National Library of Canada
Acquisitions and Bibliographic Services Branch
395 Wellington Street
Ottawa, Ontario
K1A 0N4

Bibliothèque nationale du Canada
Direction des acquisitions et des services bibliographiques
395, rue Wellington
Ottawa (Ontario)
K1A 0N4

Your file Votre référence

Our file Notre référence

NOTICE

The quality of this microform is heavily dependent upon the quality of the original thesis submitted for microfilming. Every effort has been made to ensure the highest quality of reproduction possible.

If pages are missing, contact the university which granted the degree.

Some pages may have indistinct print especially if the original pages were typed with a poor typewriter ribbon or if the university sent us an inferior photocopy.

Reproduction in full or in part of this microform is governed by the Canadian Copyright Act, R.S.C. 1970, c. C-30, and subsequent amendments.

AVIS

La qualité de cette microforme dépend grandement de la qualité de la thèse soumise au microfilmage. Nous avons tout fait pour assurer une qualité supérieure de reproduction.

S'il manque des pages, veuillez communiquer avec l'université qui a conféré le grade.

La qualité d'impression de certaines pages peut laisser à désirer, surtout si les pages originales ont été dactylographiées à l'aide d'un ruban usé ou si l'université nous a fait parvenir une photocopie de qualité inférieure.

La reproduction, même partielle, de cette microforme est soumise à la Loi canadienne sur le droit d'auteur, SRC 1970, c. C-30, et ses amendements subséquents.

Canada

Simulation studies of cubic crystal interfaces:
Instabilities and transitions

Loki Michael Jörgenson

B.Sc., Queen's University, 1986

M.Sc., McGill University, 1989

Department of Physics, McGill University

Montréal, Québec CANADA

Richard Harris, Thesis Supervisor

A Thesis submitted to the Faculty of Graduate Studies and
Research in partial fulfillment of the requirements
of the degree of Doctor of Philosophy in Physics

National Library of Canada
Acquisitions and Bibliographic Services Branch
395 Wellington Street
Ottawa, Ontario
K1A 0N4

Bibliothèque nationale du Canada
Direction des acquisitions et des services bibliographiques
395, rue Wellington
Ottawa (Ontario)
K1A 0N4

ISBN 0-315-87591-7

Shortened title (47 characters including spaces):
Simulation studies of cubic crystal interfaces

Full title (78 characters including spaces):
Simulation studies of cubic crystal interfaces:
Instabilities and Transitions

Abstract

We study the behaviour of a simple cubic crystal interface through the analysis and simulation of the Ising model in three dimensions; we use an algorithm which permits local temperature variations by emulating thermal diffusion. We derive a description of the interface based on the thermal fluctuation population at equilibrium and then use it to identify the equilibrium and dynamic roughening transitions observed under a variety of circumstances including a planar interface at equilibrium, a metastable bulk inclusion, an evaporating inclusion and a planar interface in the presence of a driving force. We also study strongly driven interfaces which exhibit an instability and pattern formation behaviour known as the Mullins-Sekerka instability. We use a special two-dimensional version of the simulation model to examine the linear growth of unstable modes of a driven interface; we compare our simulation data to theoretical predictions for the cases of an unstable flat interface and circular disk interface. Returning to the fully three-dimensional code, we present simulation data of late-time dendritic growth, including an analysis of the information available in the thermal fields. We also show that, at low temperatures, the tips of dendrites are facetted and demonstrate a response to the driving force which is consistent with the dynamic roughening transition.

Résumé

Cette thèse etudie la dynamique des interfaces d'un cristal cubique simple par l'analyse et la simulation du modèle de Ising en trois dimensions. Un algorithme simulant la diffusion thermale et permettant des variations locales de temperature a été utilisé. Une description analytique de l'interface en équilibre basée sur les fluctuations thermales y est également dérivée. Celle-ci est ensuite utilisée pour l'identification de la transition rugueuse, tant pour des cas statiques que dynamiques, tels ceux d'une surface plane en équilibre, d'une goutte metastable, d'une goutte en évaporation, et d'une surface plane poussée par un force externe. Cette thèse étudie également des interfaces montrant la formation de motifs cohérents resultant d'une instabilité, alors dites de Mullins-Sekerka. Une version modifiée et en deux dimensions de notre modèle est utilisée pour examiner la croissance linéaire des modes instables d'interfaces à une dimension. Les résultats obtenus sont comparés aux prévisions analytiques pour une surface plane et un disque. Finalement, les résultats de simulations de l'instabilité dendritique en trois dimensions sont présentés. Les résultats obtenus pour les champs thermaux et les interfaces, et ce pour le régime non-lineaire aux temps avancés, sont analysés. En outre, une partie de cette thèse étudie les facettes trouvées sur les extrémités des dendrites de même que les relations entre la croissance et la transition rugueuse cinétique.

Dedication

For Thalie, without reservation or qualification.

Acknowledgements

I would like to acknowledge the support and understanding of my thesis supervisor, Richard Harris; I will always appreciate the consistency and reliability of his guiding influence in my work and my development as a physicist. I am indebted to him for sharing my vision of how physics can be done as much as showing me how to do it well.

⊙

My explicit and unqualified thanks are given to the procedural administrators who have made my efforts less tiresome, Diane Koziol, Selina Stewart and Cindy-Ann Thomas.

⊙

Additional thanks go to Martin Grant for his support and guidance, to Hong Guo for his help and contributions and to Ross Thomson and Martin Lacasse for their enlightening insights into the manifold ways of the Machine. And to Eugenia Corvera for all the *besos y abrazos.*

⊙

I am also indebted to Tao Sun for his contribution to my understanding of the roughening transition and renormalization theory.

⊙

Thanks go to Douglas Stairs for making this at all possible.

⊙

I would also like to thank no one in particular for bringing this to an end and a new beginning.

○

Contents

List of Figures

1 Introduction

Crystals have forever captured the eye and the imagination. Common quartz, iron pyrite and amythest evoke as much wonder and curiousity as precious gemstones, simply for their unearthly symmetry and geometric beauty. The intricate growth forms of snowflakes and hoarfrost are eternal sources of inspiration for poets, philosophers and scientists alike. But like so many of Nature's mysteries, the secrets of crystals and crystal interfaces have been only reluctantly revealed through painstaking study.

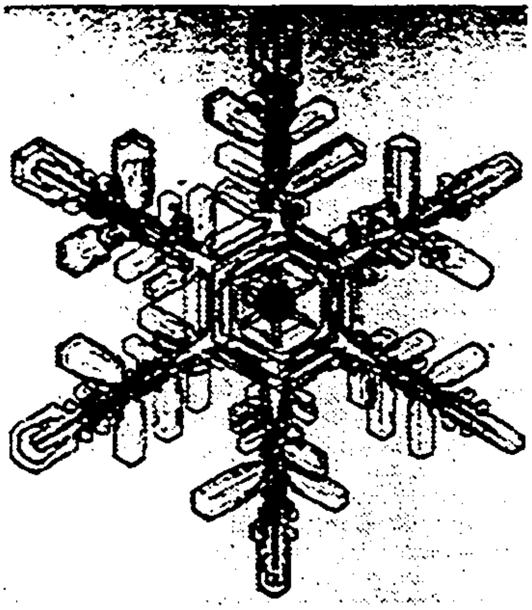

Figure 1: A classic snowflake grown by Furukawa. Reproduced from (Yokoyama and Kuroda 1990).

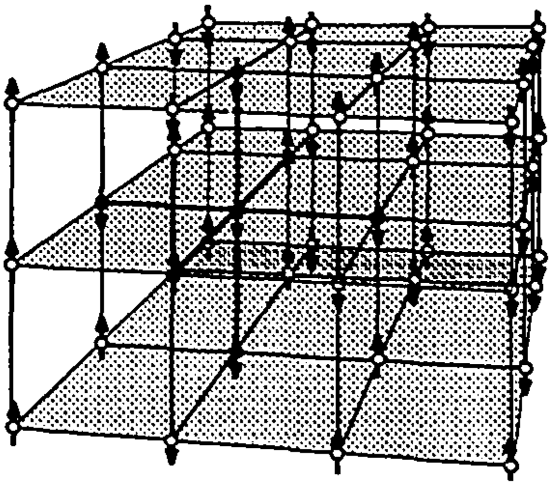

Figure 2: Toy 3D Ising model

In this thesis, we endeavour to contribute to the growing store of knowledge by studying the behaviour of a crystal interface using computer simulation. Our means will be the simulation and analysis of the simple cubic Ising model. This is a simple model of spins with values of ±1 (ie. a *solid-liquid* or *solid-vapour* two-phase system) regularly spaced on a three-dimensional lattice as pictured in Figure 2; since its spatial structure is precisely that of a crystal, a boundary separating bulk concentrations of each phase provides an excellent repre-

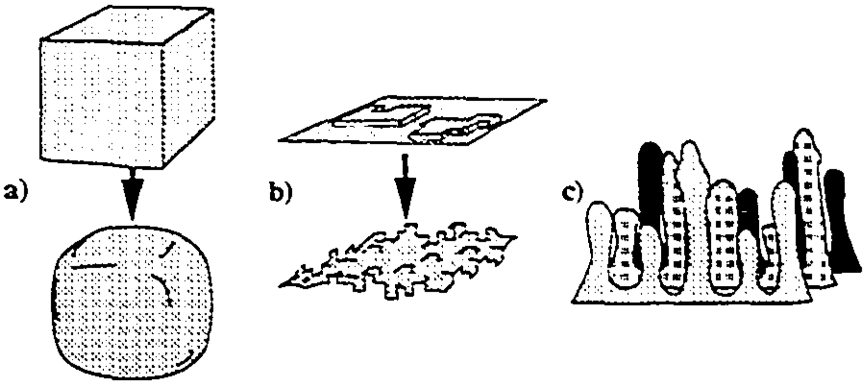

Figure 3: Cartoons of a) the equilibrium (or dynamic) roughening transition on a bulk inclusion, b) the equilibrium (or dynamic) roughening transition on a planar interface, and c) the Mullins-Sekerka instability on a planar interface.

sentation of a crystal interface. The interface, which is a two-dimensional object in a three-dimensional system, can be planar and oriented in any specific direction relative to the lattice's axes, or encompass a *bulk inclusion* or *droplet* of one phase within a background of the other and thus present surfaces of every possible orientation.

Our goal will be to examine several distinct yet related aspects of such an interface, at, near and far from equilibrium, and thus to illustrate elementary aspects typical of real crystal interfaces. In Figure 3, some of these aspects are depicted: **At equilibrium**, a crystal surface demonstrates a structural phase transition, called the *equilibrium roughening transition*, which affects both the equilibrium shape of a droplet interface and the behaviour of thermal fluctuations on a planar interface. Below a critical temperature, the plane will be flat and relatively featureless, while the droplet is faceted, each reflecting the underlying lattice structure. At the critical point and all temperatures above, the plane becomes rough and its width diverges over long lengthscales; the droplet also shows roughening and its facets disappear. **Near equilibrium**, when subjected to a small driving force, the interface moves (or is static and exhibits enhanced curvature), modifying the equilibrium behaviour. As well as transforming at a critical temperature, the surface may transit at a critical applied force for a given temperature; this is the *dynamic* or *kinetic roughening tran-*

sition. Far from equilibrium, the interface becomes unstable and begins to grow, generating complex tree-like structures called *dendrites.* The growth is not arbitrary but selects specific directions, lengthscales and rates of movement which depend on the nature of the crystal lattice as well as the physical considerations (eg. the strength of the driving force). This is known as the *Mullins-Sekerka instability.* Each of these phenomena represent a basic problem in the physics of interfaces and each has resisted a complete analytic description of the essentially simple processes governing their dynamics. By studying the interface in a simple cubic Ising model under such a variety of conditions, we hope to build a complete description of crystal interface behaviour, from equilibrium to dynamics.

As mentioned above, the equilibrium roughening transition is marked by two distinct modes of behaviour: A planar interface of a specific orientation (eg. {100} in the simple cubic crystal) passes from a flat, highly correlated state to a roughened wandering one. A droplet interface, which necessarily presents surfaces of all possible orientations, passes from a faceted, geometric form (eg. like a cube) to a rough, rounded one. While it will be shown in later Chapters that these two behaviours are related, historically the former has acted as the basis for theoretical analysis and the latter for experimental studies. The reason for this is tractability in each of the two contexts; a flat interface has fewer complications to account for and lends itself to being modeled more easily than a curved surface, hence it is simplest for theorists to grapple with; equilibrium crystal surfaces are difficult to control and so experimentalists have had the greatest success with small, approximately spherical droplets.

Most natural crystals are formed away from equilibrium; they then only change very slowly through surface diffusion and adsorption/desorption, strongly limited by the low rate of mass transport of material. True equilibrium shapes are independent of any dynamical or thermal history, defined only by the nature of the crystal lattice and the current thermodynamic conditions, such as temperature and pressure. Producing and maintaining true equilibrium has always been a challenge for experimentalists. For this reason, the equilibrium roughening transition was theoretically predicted long before it was actually observed. In a now landmark paper, Burton, Cabrera and Frank (1951) suggested that there was a critical temperature at which the planar interface of a simple cubic Ising model would be transformed from a flat, correlated surface to a roughened one. They believed that at sufficiently low temperatures there was a barrier imposed by capillary forces which would inhibit the roughening normally associated with thermal fluctuations. At the critical temperature, they believed that the fluctuations would be just strong enough to delocalize the interface. However, their analysis was based upon a simplified model with fluctuations restricted to a single layer and thus their results were viewed with some doubt. Chui and Weeks (1976) eventually showed that their analysis was indeed correct. They also showed that the transition was of a Kosterlitz-Thouless type (Kosterlitz and Thouless 1973) (ie. of infinite order) and consequently very difficult to observe.

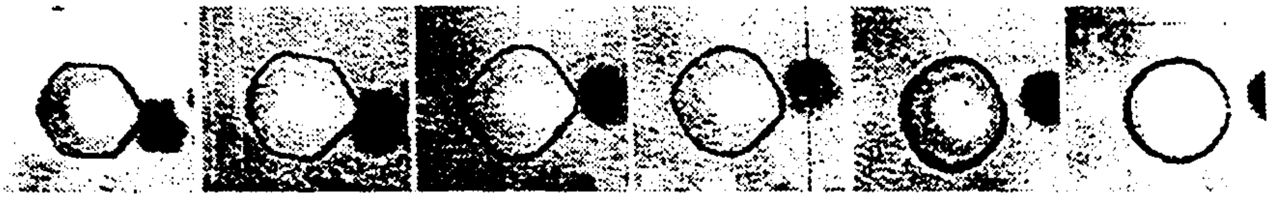

Figure 4: A small droplet ($\sim 50\mu m$) of tetrabrommethane as it passes from $T = 50$ C to $T = 92$ C through its roughening temperature. Reproduced from reference (Pavlovska and Nenow 1977).

At about this time, refinements in experimental techniques were finally making it possible for experimentalists to observe true equilibrium crystal shapes. What they saw was consistent with the idea of the roughening transition: The crystal surfaces underwent a structural transition with temperature which changed their profile from multi-faceted, geometric shapes at low temperature to rounded, roughened lumps at high temperature. Early efforts by Pavlovska and Nenow (1977) with *negative crystals* (vapour bubbles within a crystal lattice) in such substances as diphenyl, napthalene and tetrabrommethane revealed a reproducible transition from a faceted to unfaceted state within certain temperature ranges. Similar observations were made by Jackson and Miller (1977) using hexachlorethane. Since then, Heyraud and Métois (1980; 1987; 1987; 1989) have produced many excellent results using simple metals and ionic compounds like gold, indium, sodium chloride and lead. However, the most impressive data has come from experiments with helium crystals, either ^{4}He (Wolf, Balibar and Gallet 1983; Wolf et al. 1985; Gallet, Balibar and Rolley 1987) or ^{3}He (Rolley, Balibar and Gallet 1986; Rolley et al. 1983); their work has been so well controlled that they have been able to provide solid quantitative evidence on both crystal droplet profiles and planar crystal interfaces. Moreover, the behaviour of ^{4}He is particularly interesting in that it demonstrates three distinct roughening transitions on three different faces due to its hexagonal close-packed structure (see Figure 5).

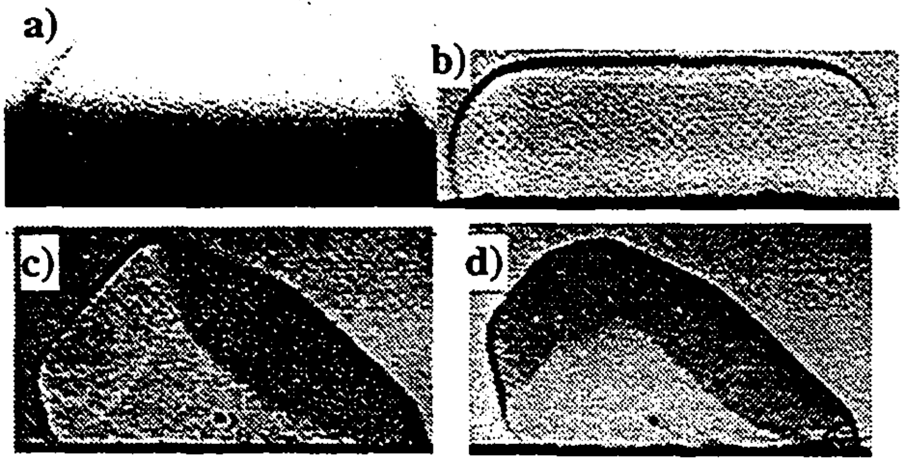

Figure 5: Equilibrium ^{4}He crystals at various temperatures between the three roughening transitions: a) at $T > T_{R3} > T_{R2} > T_{R1}$, b) at $T_{R3} > T > T_{R2}$, c) at $T_{R2} > T > T_{R1}$, and d) at $T_{R1} > T$. Reproduced from reference (Balibar, Gallet and Rolley 1990).

Adding to the experimental evidence, simulation work has begun to play an increasingly important role in identifying and quantifying the roughening transition. In particular, the planar crystal interface has been studied using the solid-on-solid (SOS) model (Weeks and Gilmer 1979; Weeks 1980), a natural consequence of its use in theoretical work by Chui and Weeks. This model employs a two-dimensional regular grid of columns, each with a height h_i and an interaction energy defined by the difference (h_i-h_j) between neighbouring sites; Figure 6 shows a toy version of it. At low temperatures where surface fluctuations tend to be small and few, this model favourably emulates a planar interface and successfully avoids the burden of a fully three-dimensional simulation sytem. Thus, it is perfectly suited for the study of the equilibrium transition. Some groups have made attempts at simulating the Ising model in three dimensions (Bürkner and Stauffer 1983; Mon et al. 1988; Mon, Landau and Stauffer 1990); however, results have been somewhat limited due to the restrictions of available computer hardware. Although less simulation work has been done on droplets, analysis of the Ising model has provided detailed descriptions of the equilibrium shapes of various crystal lattices, above and below the roughening transition, in two (Rottman and Wortis 1981; Holzer 1990a) and in three dimensions (Rottman and Wortis 1984a; Touzani and Wortis 1987; Holzer and Wortis 1989; Murphy and Rottman 1990). In the two-dimensional case, these analyses has been confirmed by Ising model simulations (Saito and Ueta 1989). Reviews of research on the equilibrium roughening transition can be found in Weeks (1980), Rottman and Wortis (1984b), and van Beijeren and Nolden (1987).

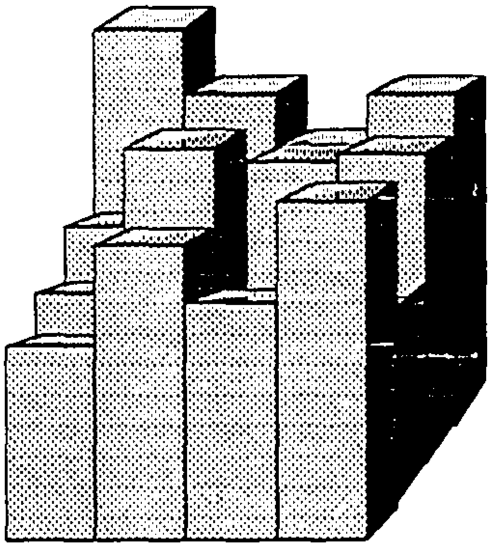

Figure 6: Toy SOS model

In Nature, it is much more common to find crystal interfaces which were formed while weakly driven away from equilibrium. As pointed out above, experimentally it is far more difficult to establish true equilibrium than to maintain a non-equilibrium context. Moreover, industrial crystal growth techniques depend directly on the particulars of weak interface growth. Consequently, there is considerable interest in understanding how small forces affect the behaviour of an interface. Chui and Weeks (1978) first proposed the existence of a dynamic roughening transition two years after their initial equilibrium analysis. This was followed by a more rigorous analysis by Nozières and Gallet (1987) which has provided a clear understanding of the problem: If the interface is only weakly coupled to the underlying lattice (ie. below but near the equilibrium transition temperature), a sufficiently strong driving force will tend to decouple it completely, thermal fluctuations then causing it to roughen; stronger driving forces can cause the interface to decouple and appear rough at even lower temperatures. The driven interface thus *appears* to have a roughening transition temperature below the equilibrium value; the dynamic transition is typically characterized by this apparent depression of the roughening temperature. The transition also exhibits a marked broadening of the critical region wherein, for a given driving force, the surface passes from a one structural phase to the other in a finite range of temperature. Both of these effects have been observed in a variety of experiments (Jackson and Miller 1977; Pavlovska and Nenow 1977), including on the leading tips of growing dendrites (Maurer, Bouissou and Perrin 1989) (see Figure 61). However, the most precise measurements have once again been made with ^{4}He (Wolf et al. 1985; Balibar, Gallet and Rolley 1990; Gallet, Balibar and Rolley 1987); this is attributed to the relatively high rates of surface mass transport of material on solid helium which reduce the typically long dynamical timescales to an observable level.

Significant contributions are beginning to be made through numerical analysis and simulation; most notably, work has been done using the Kardar-Parisi-Zhang equation (Kardar, Parisi and Zhang 1986; Medina et al. 1989; Grossman, Guo and Grant 1991), a nonlinear differential equation modeling interface growth in the presence of a influx of particles, and with the solid-on-solid model (Kim and Kosterlitz 1989; Grossman, Guo and Grant 1991). However, due to the importance of the dynamics required to simulate this phenomenon in three dimensions, there are still relatively few results. Refinements to the analysis of a driven interface are already appearing (van Saarloos and Gilmer 1986; Ben Amar and Pomeau 1988; Hwa, Kardar and Paczuski 1991), partially in response to these studies. However, this problem is far from being completely understood as these results are often inconsistent with experiment or one another.

When a crystal interface is strongly driven, it decouples completely from the lattice and grows freely. In general, this leads to an instability in the interface and eventually to a pattern-selection mechanism. The rich history of unstable interfaces encompasses many different phenomena (see Kessler *et al.* (1988) for a review) which are, for the most part, intrinsically non-linear, dynamical problems involving thermodynamically irreversible, dissipative processes that resist a coherent analytic description. The Mullins-Sekerka instability is characteristic of these phenomena and has proved a difficult problem to characterize completely. It is seen routinely in many different contexts such as the solid-vapour growth of snowflakes and the solid-liquid growth of alloy solidification processes. However, it has only been closely studied in the last decade or so; a summary of prior experimental work can be found in either Glicksman (1984) or Laxmanan (1985). Water ice has been used to grow snowflake-like crystals (Sekerka 1971; Langer, Sekerka and Fujioka 1978; Yokoyama and Kuroda 1990); rather impressive work has been done with succinonitrile (Glicksman 1984; Chou and Cummins 1988) and to a certain extent with NH_4Br (Dougherty

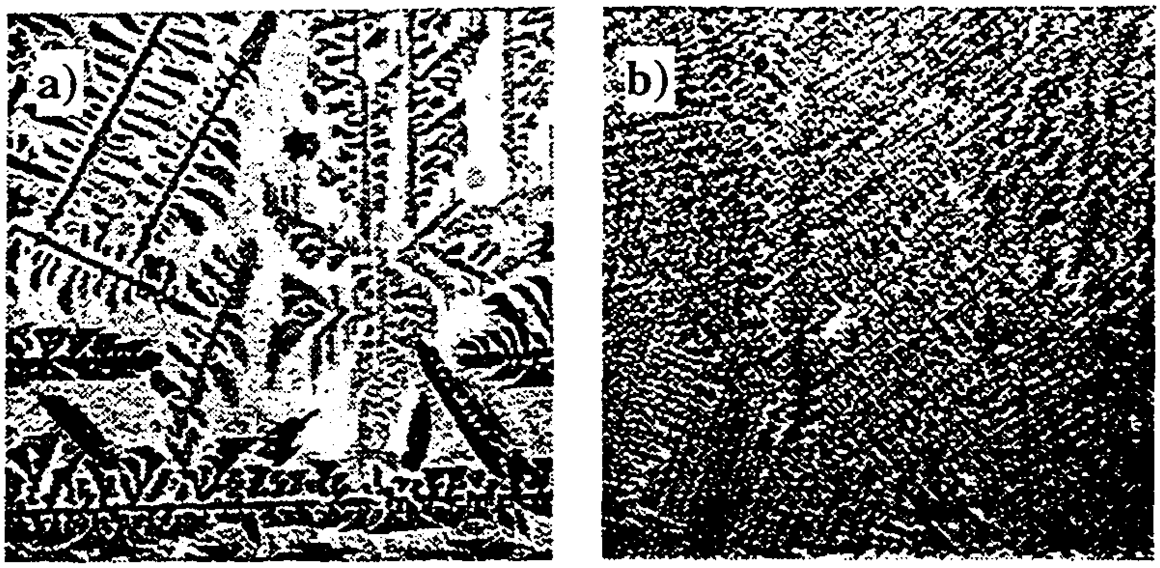

Figure 7: Dendritic growth patterns observed in a) a thin film of an initially uniform salt mixture, CuCl and $PbCl_2$, and b) Cu-Zn alloy (brass). From work by J. van Suchtelin, Philips Research, Einthoven, Netherlands and J.P.A. Löfvander, Univ. of California, Santa Barbara respectively. Reproduced from reference (Langer 1992).

and Gollub 1988; Maurer, Bouissou and Perrin 1989). Also, spontaneously occurring dendrites are often studied in the context of industrial processes involving crystal and alloy manufacture, underlining their importance to commercial concerns.

The Mullins-Sekerka instability was initially described (Mullins and Sekerka 1963) in terms of a linearized diffusion equation which, while able to capture the essential physics at the early stages of the instability, was not able to predict the selected instability modes; the analysis suggests that there should be a mixture of lengthscales represented, however it is observed experimentally that only one dominates at late times. The maximum velocity mechanism first proposed by Mullins and Sekerka to predict this lengthscale was eventually discounted by the experimental work of Glicksmann (1976). Langer and Müller-Krumbhaar (1978) then hypothesized a context wherein a growing dendrite selects a speed and shape for which it is marginally stable. This argument still stands although it has never been given a solid theoretical underpinning. During the mid-80's, an approach known as microscopic solvability theory was developed which successfully incorporated the anisotropy of the crystal lattice and properly predicted, for a dendrite of axially-circular symmetry, the shape and velocity of the tip (Kessler, Koplik and Levine 1986). However, even now, some doubt is being cast upon it as a complete and accurate description of the fully three-dimensional dendrite problem (Langer 1992); as Langer suggests, a complete and physically relevant description may require a multidisciplinary effort encompassing fluid dynamics, metallurgy, non-equilibrium thermodynamics, nonlinear dynamics and possibly chaos theory. Reviews on unstable interfaces in general and the Mullins-Sekerka instability in particular can be found in Langer (1980; 1987) and Kessler *et al.* (1988).

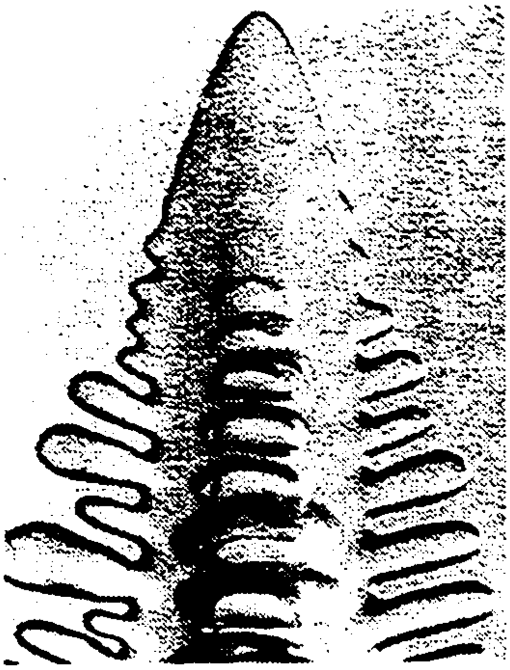

Figure 8: A succinonitrile dendrite grown by Glicksmann. Reproduced from (Langer 1992).

Simulation work on the problem has been largely limited to two-dimensions, including snowflake pattern formation models (Yokoyama and Kuroda 1990), Ising models (Guo and Jasnow 1986; Harris, Jörgenson and Grant 1992) and numerical simulation of various interface growth models such as local interface approaches (short-range, localized interaction) like the geometrical model (Browser et al. 1984) and the boundary layer model (Ben-Jacob et al. 1984), the one-sided diffusion model (Saito, Goldbeck-Wood and Müller-Krumbhaar 1988) and the cell-dynamical scheme (Liu and Goldenfeld 1990). Although each has improved upon the understanding of the instability, very few attempts have been made to expand them to the fully three-dimensional problem. Indeed, none of the aforementioned interface problems, equilibrium or dynamic, have really been studied effectively in three dimensions using simulation. The reason for this is simply that computer hardware has only very recently been capable of the task.

Most computer models are discretized in some fashion (eg. the Ising model), the smallest unit defining the lower limit of the system resolution. In order to usefully model a physical context, it is traditionally estimated that the lengthscales of interest should be at least one order of magnitude larger than the unit length and at least one order less than the system size, preferably in each of the three dimensions. This sets a minimum recommended limit for system size (in the Ising model) of $\sim 100^3$ or one million sites, assuming that there is only one important lengthscale and that it can coerced to be ~ 10 units in length. From small workstations to CRAYs, this represents a significant investment in computer memory and, depending on the complexity of the algorithm, may also represent a considerable amount of cpu power. Until now, only the largest and fastest machines were capable of running such a simulation. Traditional computer research has employed models based on some simplification, such as the solid-on-solid model, which makes three dimensions manageable. However, they also introduce compromises in behaviour which limit their usefulness and physical relevance; for example, the SOS model cannot reproduce sidebranching or simulate a droplet interface, two important aspects of the fully three-dimensional dendritic growth problem.

Still, the importance of simulation research cannot be ignored, especially as technology grows to meet the challenge of ever more physically complete models. As mentioned before, theoretical progress is often hampered by the abstruse nature of interface problems while experimental studies are limited by the available materials and the precision with which they can be manipulated. Simulation acts as the ideal bridge between the two, providing an absolutely controllable environment for the testing of theory and for reproducing simplified physical phenomena. Our work presented here underlines this fact as we confirm numerous theoretical predictions and reproduce many physical observations by performing several original simulation studies at the limit of our available computer hardware.

In this thesis we report original contributions to each of the aforementioned subjects. In like style, we examine each context of the simple cubic crystal interface in terms of simulation results using the simple cubic Ising model; the equilibrium roughening transition on the planar interface, the dynamic roughening transition on both a driven planar and metastable bulk inclusion interface, and the Mullins-Sekerka instability in the presence of a thermal gradient on a planar interface. In each case, we present results of simulations in three dimensions which, to the best of our knowledge, have never been done before. Further, we provide original analyses of several equilibrium and growth behaviours as well as confirmation and comparison of many theoretical and experimental results.

In Chapter 2, we overview the equilibrium roughening transition. First, we present a renormalization derivation of the equilibrium roughening transition on a planar interface, based on a generalized solid-on-solid model. Included are the foundations for the behaviour of the interface in a weak field. We also summarize many of the basic characteristics of the equilibrium transition. Next, we demonstrate how the equilibrium shape of a droplet interface is defined by the anisotropic surface energy and subsequently, how it changes with the roughening transition. To do this, we introduce the Wulff construction which exactly defines the crystal shape given a radial description of the surface energy, offering a basic derivation based on the approach of Landau and Lifshitz (1980).

In Chapter 3, we introduce the basic theory describing the Mullins-Sekerka instability. Following the linear stability analysis attributed to Mullins and Sekerka, we examine the initial stages of the instability on a planar interface in the presence of a thermal gradient. The result clearly identifies the unstable modes of the interface under a driving force. This analysis is then extended to a spherical interface; in this case, we find a critical radius of stability which limits the onset of the unstable modes. Finally, we examine the unpertubed steady-state solutions for a needle-like crystal. These results then provide a basis for testing and analyzing the data presented in later Chapters.

In Chapter 4, the simulation model is described. We first review the basic simple cubic Ising model through meanfield analysis, demonstrating how a first-order phase transition is introduced through a uniform external field and a degeneracy in the upper energy spin state. We also describe the Monte Carlo method used, the Creutz (1984) multi-demon algorithm, and show how it provides for local temperature variations; in addition, we introduce a novel thermal diffusion mechanism with a simple, consistent and controllable behaviour. We explain how the model was employed to simulate various interface configurations and geometries.

In Chapter 5, we present the results from a variety of simulations at and near equilibrium. In four Sections, we examine each of four different contexts significant to the roughening transitions, both equilibrium and dynamic: We first establish a unique basis for characterizing interfaces which we then use throughout this Chapter; we analyse the fluctuation distribution on a planar interface at equilibrium, demonstrating divergent aspects of its behaviour at the transition, and derive specific quantities which can be measured on real and virtual interfaces. We then compare this description with simulation data; we show that the equilibrium roughening transition is more clearly identified using this approach than conventional measurements. Next, we examine a metastable bulk inclusion, noting that a stabilizing force is required to prevent the system from minimizing the interface energy and evaporating the droplet. We then compare the theoretical predictions for how the roughening transition of a static interface is modified by an external field to our simulation results. As a comparative exercise, we also study the behaviour of the inclusion when the stabilizing field is removed; the droplet *appears* to pass quickly through a roughening transition, even though the temperature is not changing and there is no external force. We supply a mechanism based on well-known growth/evaporation processes to explain this phenomenon. Finally, we make a qualitative study of the planar interface weakly driven by a thermal gradient for contrast with the equilibrium and inclusion behaviours. We make contact with several aspects of current dynamic roughening transition theory, highlighting the behaviour of the fluctuation distribution quantities defined in the first Section.

In Chapter 6, we test the linear stability analysis presented in Chapter 3. Due to the complex nature of dendritic growth at late times, this early-time behaviour represents our best opportunity to directly test available instability theory. To our knowledge, this has never been done before in either experiment or simulation due to the brief timescale of the linear behaviour. We present two distinct contexts wherein we are able to compare specific predictions with our simulation data. In order to enhance the resolution in our measurements, we employ a two-dimensional version of our code. There are no significant differences between unstable one-dimensional and two-dimensional interfaces at the level of the linear stability presented in Chapter 3; we re-derive any important analytic expressions. First, we study the growth modes of an unstable planar interface, looking for the predicted dispersion relation which describes the relative strengths of the unstable modes. We use the established technique of long-range spin interactions (Heermann 1984; Grant et al. 1985) to extend the linear growth regime. Taking advantage of the reduced cpu requirements of a one-dimensional interface, we use the longest interface possible for maximum resolution. Second, we study the behaviour of an unstable circular inclusion; it has an anticipated radius of stability at which the disk first begins to go unstable. We estimate this lengthscale using two separate measurements and compare it with our simulation results.

In Chapter 7, we present simulation trials of late-time, non-linear dendritic growth in three dimensions; these results are considered ground-breaking attempts at reproducing the physically complete Mullins-Sekerka instability. We study two interface geometries, the fully three-dimensional *block* system and the pseudo-two-dimensional *slab* system, each clearly demonstrating dendritic growth at specific lengthscales. We characterize the interfaces in terms of their power spectra, interface areas and dendrite tip speeds and relate this to instability theory. We comment on various inconsistencies between the simulations and experimental results and identify possible shortcomings in the simulation model. Using the thermal field defined by our model, we perform a test of our algorithm to reliably model diffusion processes and then examine the thermal diffusion mechanism governing the instability through imaging techniques. We demonstrate a variety of instability behaviours with their corresponding thermal fields and then make a detailed analysis of the influence of the system parameters on the growths. It is shown how thermal fluctuations and diffusion rates control the shapes of the dendrites and their rates of growth. Finally, we examine the influence of the dynamic roughening transition on growing dendrites; we show how the tips are faceted at low temperatures and demonstrate that, similar to experiment, we observe a transition in the tip growth response to changing driving force.

2 Two-Phase Interfaces in Equilibrium

At equilibrium, a crystal interface is defined by the nature of its underlying lattice and by the strength of the ambient thermal fluctuations. For the moment, let's consider a planar solid-vapour interface with the lowest possible Miller index ($\{100\}$ for a simple cubic crystal; see Appendix A.1). At low temperatures, the interface is highly correlated (ie. flat). Thermal fluctuations are manifested in the form of a small number of islands or *micro-facets* raised one lattice unit above the reference plane (for example, see Figure 18). These micro-facets are not stable but appear spontaneously and then shrink until they disappear. Macroscopically, the interface is fixed relative to the lattice and does not move or change. At higher temperatures, the thermal fluctuations are larger and more numerous; they may even appear atop other fluctuations. However, the interface remains fixed and flat on long length scales. At some critical temperature T_R, fluctuations will be so numerous as to overwhelm the reference plane and it will be lost; the interface will appear *rough*. It will no longer be constrained and thus it will wander freely; macroscopically, the interface width will diverge over long length scales. At all temperatures above T_R, the interface will be rough, the amplitude of the roughening increasing with T. This phenomenon is referred to as the *roughening* transition or, less frequently, the *facetting* transition. In Section 2.1, we shall reproduce a renormalization analysis of the transition and summarize the thermodynamic characteristics of an infinite planar $\{100\}$ interface near T_R.

The planar interface described above has a fixed orientation relative to the crystal lattice. However, when an interface defines an enclosed volume, all possible surface orientations may be present. We might for example consider the context of a simple bulk inclusion of one phase in a bath of another phase - prehaps a solid droplet or small crystal in a liquid melt - but in the limit of infinite droplet volume to avoid finite-size effects. Since in the simple cubic crystal only $\{100\}$ interfaces have a finite T_R (all other orientations have $T_R = 0$), a mixture of facetted and roughened surfaces is observed on a droplet surface near $T_R^{\{100\}}$; at the transition point, the entire interface is then roughened. Thus the equilibrium shape of a crystal droplet is another manifestation of the underlying lattice structure and also exhibits a transition behaviour. In Section 2.2, we review the Wulff construction and show how it exactly defines the equilibrium shape of a bulk inclusion above and below T_R.

Within both sections, we review the physics of the roughening transition and establish a foundation for the analysis of our simulation results presented in Chapter 5.

2.1 The Roughening Transition

In 1951, Burton, Cabrera and Frank (1951) proposed that an equilibrium crystal interface may exhibit a structural phase transition, from a smooth, flat phase at low temperatures to a rough, curved one at high temperatures. They carried out an analysis of the $\{100\}$ surface of a simple cubic crystal, restricting thermal fluctuations to the first layer. They showed that the interface would remain flat only up to a critical temperature T_{BCF} which they referred to as the roughening temperature. However, their single-layer assumption is of limited use near the transition when fluctuations extend well beyond the first layer and, so, their insight into the transition could not be validated. It was eventually shown by van Beijeren (1975) that T_{BCF} is actually a lower limit for the roughening transition. In 1976, Chui and Weeks (1976) provided the key, demonstrating the relationship between the discrete Gaussian (dG) interface model (a solid-on-solid (SOS) model with quadratic interactions) and a 2D Coulomb lattice-gas through a duality transformation, the latter model already having been shown to have a Kosterlitz-Thouless transition (Kosterlitz and Thouless 1973).

Subsequently, the presence and nature of the *roughening* transition have been firmly established, both experimentally and theoretically.

This phenomenon is restricted to planes with {100} orientation. This is a consequence of the symmetry of the simple cubic crystal structure which causes the {100} interface to be strongly coupled to the lattice. Other orientations like the {111} plane are much more weakly coupled due to the reduced spatial coherence of the sites relative to the interface; at all $T > 0$, it is decoupled from the lattice by thermal roughening. Crystal structures like hexagonal close-packed and face- and body-centered cubic do exhibit facets with different orientations; consequently, they also have multiple transition temperatures, one for each orientation. However, they are also less accessible than the simple cubic structure to analytic techniques like the SOS model.

Before a more detailed analysis of the roughening model, we shall review some of the elementary aspects of transition theory. The behaviour of the height-height correlation function $G(r)$ introduced by Chui and Weeks (1976) for the SOS model reflects the basic nature of the transition. The Solid-On-Solid model is a regular 2D lattice of sites $\{i, j\}$ each with a height h_{ij}; it is a simplification of the planar 2D interface in that it prohibits overhangs and bubbles in the bulk. This is particularly appropriate for low temperature simulations where the interface width is small. The interaction energy is typically defined by a Hamiltonian like $\mathcal{H} \propto \sum_{ij}(|h_{i,j} - h_{i+1,j}| + |h_{i,j} - h_{i,j+1}|)$. The height-height correlation function is defined as

$$G(r) \equiv \langle (h_{ij} - h_{kl})^2 \rangle = \sum_{h_{ij}} \sum_{h_{kl}} (h_{ij} - h_{kl})^2 \, P(h_{ij}, h_{kl}) \tag{1}$$

where $r \equiv \| h_{ij} - h_{kl} \|$ and $P(h_{ij}, h_{kl})$ is the probability of height h_{ij} at (i, j) and height h_{kl} at (k, l). It has been shown (Chui and Weeks 1976; Ohta and Kawasaki

1978) to have an analytic form

$$G(r) \propto F(T)a^2 \log\left(\frac{1}{a^2(\xi^{-2} + r^{-2})}\right) \tag{2}$$

where ξ is the correlation length between fluctuations, a is the unit lattice constant in a simple cubic crystal (ie. a is the same unit horizontally between adjacent columns and vertically in height) and $F(T)$ is an increasing function of temperature. Study of the related XY model by Chui and Weeks (1976) has shown that ξ of the SOS model is the dual conjugate of the XY vortex-vortex correlation length; its form near T_R then follows from the analysis by Kosterlitz (1974);

$$\xi = \begin{cases} \xi_0 e^{B/\sqrt{T_R - T}} & T \to T_R^- \\ & \\ \infty & T \geq T_R \end{cases} \tag{3}$$

where B is a non-universal constant. Thus, at $T > T_R$, $G(r)$ diverges at large r like $\log(r/a)$. Below T_R, $G(r)$ saturates at $r > \xi$ like $F(T)a^2 \log(\xi/a)$. The prefactor $F(T)$ has a universal value at T_R of $2/\pi$ (Ohta and Kawasaki 1978); it approaches this value from above like

$$F(T) = \frac{2}{\pi} + C_{onst}\sqrt{T - T_R} \qquad T \to T_R^+ \tag{4}$$

where the constant is non-universal.

Also central to the roughening transition is the free energy per unit length, $E_s(T)$, required to form a step. As its name suggests, a *step* is a vertical dislocation of the interface by one lattice unit. It is the dual conjugate of the spin-spin correlation length in the XY model (Swendsen 1978). Below T_R, the step free energy is finite and provides a barrier to the formation of steps. At T_R, E_s goes to zero permitting steps to proliferate without bound and thus resulting in the roughening of the interface. From Kosterlitz' results, near T_R the step free energy behaves like

$$E_s = \begin{cases} E_0 e^{-B/\sqrt{T_R - T}} & T \to T_R^- \\ \\ 0 & T \geq T_R \end{cases} \tag{5}$$

where B is the same non-universal constant in (3).

These results have been subsequently shown to be true for all SOS models (José et al. 1977), regardless of lattice structure or details of the interaction. Further, van Beijeren (1977) showed that the SOS model for the body-centered cubic crystal could be mapped into the exactly solvable six-vertex model, subsequently recovering all the same results. Thus the basic characteristics of the roughening transition are applicable to any interface model with a regular lattice.

2.1.1 Renormalization Analysis of a Roughening Model

In order to establish the physical basis for the roughening transition, we shall walk through a more detailed renormalization analysis of a generalized SOS model based upon the derivation of Weeks *et al.* (Chui and Weeks 1976; Weeks and Gilmer 1979). We present a summary of important analytic expressions in Section 2.1.2.

We shall choose a Hamiltonian which is as general as possible, using a quadratic height-height interaction for reasons of analytic simplicity (the transition behaviour is independent of the specifics of the interaction); in this form, it is referred to as the discrete Gaussian model (dG). As usual, it is written in terms of a regular lattice with heights h_{ij} with the interaction extending over some range $\delta = \| \{i,j\} - \{k,l\} \|$ which can be greater than unity;

$$\mathcal{H} = \frac{J}{2} \sum_{\{i,j\},\delta} (h_{ij} - h_{kl})^2 + JH^2 \sum_{\{i,j\}} h_{ij}^2 - \sum_{\{i,j\}} \Delta\mu_{ij} h_{ij} - 2v_o J \sum_{\{i,j\}} \cos(2\pi h_{ij}) \tag{6}$$

where J is the interaction constant and is distinct from that of the Ising model Hamiltonian used in later Sections. The first term is the site-site interaction energy over a range δ; the second term is a weak *centering* field which holds the interface at $\bar{h} = 0$; the third term is an applied field (in general, it can be different for each site) which will act as a chemical potential; the fourth term is a weighting function which plays the part of the crystal lattice in the $\hat{z}$ direction, favouring integer values of h. Although most SOS models use a discretized height variable which restricts h to integer values, this form is more general, illustrating the universality of the roughening transition; it has been shown that any periodic weighting function will result in the same equilibrium behaviour at the transition (Chui and Weeks 1976).

The dynamics of the interface is controlled through the Langevin equation

$$\begin{aligned} \frac{\partial h_i}{\partial t} &= -\frac{\Gamma}{k_B T}\frac{\partial \mathcal{H}}{\partial h_i} + \eta_i \\ &= -\frac{\Gamma}{K}\left(\sum_{\delta}(h_i - h_{i+\delta}) + H^2 h_i - \frac{\Delta\mu_i}{2J} - 2\pi v_o \sin 2\pi h_i\right) + \eta_i \end{aligned} \tag{7}$$

where $K^{-1} \equiv 2J/k_B T$. Γ will be identified later as the equilibrium evaporation rate and η_i are stochastic fluctuations which satisfy

$$\begin{aligned} \langle \eta_i(t) \rangle &= 0 \\ \langle \eta_i(t)\eta_{i'}(t') \rangle &= 2\Gamma\delta(t-t')\delta_{ii'}. \end{aligned} \tag{8}$$

Here, any quantity enclosed by $\langle\rangle$ indicates an ensemble average.

For the limiting case of no driving force ($\Delta\mu = 0$) and no discrete lattice ($v_o = 0$), (7) is exactly solvable using Fourier transform techniques; in terms of the Green's function $G(k,\omega)$, it has a form in the long wavelength limit like

$$G(k,\omega) = \left(\frac{k^2 + H^2}{K} - \imath\frac{\omega}{\Gamma}\right)^{-1}. \tag{9}$$

For an infinitesimal *centering* field $H^2 \rightarrow 0^+$, (7) is a discretized diffusion equation and thus, $G(k,\omega)$ is identically the Green's function for 2D diffusion. Re-introducing v_o as a perturbation for an infinitesimal $\triangle\mu$, we can re-write (7) in integral form

$$h(r,t) = \int_{-\infty}^{\infty} dr' \int_{-\infty}^{\infty} dtG(r-r',t-t') \left(\frac{\triangle\mu(r',t')}{k_B T} + \frac{\eta(r',t')}{\Gamma} - 2\pi K^{-1} v_o \sin 2\pi h(r',t') \right) \tag{10}$$

where r is a dimensionless 2D vector in units of lattice spacing with its point of origin at the center of a lattice site. The equilibrium behaviour of the interface can then be extracted from the limit $\triangle\mu \to 0$.

First, expanding (10) in powers of $\triangle\mu/k_B T$,

$$h(r,t) = h_0(r,t) + \int_{-\infty}^{\infty} dr' \int_{-\infty}^{\infty} dt'\; h_1(r',t') \frac{\triangle\mu(r',t')}{k_B T} + \mathcal{O}(\left(\frac{\triangle\mu(r',t')}{k_B T}\right)^2) \tag{11}$$

we suppose that the linear response function is the ensemble average over the noise $\chi(k,\omega) = \langle h_1(k,\omega)\rangle$. Thus the unperturbed linear response function is

$$\chi_0(k,\omega) = G(k,\omega) = \frac{1}{(k^2 + H^2)/K - \imath(\omega/\Gamma)}. \tag{12}$$

Subsequently, the perturbed function χ is expressed as

$$\chi^{-1}(k,\omega) = \chi_0^{-1}(k,\omega) + \Sigma(k,\omega); \tag{13}$$

Σ is a *self-energy*. By substituting (11) into (10), an exact solution for Σ is possible

$$\Sigma(k,\omega) = \frac{4\pi^2 v_o K^{-1} \mathcal{F}\{\langle \cos(2\pi h_0(rt) h_1(rt,r't'))\rangle\}}{\langle h_1(k,\omega)\rangle}; \tag{14}$$

where $\mathcal{F}\{\}$ indicates a Fourier transform in real space and time

$$\mathcal{F}\{f(\mathbf{x},t)\} = \int dt \int d\mathbf{x}\; e^{-(\imath \mathbf{k}\cdot\mathbf{x}+\omega t)} f(\mathbf{x},t).$$

The limits of behaviour of Σ as a function of temperature foreshadow the final roughening transition results. At low T, the equilibrium variations in h_0 are very small and the interface is strongly localized around $h_0 = 0$ by the weighting term. For small h_{ij}, the sine term in (7) can be expanded to first order and consequently the self-energy is shown to have a constant value even in the long wavelength and zero frequency limit;

$$\lim_{\omega,k\to\infty} \Sigma(k,\omega) \cong \frac{4\pi^2 v_o}{K}. \tag{15}$$

At high T, the limiting behaviour is less apparent. However, it is a fair assumption that the weighting term is less influential as the fluctuations in h_i become very pronounced. Thus the unperturbed solution, $\Sigma = 0$, may be presumed to reflect the perturbed self-energy for an interface at high T. This suggests a divergent behaviour in the $k, \omega \to 0$ limit, consistent with the observation that roughened interfaces diverge over long lengthscales.

Following the renormalization group approach of Kosterlitz (1974) and José *et al.* (1977), we will formally analyze this behaviour. We expand h_0, h_1 and Σ in powers of v_o using (10)-(14) and we recover the expression for $\chi^{-1}(k,\omega)$ in terms of v_o. This requires a certain amount of tedious algebra, shown in detail in de Gennes (1971), and produces

$$\begin{aligned} \chi^{-1}(k,\omega) \;=\; & q^2\left(K^{-1} + \pi^3 K^{-2} v^2 \int_1^\infty dr\, r^{3-2\pi K}\right) \\ & -\imath\omega\Gamma^{-1}\left(1 + \frac{\pi^4 v^2}{\pi K - 1}\int_1^\infty dr\, r^{3-2\pi K}\right) + \mathcal{O}(v^4) \end{aligned} \tag{16}$$

where $v = v_o e^{-C_{onst}K}$ is used for convenience; the constant $C_{onst} \approx \pi^2/2$ is simply a consequence of Fourier transforming the *cos*() factor in (14). The integrals in (16) are subsequently assessed by separating each of them into two parts, integrating from

1 to b and from b to ∞ with the condition $0 < \ln b \ll 1$ or $b \to 1^+$. The small r parts of the integration can be combined with the original constant term (either K^{-1} or Γ^{-1}) to produce a new parameter value; the large r part of the integration can be rescaled so that the limits of integration are again from 1 to ∞. The scaling factor is absorbed in a redefined w and (16) can be rewritten with parameters $K(\ell)$, $\Gamma(\ell)$ and $v(\ell)$ where $\ell \equiv \ln b$. The equivalence between (16) and this new expression implies the differential recursion equations

$$\begin{aligned} \frac{dK(\ell)}{d\ell} &= -\pi^3 v^2(\ell) && (17) \\ \frac{1}{2}\frac{dv^2(\ell)}{d\ell} &= -(\pi K(\ell) - 2)v^2(\ell) && (18) \\ \frac{d\ln\Gamma(\ell)}{d\ell} &= -\frac{\pi^4 v^2(\ell)}{\pi K(\ell) - 1} && (19) \end{aligned}$$

with the limiting behaviours $f(\ell = 0) = f$ for f being K, Γ or v.

By comparing the expressions (17), (18) and (19) with Nelson *et al.* (1977) and José *et al.* (1977) in their comparative analyses of the 2D Coulomb gas and the XY model, we observe that the first two equations are basically identical to their recursion relations. This implies the similarity in the nature of the static transition behaviour of this model to theirs. By defining a new variable $x(\ell) \equiv \pi K(\ell) - 2$ and substituting into (17), we obtain

$$\frac{1}{2}\frac{dx^2(\ell)}{d\ell} = -\pi^4 x(\ell) v^2(\ell). \qquad (20)$$

Comparing this equation to (18), we identify a conserved quantity

$$x^2(\ell) - \pi^4 v^2(\ell) = x^2 - \pi^4 v^2 = C_{onst} \qquad (21)$$

and, assuming $x(\ell) > 0$, we see that (19) drives $v(\ell)$ to 0 as $\ell \to \infty$; this indicates that the influence of the periodic weighting function disappears and thus the interface roughens. The roughening transition can then be considered the low temperature end point of a line of critical points with $v(\infty) = 0$; at this end point, we must have $x(\infty, T_R) = 0$ or $K(\infty, T_R) = 2/\pi$. This value for K is *universal* (ie. independent of any modifications to the basic Hamiltonian).

Another insight which can be derived from (20) when it is evaluated at $\ell = \infty$ for $T \geq T_R$ is how $K(\infty, T)$ varies with T as $T \rightarrow T_R^+$. Since $v(\infty) = 0$,

$$x^2(\infty) = x^2(\ell) - \pi^4 v^2(\ell) \qquad T \geq T_R; \tag{22}$$

the right hand side can be expanded about T_R in powers of $T - T_R$, noting that the constant term disappears at T_R due to $x(\infty, T_R) = 0$. Thus, to lowest order

$$x(\infty) = \sqrt{C_{onst}(T - T_R)}; \tag{23}$$

this indicates that $K(\infty)$ (and thus $\Gamma(\infty)$ as we shall see below) has an unusual square-root cusp as $T \rightarrow T_R$. Also, since $x(\infty, T_R) = 0$ and recall that $v \equiv v_o e^{-\pi^2 K/2}$, we obtain

$$K(\infty, T_R) = \frac{2}{\pi} + \pi^2 v_o e^{-\pi^2 K(\infty, T_R)/2} \tag{24}$$

Setting $v_o = 1$ as an approximation of a discrete lattice, (24) can be solved by iteration, giving $k_B T_R \sim 1.45\ J$. This is consistent with computer simulation results for the dG model (Shugard, Weeks and Gilmer 1978).

The third recursion equation (19) contains information about the dynamical behaviour in Γ. Combining (17) and (19) to eliminate v and integrating $\ell = 0$ to ∞, we arrive at

$$\frac{\Gamma(\infty, T_R)}{\Gamma} = \frac{\pi K(\infty, T_R) - 1}{\pi K - 1} \tag{25}$$

Thus, Γ scales with K whose behaviour was discussed above. The consequences for the statics and dynamics of the interface are immediate; the average growth rate I of the crystal is related to the response to a spatially and temporally uniform driving force when the stabilizing field is removed, $H^2 = 0$. From the interface definition (11), we obtain the growth rate I to first order in $\Delta\mu$ and use (12) for the high-T response function to define its high temperature limit;

$$\begin{aligned} I &= \lim_{\omega \to 0} -i\omega\chi(k=0,\omega)\frac{\Delta\mu}{T} && (26) \\ &= \Gamma(\infty)\frac{\Delta\mu}{T} \qquad (T \geq T_R). && (27) \end{aligned}$$

This result is consistent with conventional theories of crystal growth (Weeks and Gilmer 1979); for small driving forces at high temperatures, they predict to first order in $\Delta\mu$ a limiting form of $I = E_{vap}\Delta\mu/T$ where E_{vap} is the equilibrium evaporation rate. Since $v(\infty) = 0$ above T_R, the response function $\chi(k,\omega)$ has the same form as χ_0 but with the scaled parameters. Also, since we expect the high T limiting form of the unscaled χ to also be χ_0, the scaled and bare parameters are identical in this limit for all ℓ (ie. $\Gamma(\infty) \simeq \Gamma$ for $T \to \infty$) and we then identify Γ with the evaporation rate E_{vap}.

At $T < T_R$, the behaviour of the response function is quite different. As $T \to T_R^-$, it can be shown to have a limiting form

$$\chi(k,\omega) = \frac{1}{K^*(k^2 + \xi^{-2}) - i\omega/\Gamma^*} \qquad (28)$$

with a finite correlation length ξ and renormalized parameters K^* and Γ^*. This form is not unexpected; since Σ has been shown to be well-behaved (ie. equation (15)) at low T, a functional form for χ^{-1} similar to χ_0^{-1} (ie. linear in ω and quadratic in k) is reasonable. Then (26) predicts a rate $I = 0$ for $T < T_R$ to first order in $\Delta\mu/T$.

This is consistent with the fact that, for a perfect lattice, the growth mechanism is primarily via nucleation. Nucleation theory gives $I \propto e^{-C_{const}/\Delta\mu}$ so one would expect that all terms in a power series expansion about $\Delta\mu = 0$ would vanish.

At equilibrium (ie. $\Delta\mu = 0$), the spatial correlations between height fluctuations can be calculated from the fluctuation-dissipation theorem

$$\langle | h_0(k,\omega) |^2 \rangle = \frac{2}{\omega} \Im \{\chi(k,\omega)\} \tag{29}$$

where $\Im\{\mathcal{X}\}$ signifies the imaginary part of $\mathcal{X}$. Specifically, for large r and t at $T \geq T_R$,

$$\langle [h_0(r,t) - h_0(0,0)]^2 \rangle \cong \frac{K(\infty)}{2\pi} \log \left\{ \max \left(r^2, \frac{4\Gamma(\infty)}{K(\infty)} t \right) \right\} \tag{30}$$

based on results of de Gennes' (1971). By inspection, we can see that there are space/time correlations which diverge logarithmically above T_R. The large r limit of the equal time correlation function gives a measure of the interface width and (30) shows that it is logarithmically divergent for all $T \geq T_R$. Similarly, this is true of the large t time-correlation function. Also, (30) suggests that the correlation function ξ is ∞ above T_R. Below T_R, we can see from (19) and (28) that the correlation function approaches an asymptotic value exponentially fast. Thus the interface width and the correlation function are finite below T_R. Exactly at the roughening temperature, $K(\infty) = 2/\pi$ so the width is predicted to show an abrupt change from its finite value below T_R to

$$\langle [h_0(r,t) - h_0(0,0)]^2 \rangle \cong \frac{2}{\pi^2} \log r \qquad T = T_R \tag{31}$$

This behaviour has been observed in simulation (Shugard, Weeks and Gilmer 1978) and to some degree in experiments (Rolley, Balibar and Gallet 1986; Wolf, Balibar and Gallet 1983; Wolf et al. 1985; Gallet, Balibar and Rolley 1987).

2.1.2 Summary of Roughening Transition Characteristics

A number of other results can also be extracted from the renormalization group approach through careful analysis. We list below a summary of important transition behaviours including some of those mentioned earlier; included are the transition temperature, surface tension, step free energy, correlation length, interface width and surface curvature. Additional details can be found in review articles (Weeks and Gilmer 1979; van Beijeren and Nolden 1987; Ohta and Kawasaki 1978).

Roughening Transition Temperature The transition temperature can be determined with reasonable accuracy for the discrete Gaussian model (an SOS-type model with quadratic interaction energy),

$$k_B T_R \cong 1.45\ J \tag{32}$$

which have been confirmed by simulations (Shugard, Weeks and Gilmer 1978). It should be noted that this is **not** a universal quantity but can be extracted from the flow equations for different models by an appropriate choice of parameters.

Surface Tension The surface tension (surface energy per unit area) has a weak singularity at the roughening transition. From below T_R, it behaves like (Kosterlitz 1974)

$$\gamma \approx \gamma_0 e^{-A/\sqrt{T-T_R}} \qquad T \to T_R^- \tag{33}$$

where γ_0 and A are non-universal. Note that all derivatives of γ are smooth functions of T which vanish at T_R; this is typical of the Kosterlitz-Thouless transition and make detection of the transition very difficult.

Step Free Energy The step free energy is defined as the difference of free energy between interfaces with and without a step (a vertical dislocation of one lattice unit). It has the form near T_R

$$E_s = \begin{cases} E_0 e^{-B/\sqrt{T_R-T}} & T \to T_R^- \\ 0 & T \geq T_R \end{cases} . \tag{34}$$

Again, E_0 and B are non-universal. This expression is obtained from the analysis of the XY model (Swendsen 1978); the step free energy is the dual conjugate of the XY inverse spin-spin correlation function.

Correlation Length The correlation length is the characteristic distance between thermal excitations on the crystal surface. Below but near to T_R, it behaves like

$$\xi = \begin{cases} \xi_0 e^{B/\sqrt{T_R-T}} & T \to T_R^- \\ \infty & T \geq T_R \end{cases}$$

where B is the same as in (34) and ξ_0 is again non-universal. It is the dual conjugate of the XY model vortex-vortex correlation (Ohta and Kawasaki 1978).

Interface Width The height-height correlation (30) of a single-valued interface (like in an SOS model) provides a good approximation of interface width behaviour. From the analysis of its behaviour (Chui and Weeks 1976; Ohta and Kawasaki 1978), the mean square width near T_R follows

$$\langle w^2(T)\rangle \propto \begin{cases} C + \sqrt{T_R - T}^{-1} & T \to T_R^- \\ W_\circ + D\sqrt{T - T_R} & T \to T_R^+ \end{cases} \tag{35}$$

Here, C and D are not universal but W_0 is the universal value $2/\pi^2$.

Surface Curvature The radius of curvature of a {100} surface on a bulk inclusion (droplet) is predicted to jump from infinite value at $T < T_R$ to a universal finite value at T_R (Jayaprakash, Saam and Teitel 1983)

$$R_c = \frac{\pi R_0 k_B T_R}{2\gamma a^2} \tag{36}$$

where R_0 is the distance from tangent place at the surface to the center of the droplet, γ is the surface tension and a is the lattice unit length. The behaviour of a finite volume is discussed in greater depth in Section 2.2.

Thus, the equilibrium roughening transition is characterized by the vanishing of the step free energy, the divergence of the interface width, the divergence of the correlation length and a jump in the surface curvature. In the real world, the transition appears on a planar interface as the divergence of the width at long lengthscales from a finite value at T_R; thermal fluctuations overwhelm it, changing its appearance from a flat, facetted plane to a rough, wandering surface. This behaviour will be demonstrated in Section 5.1 using computer simulation methods.

2.2 Equilibrium Crystal Shapes

The previous section examined the behaviour of an infinite planar interface near its transition temperature. In the context of a enclosed volume (ie. a crystal droplet or bulk inclusion) in the thermodynamic limit $V \to \infty$, this is identical to studying the faces of the inclusion which have the orientation {100}; surfaces with any other orientation have $T_R = 0$ and are rough at all finite T. Since the roughened surface is curved and the facetted regions flat for $T < T_R^{\{100\}}$, the equilibrium crystal shape (ECS) demonstrates a marked transition behaviour at $T_R^{\{100\}}$; the facets disappear and it becomes continuously curved. The Wulff construction provides an indispensable tool for studying this change. The simple recipe proposed by Wulff (1901) exactly defines the temperature-dependent ECS. It requires only an expression for the surface

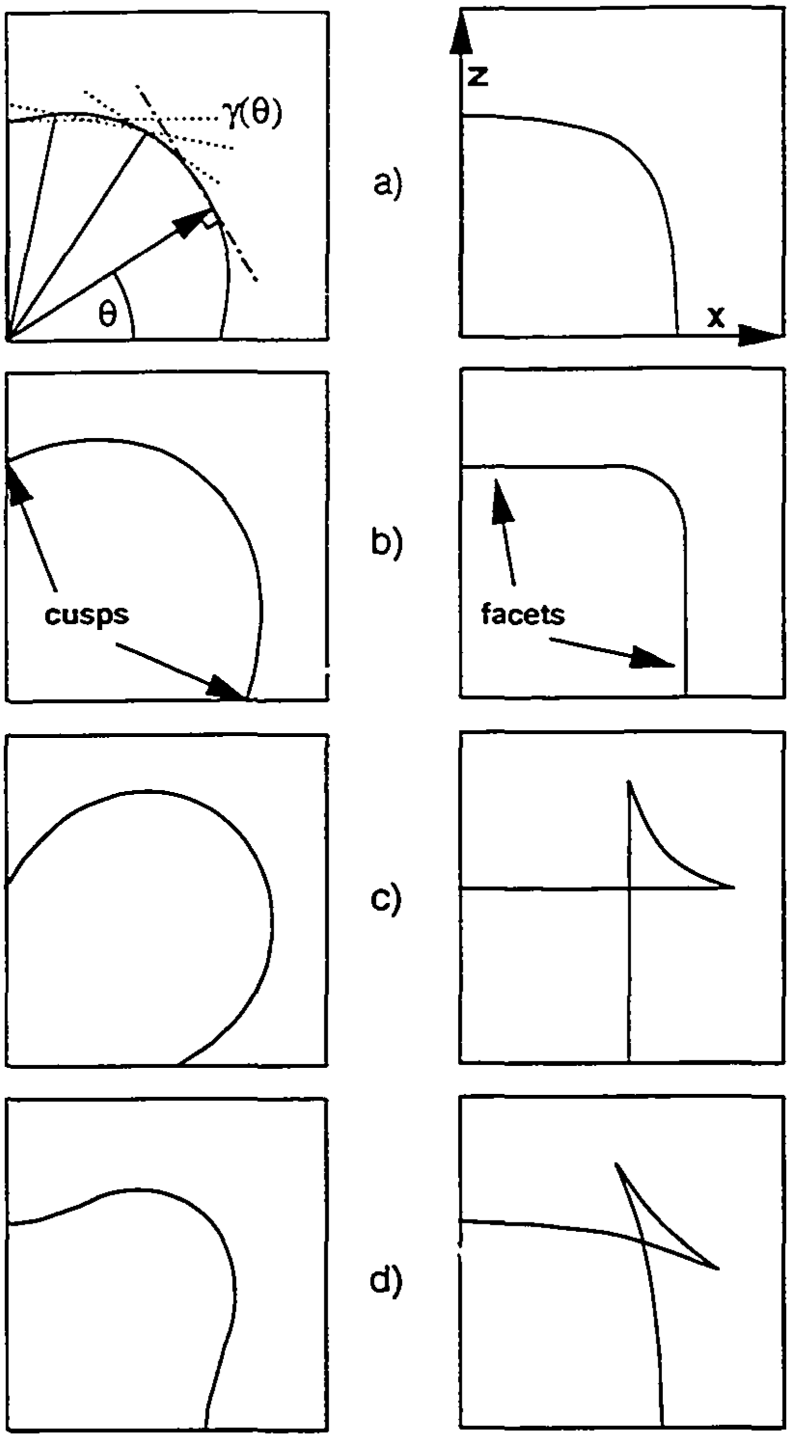

Figure 9: The Wulff construction for a simple cubic crystal. The plot pairs are the polar plot of a hypothetical surface tension $\gamma(\theta,\phi)$ and the corresponding equilibrium crystal shape. They approximately represent the cross-section of a simple cubic Ising crystal with nearest neighbourhood interaction a) at a temperature T above the roughening temperature T_R, b) at a finite temperature $T < T_R$ and c) at $T = 0$. The final pair d) is of a possible surface tension which would produce a cusp in interface. Note that cusps in the surface tension produce facets in the equilibrium shape.

tension $\gamma(\hat{n},T)$ as a function of temperature T and the unit orientation vector $\hat{n}$ originating at the center of the crystal (see Figure 9).

Let us suppose a microscopically smooth surface $S(R,\hat{n})$ where R is the radius from the center of the inclusion to the surface in the direction of the vector $\hat{n}$. Given a fixed crystal volume V and the surface energy per unit area $\gamma(\hat{n})$, the ECS is the surface which minimizes the free energy of the crystal. The solution for $S(R,\hat{n})$ is found graphically (in cross-section) by the following recipe:

1. Draw a polar plot of the surface energy per unit area $\gamma(\hat{n})$
2. Draw a plane perpendicular to $\hat{n}$ at every point on the $\gamma(\hat{n})$ plot
3. Extract the inner envelope of the family of planes

The inner envelope is the equilibrium crystal shape to an overall scale factor given by the fixed crystal volume. Figure 9 shows the ECS defined by the Wulff construction for a simple cubic crystal lattice in cross-section at its center for temperatures above and below T_R and at $T = 0$. It is interesting to note that, as pointed out by Mark Holzer (1990b), the ECS appears to be an intensive state variable of this system. This would also suggest that the volume V is its corresponding extensive state variable and that the free energy of the system is described by $\delta F = S\ dV$ (all other state variables fixed). Thus the Wulff construction is really a recipe for a Legendre transform between the intensive/extensive variable pairs, surface tension (γ)/surface area (A) and equilibrium crystal shape (ECS)/volume (V).

The geometric relationship between γ and the ECS created by the Wulff construction can be simply derived from these plots. Using the ECS from Figure 9 a) as a reference, we restrict the analysis to x and z although it obviously includes y; the following refers to specifically to Figure 10. Choosing an arbitrary point (x_o, z_o) on the ECS, its tangent is extended until it intersects the z axis at z_1. The small angle

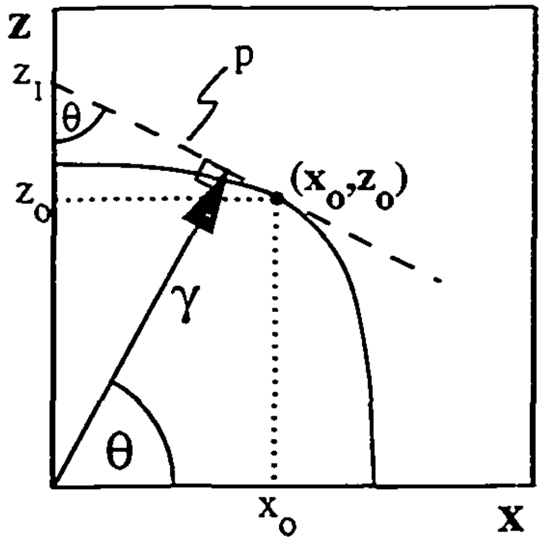

Figure 10: A geometric analysis of the ECS defines the surface tension γ as a function of angle for a vector originating at the center.

between the tangent and z axis is θ; its slope is $p = dz/dx = -\tan(\theta)$. The normal to the tangent which intersects the origin is thus γ. So far, we have just worked backwards through the recipe for the Wulff construction. The length of γ is simply

$$\begin{aligned}\gamma(\theta) &= \cos(\theta)z_1 \\ &= \cos(\theta)(z_o + px_o).\end{aligned}$$

Generalizing and inserting $p = -\tan(\theta)$, we find the surface energy per unit area from the ECS to be expressed by

$$\gamma(\theta) = \cos(\theta)(z - \tan(\theta)x). \tag{37}$$

In order to provide a firmer foundation for the use of the Wulff construction, we present a simple derivation of an analytic expression based on Landau and Lifshitz (1980). It will not be the most general analysis possible as it will rely on the piece-wise differentiability of $\gamma(\hat{n})$. However, we hope to benefit from its simplicity and clarity.

In this spirit, we begin by noting that the ECS produced by a Wulff construction is always convex; this can be seen in Figure 9 d) where the tendency to loop results in a cusp in the always-convex ECS. This is significant insofar as a convex shape can always be separated into upper (+) and lower (−) parts, defined by being in *line-of-sight* from $z = +\infty$ and $-\infty$ respectively (see Figure 11). The choice $\hat{z}$ is arbitrary

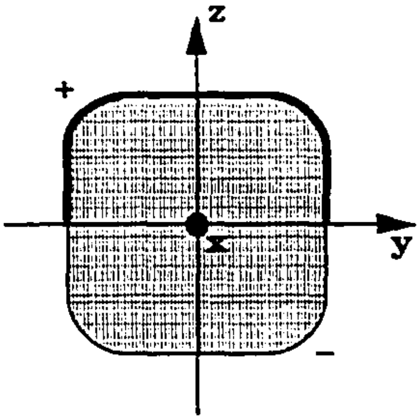

Figure 11: Any convex shape can be broken down into two unique components; half which is in *line-of-sight* of a point at $z = +\infty$ and half which is only seen from $z = -\infty$. The choice of $\hat{z}$ is arbitrary but is usually chosen to take advantage of any symmetry in the shape.

but is usually chosen to take advantage of any symmetry in the shape; the origin is assumed to be at its center.

Subsequently, the orientation on the surface of the crystal can be described as

$$\hat{n}_\pm = \pm \frac{(p_\pm, q_\pm, 1)}{\sqrt{1 + p_\pm^2 + q_\pm^2}} \tag{38}$$

where we use +/− to indicate *upper*/*lower*, parametrizing the surface $S(x, y, z) = z_\pm(x, y)$; we have used the partial derivatives p, q defined

$$p_\pm \equiv \frac{\partial z_\pm}{\partial x} \qquad q_\pm \equiv \frac{\partial z_\pm}{\partial y}. \tag{39}$$

The surface free energy per unit area of an infinitesimal surface element which has been projected upon the 2D viewing plane $(x, y, 0)$ is then

$$\epsilon_\pm = \gamma(\hat{n}_\pm)\sqrt{1 + p_\pm^2 + q_\pm^2}. \tag{40}$$

The subsequent minimization of the surface energy for fixed volume V can then be done through the variational expression

$$\delta \int dx\, dy\, (\epsilon_+ + \epsilon_- - 2\lambda(z_+ - z_-)) = 0 \tag{41}$$

where λ is a Lagrange multiplier. Using (39), we obtain

$$\sum_\pm \int dx\, dy \left(\frac{\partial \epsilon_\pm}{\partial p_\pm} \frac{\partial \delta z_\pm}{\partial x} + \frac{\partial \epsilon_\pm}{\partial q_\pm} \frac{\partial \delta z_\pm}{\partial y} \mp 2\lambda\, \delta z_\pm \right) = 0.$$

This in turn can be transformed using the method of partial integration, knowing that $\delta z_\pm = 0$ everywhere beyond the crystal surface;

$$\sum_\pm \int dx\, dy \left(\frac{\partial}{\partial x} \frac{\partial \epsilon_\pm}{\partial p_\pm} + \frac{\partial}{\partial y} \frac{\partial \epsilon_\pm}{\partial q_\pm} \pm 2\lambda \right) \delta z_\pm = 0.$$

At this point, the integrations can be separated since $\delta z_\pm(x, y)$ are independent variations and thus the integrand itself must be zero for each of + and −;

$$\mp 2\lambda = \frac{\partial}{\partial x} \frac{\partial \epsilon_\pm}{\partial p_\pm} + \frac{\partial}{\partial y} \frac{\partial \epsilon_\pm}{\partial q_\pm}. \tag{42}$$

The solution to this is

$$\begin{aligned} \epsilon_\pm &= \pm\lambda(z_\pm - \frac{\partial z_\pm}{\partial x} x - \frac{\partial z_\pm}{\partial y} y) \\ &= \pm\lambda(z_\pm - p_\pm x - q_\pm y). \end{aligned} \tag{43}$$

Looking back at our geometric expression (37), we can see that it is identical to (43), except for the scaling factor λ, where from (40) we get $\epsilon = \gamma/\cos(\theta)$ and from (39)

p is again the slope $dz/dx = -\tan(\theta)$. Taking the partial derivatives of (43) and rearranging, the surface of the crystal shape is then described by

$$x = \mp\lambda^{-1}\frac{\partial\epsilon_\pm}{\partial p_\pm} \tag{44}$$

$$y = \mp\lambda^{-1}\frac{\partial\epsilon_\pm}{\partial q_\pm} \tag{45}$$

$$z = \pm\lambda^{-1}\left(\epsilon_\pm - p_\pm\frac{\partial\epsilon_\pm}{\partial p_\pm} - q_\pm\frac{\partial\epsilon_\pm}{\partial q_\pm}\right) \tag{46}$$

Thus, given the surface free energy per unit area, the crystal shape $S(x, y, z)$ can be constructed from (44)-(46).

As an aside, we note that the Langrange multiplier λ can be defined by thermodynamical analysis (Wolf et al. 1985) as

$$\lambda = \frac{1}{2}\frac{\rho_s - \rho_l}{\rho_l}\delta P \simeq \frac{\gamma}{R}$$

where ρ_s and ρ_l are the solid and liquid (or vapour) densities and δP is the excess pressure of the liquid with respect to the equilibrium pressure on a flat interface. It is approximately related to the ratio of the surface tension to the surface radius of curvature.

Using the simple cubic lattice to illustrate a more specific application, the equilibrium crystal shape exhibits a distinct behaviour at the roughening transition; Figures 9 a), b) and c) approximately represent this behaviour. Below T_R (ie. 9 b)), the surface energy as a function of the orientation vector has cusps in the [100] directions. In terms of the ECS, this results in a flat, macroscopic facet of {100} orientation on each face, connected by smoothly curved regions. Since there are no cusps in any other directions, no other orientations of the surface exhibit facets or the transition behaviour. In the $T = 0$ limit, the facets are square and exactly bound each other with no intervening curved surface. Above T_R, $\gamma(\hat{n})$ is a smoothly differentiable function of angle; similarly, the ECS is continuously curved with no macroscopic facets. Thus, it is at T_R that the cusp in $\gamma(\hat{n})$ disappears and, with it, the facets.

In Section 5.2, we study the behaviour of a finite crystal volume using computer simulation. We examine the ECS of a simple cubic crystal, looking for indications of a transition. In the process, we extrapolate the idea of the ECS to specific measurable aspects of a physical crystal.

3 Non-Equilibrium Interfaces

Driven away from equilibrium, a crystal interface may exhibit a pattern generating instability; a common example is the formation of snowflakes. As we noted in the introduction, the underlying physics of this phenomenon is largely, although not completely, contained in the *Mullins-Sekerka instability* description. Let's consider a flat solid-liquid phase boundary at coexistence, similar to that discussed in Chapter 2. After relaxing to its equilibrium state, it is completely stable. If the temperature of the liquid phase is spontaneously lowered, the interface will become unstable and begin to move into the liquid. As the phase changes from liquid to solid, latent heat is released, warming the liquid along the interface and retarding its advance. This heat is diffused away into the liquid bulk and the interface continues its progress. Eventually a steady state is reached, the interface moving forward at a constant velocity, driven by a thermal gradient perpendicular to it. Perturbations of the interface will start to grow, maximizing the surface area and thus the redistribution of the latent heat. Finger-like growths will form as heat collects between the growing bumps, slowing the advance of the depressions and accelerating the tips; these *dendrites* typically sprout secondary branches along their sides as they grow. The dendrites are of a characteristic length scale which depends on the state of the system and the material involved. Despite the relative simplicity of the mechanism, it can produce very complicated structures as commonly observed in frost or snowflakes.

We shall illustrate the basic physics of the process by carrying out a linear stability analysis, both for a planar interface and for a spherical droplet. As we have mentioned before, the dendrite problem requires a much more complete treatment in order to develop a fully physical description. However, we will be able to provide ample foundation for our computer studies of the instability; our simulation model inherently contains all of the necessary physics. Through the linear stability analysis, we will identify the characteristic instability length scale associated with each interface geometry and show how they are related to the thermal diffusion and capillary (surface tension) lengths. Finally, we shall look at a steady state solution for the dendrite found at late times in the form of a parabolic needle crystal. The spherical tip radius or curvature will be related to the constant tip velocity.

3.1 The Linear Stability Analysis of a Planar Interface

When a planar interface is unrestrained by lattice influences (ie. roughened) and advancing with velocity v, an instability can arise wherein certain modes of the boundary are amplified and the interface exhibits a pattern selection behaviour. The basic mechanism behind this phenomenon was first described by Mullins and Sekerka (1963; 1964) who performed a linear stability analysis to define the dynamics of the process. Refinements to the description have subsequently been introduced (Langer 1987; Kessler, Koplik and Levine 1988) including the effects of the lattice anisotropy. However, the linear stability analysis is still the most effective way to present the essential instability. We will discuss the Mullins-Sekerka instability in the context of a thermal gradient produced by a latent heat of transition between the phases, one of which is undercooled. It should be noted that the analogy in terms of a chemical potential is equivalent and easily extracted from this analysis.

The growth rate of a pure substance is defined by the diffusion of the latent heat $\mathcal{L}$ from the interface. We define a dimensionless thermal field

$$u \equiv \frac{T - T_m}{\mathcal{L}/C} \tag{47}$$

where C is C_l, the heat capacity of the *liquid* phase. For analytic convenience, C_s of the solid phase can be assumed to be either approximately equal to C_l or zero; here, we avoid the question by assuming that the thermal conduction is restricted to the liquid phase, resulting in some asymmetry in the results but not changing the essential physics. We will re-introduce the influence of the solid phase through the interface continuity condition.

The interface is initially planar with a normal in the $\hat{z}$ direction; the average interface position is defined to be at $z = 0$ (ie. the frame of reference moves with the interface) with the solid bulk at $z \leq 0$. The problem is completely described by one dynamical equation, two boundary conditions and a continuity equation for the interface. The dynamical part is handled by the continuum diffusion equation

$$\frac{\partial T}{\partial t} = D\ \nabla^2 T \tag{48}$$

where D is D_s or D_l, the diffusion constants of the solid and liquid phases respectively. It is re-written using (47),

$$\nabla^2 u + \frac{2}{\ell}\frac{\partial u}{\partial z} = 0 \tag{49}$$

where ℓ is the characteristic lengthscale of thermal diffusion, $\ell = 2D_l/v$. The Gibbs-Thomson condition expresses the thermodynamic relationship between the interface curvature κ and the effective coexistence temperature;

$$T_\perp = T_m\left(1 - \frac{\gamma\kappa}{\mathcal{L}}\right)$$

which becomes with (47)

$$u_\perp = -\frac{\gamma T_m C}{\mathcal{L}^2}\kappa = -d_o\kappa \tag{50}$$

where γ is the surface tension. Thus, $u_\perp$ represents a local undercooling at the interface which increases with curvature. The parameter d_o is the capillary length, the characteristic lengthscale of the interface. The other boundary condition is

$$u(\infty) = -\Lambda \tag{51}$$

where Λ is the strength of the undercooling at infinity; a meaningful solution for $u(z)$ will require $\Lambda \equiv 1$. Finally, we include a continuity equation for the interface

$$v_\perp = -\left[D\nabla u \cdot \hat{n}\right]\Big|_{solid}^{liquid} \tag{52}$$

The entire problem is thus contained in (49)-(52).

Using (52), the solution to (49) is easily shown to be

$$u = \begin{cases} e^{-2z/\ell} - 1 & z \geq 0 \;\; (liquid) \\ 0 & z \leq 0 \;\; (solid) \end{cases} ; \tag{53}$$

Note that the undercooling is necessarily $\Lambda \equiv 1$; this is interpreted as the amount of latent heat produced being exactly the amount required to heat the undercooled liquid to T_m. A planar interface cannot sustain an excess or deficiency of latent heat and maintain a constant velocity. Further, note that the interface velocity v for $\Lambda = 1$ is undefined.

Figure 12 shows a schematic of this solution in terms of the initially planar interface. This leads to the first step of the linear instability analysis which, in its simplest form, uses the *quasi-stationary* approximation; the timescale for interface dynamics is assumed to be much longer than the timescale of thermal relaxation and subsequently the thermal field is always described by its stationary solution. The more general analysis can be done without the approximation (Sekerka 1967a; Sekerka 1967b; Langer 1980) but the essential behaviour is more clearly presented through its use.

A perturbation is now introduced at the interface of the form

$$h(\mathbf{x}) = h_0(\mathbf{x}) + \zeta(\mathbf{x}) \tag{54}$$

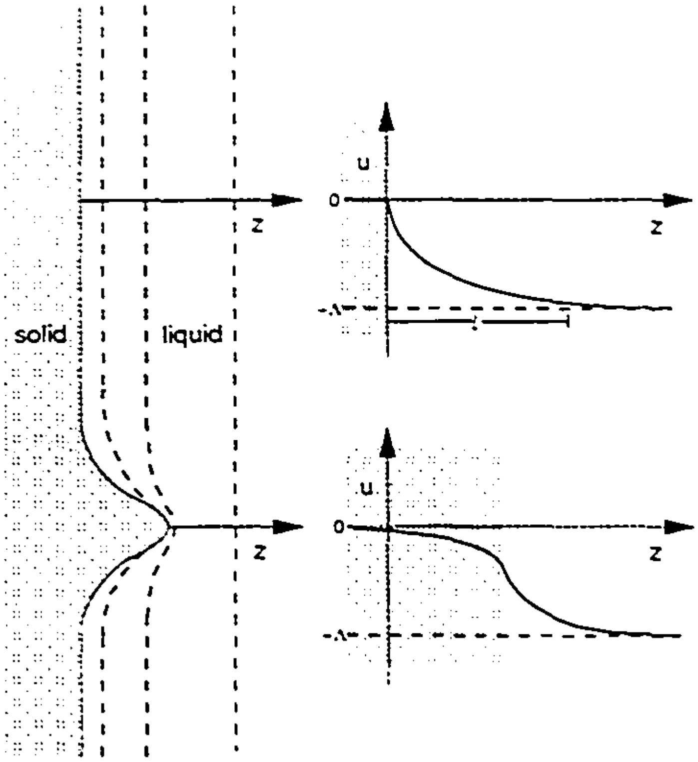

Figure 12: A diagram of the solution to the thermal diffusion equation using the quasi-static assumption; the dashed lines are isotherms. The interface is at the coexistence temperature T_m as modified by the local curvature (see equation (50)). The thermal gradient follows $e^{-2z/\ell} - 1$ perpendicular to the interface where the width has a characteristic size ℓ.

where $h_0(\mathbf{x}) = 0$ is the initial condition; ζ has the form of a superposition of modes consistent with linear theory

$$\zeta(\mathbf{x}) = \sum_k \hat{\zeta}(k) e^{i\mathbf{k}\cdot\mathbf{x}+\omega(k)t}. \tag{55}$$

where $\mathbf{k}$ is the wavenumber vector perpendicular to the interface velocity and $\omega(\mathbf{k})$ is an amplification factor for that mode. Since the modes are independent, we choose for the sake of simplicity $\omega(\mathbf{k}) = 0$ for all $\mathbf{k}$ except one. The stationary solutions for the thermal field in the liquid and solid must then be

$$u_l = e^{-2z/\ell} - 1 + \hat{u}_l(k) e^{i\mathbf{k}\cdot\mathbf{x}+\omega(k)t-qz} \tag{56}$$

$$u_s = \hat{u}_s(k) e^{i\mathbf{k}\cdot\mathbf{x}+\omega(k)t+pz} \tag{57}$$

respectively. The following expressions in p and q result from inserting (56) and (57) in (49);

$$\frac{2}{\ell}p + p^2 - k^2 = 0 \quad , \quad -\frac{2}{\ell}q + q^2 - k^2 = 0. \tag{58}$$

The amplitudes of the thermal field perturbations $\hat{u}_s(k)$ and $\hat{u}_l(k)$ are small (on the order of $\zeta(k)$) and can be evaluated by substituting $z = \zeta$ into (56) and (57) and linearizing;

$$\begin{aligned} \hat{u}_s(k) &= -d_o k^2 \hat{\zeta}(k) & (59) \\ \hat{u}_l(k) &= \left(\frac{2}{\ell} - d_o k^2\right) \hat{\zeta}(k). & (60) \end{aligned}$$

Following a similar linearization for the continuity condition (52), we find

$$\left(\omega(k) + \frac{2v}{\ell}\right) \hat{\zeta}(k) = D\left(q\hat{u}_l(k) + \alpha p \hat{u}_s(k)\right). \tag{61}$$

where we define $\alpha \equiv D_s C_s / D_l C_l$; we will henceforth refer to D_l as simply D. Substituting (59) into this expression and eliminating $\hat{\zeta}(k)$ then gives

$$\omega(k) = v(q - \frac{2}{\ell}) - D(q + \alpha p) d_o k^2 \tag{62}$$

which, in the quasi-static limit of the perturbation wavelength much smaller than the diffusion length, $k\ell \gg 1$, has the form

$$\omega(k) \cong kv\left(1 - C_{onst} d_o \ell k^2\right) \tag{63}$$

where it has been assumed $p = q \simeq k$ (ie. both phases have similar properties). The constant is $C_{onst} = (1 + \alpha)/2$ which is of order unity for most substances.

The behaviour of the Mullins-Sekerka instability is concisely described by (63); it is composed of two opposing terms which reflect the essential physics in the problem.

The positive part acts as a destabilizing growth term, causing the interface to grow away from its initially planar position at a rate proportional to the interface velocity. The negative part acts as a stabilizing, decay term; it is dependent on d_o, the capillary length, which defines the lengthscale of the surface relaxation. In effect, the pattern of the instability is a product of the competition between the thermal gradient increasing interface area and the surface tension reducing it, both mediated by the diffusion of the latent heat. Within the range of linear behaviour, the thermal gradient dominates at small k and the surface relaxation at large k. Figure 13 shows the form of (63) as a function of k.

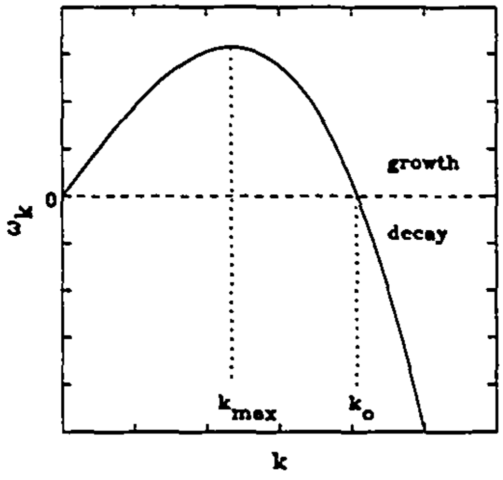

Figure 13: A linearized analysis of the Mullins-Sekerka instability yields a dispersion relation $\omega(k)$ where the interface $h(x)$ behaves like $e^{\omega_k t}$ at early times. The sign of $\omega(k)$ corresponds to growth (+ve) and decay (-ve). The mode of maximum instability k_{max} and critical mode k_o (ie. $\omega(k_o) = 0$) are indicated.

Several important features of (63) should be noted. All the positive values of $\omega(k)$ indicate growth modes while the negative ones are the decay modes. The maxima of $\omega(k)$ at k_{max}, is the mode of maximum instability; this mode will dominate at late times. The zero of $\omega(k)$ at k_0 is the critical mode at which $\omega(k)$ crosses over from growth to decay; this will be the upper k-limit of the instability. Using (63), the wavelength of maximum instability λ_{max} and of critical instability λ_0 can be derived in terms of the important physical lengths, ℓ and d_o;

$$\lambda_0 \equiv \frac{2\pi}{k_0} \cong 2\pi\sqrt{C_{onst}\ell d_o} \tag{64}$$

$$\lambda_{max} \equiv \frac{2\pi}{k_{max}} \cong 2\pi\sqrt{C_{onst}3\ell d_o} \tag{65}$$

where C_{onst} is as before. The instability lengthscale is thus related to the square root of the product of the two competing processes. In typical systems, d_o is microscopic, being of order of lattice constants in most materials of interest. In the modified Ising model presented in Chapter 4, it has been measured via simulation (see Section 5.3) to be about 1 lattice unit near the roughening temperature. On the other hand, the diffusion length is usually macroscopic, being several orders of magnitude large than d_o.

3.2 The Linear Stability Analysis of a Spherical Interface

When the interface bounds a solid bulk inclusion in a liquid background, the instability is characterized somewhat differently. In fashion similar to the planar case, we will first consider a perfectly spherical droplet of a pure material in an undercooled melt. Then we will consider a perturbation on the surface of the sphere. Note that, strictly speaking, there is no steady-state solution to this problem since the rate of growth is radially dependent.

Let us assume an initial radius $r = R_o$ on a perfect sphere centered on the origin in a melt undercooled to $\Lambda \equiv -u(\infty)$. Once again using the quasi-stationary approximation, we see that the diffusion equation satisfies Laplace's equation for all r; applying (50) at the sphere's boundary, we find

$$u(r) = \begin{cases} -\Lambda + \frac{R_o}{r}\left(\Lambda - \frac{2d_o}{r}\right) & r > R_o \\ -\frac{2d_o}{R_o} & r \leq R_o \end{cases} . \tag{66}$$

Then the continuity condition (52) is used to define the rate of growth at the interface $r = R_o$

$$v_r = \frac{dR_o}{dt} = \frac{D}{R_o}\left(\Lambda - \frac{2d_o}{R_o}\right). \tag{67}$$

This is the solution for the growth (or decay) of perfect sphere. Noise, imperfections or fluctuations on the surface or in the thermal field will introduce interface perturbations.

Consider a perturbation on the spherical interface in terms of the radius in polar coordinates;

$$R(\theta, \phi) = R_o + \Sigma_j \rho_j \mathcal{Y}_{j,m} e^{\omega_j t} \tag{68}$$

where ρ_j is a small initial perturbation amplitude, $\mathcal{Y}_{j,m}$ are the spherical harmonics and ω_j is the amplification factor. Once again, we will isolate a single mode j. Then it follows that the thermal field has the form

$$u(r, \theta, \phi) = u_0(r) + \hat{u}_j(r)\mathcal{Y}_{j,m} e^{\omega_j t} \tag{69}$$

with the solutions to the thermal diffusion perturbation amplitude in terms of unknown coefficients a and b

$$\hat{u}_j(r) = \begin{cases} a_j / r^{j+1} & r > R \\ b_j r^j & r \leq R \end{cases} \tag{70}$$

where the smallest j-mode is $j = 2$ ($j = 0$ is simply a displacement and $j = 1$ is discarded since the perturbation is around the equilibrium shape). Expanding the surface curvature in terms of R^{-1} to first order

$$\kappa(R,\theta,\phi) \simeq \frac{2}{R} + \frac{\Theta}{R} + O(R^{-2}) \tag{71}$$

where Θ is the angular part of the Laplacian with eigenstates $\mathcal{Y}_{j,m}$ and eigenvalues $j(j+1)$, we can linearize (69) and apply the Gibbs-Thomson relation (50) using (71);

$$\begin{aligned} a_j &= \left(\frac{v_r R_o^{j+1}}{D} - (j-1)(j+2)d_o R_o^{j-1}\right)\rho_j & (72) \\ b_j &= -(j-1)(j+2)\frac{d_o}{R_o^{j+2}}\rho_j & (73) \end{aligned}$$

We linearize the continuity equation (52)

$$\omega_j \rho_j = -\frac{2v_r}{R_o}\rho_j + \frac{(j+1)D}{R_o^{j+2}}a_j + \alpha D j R_o^{j-1} b_j$$

and define the amplification factors

$$\omega_j = \frac{(j-1)v_r}{R_o}\left[1 - \left(1 + j^{-1} + \alpha\right)\frac{d_o D j(j+2)}{v_r R_o^2}\right]. \tag{74}$$

Note that (74) is identical to the planar case (63) in the limits $R_o, j \to \infty$ and with finite $k = j/R_o$.

It is now useful to re-express (74) in terms of R^*, the critical radius from nucleation theory (see Appendix A.2). As a function of the undercooling Λ, it is

$$R^* \equiv \frac{2d_o}{\Lambda} \tag{75}$$

and thus the interface velocity is

$$v_r = \frac{2d_o D}{R_o}\left(\frac{1}{R^*} - \frac{1}{R_o}\right). \tag{76}$$

If we assume that R_o is slightly larger than R^*, the interface velocity will be small and positive and the droplet will grow. By inspection, (74) will then be negative for all values of j and all perturbations on the surface will decay. This means that the growing droplet will be spherically stable at $R^* \leq R_o < R_j^*$. To identify the radius at which the sphere will become unstable for a given j, we consider (74) for $\omega_j = 0$; this requires

$$\frac{v_r R_j^{*2}}{D d_o} = j(j+2)\left(1 + \frac{1}{j} + \alpha\right).$$

Inserting (76), we find

$$\frac{R_j^*}{R^*} = 1 + \frac{j(j+2)}{2}\left(1 + \frac{1}{j} + \alpha\right) \qquad (j \geq 2). \tag{77}$$

Thus, the lowest mode $j = 2$ becomes unstable at $R_2^* \simeq 11R^*$ assuming that the two phases have similar thermal characteristics ($\alpha \sim 1$).

3.3 Steady State Solutions for a Needle Crystal

We are also interested in understanding the nature of an interface instability much later in its development when it has become a long, tapered finger or *dendrite*. Following the lead of experimental evidence, we will presume the existence of a long, narrow, axially-symmetric needle crystal which has grown from an initial instability like that described in Section 3.1. We recall that the excess latent heat

$$\Lambda \equiv C\frac{T_m - T}{\mathcal{L}} \tag{78}$$

must be exactly 1 for there to be a steady state planar solution with constant velocity v. If $\Lambda > 1$, the interface will accelerate with no restraint mechanism and no steady-state is possible. If $\Lambda < 1$, an excess of heat is generated and the interface will slow until it finally stops, assuming that it remains planar. It can continue to move at a constant velocity (albeit at one place) if it bends backwards on all sides of some leading point; Figure 14 shows a steady state needle crystal with a tip with radius of

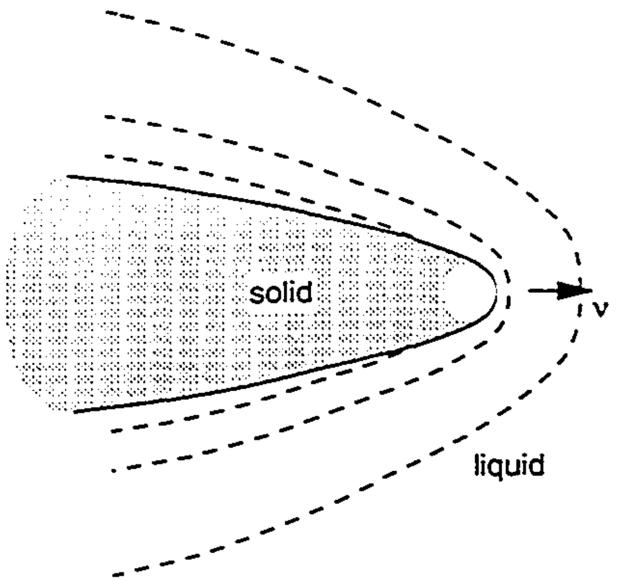

Figure 14: A schematic diagram of a steady-state needle crystal with a spherical tip moving at constant velocity. The dashed lines indicate the isotherms in the undercooled melt.

curvature ρ. The isotherms surrounding the tip diverge away from it as the heat is diffused away to the sides. For comparison, Figure 59 in Section 7.4 shows a number of simulation results for the thermal fields of growing instabilities. The only known analytic solutions for this situation are in the limit of zero surface tension with the interface exactly at the coexistence temperature T_m. In circular cross-section, these are known as the Ivantsov solutions (Ivantsov 1947); there also exist solutions for an elliptical cross-section (Horvay and Cahn 1961).

We will shall use equations (49)-(52) in parabolic coordinates μ, ν and θ to find solutions for the thermal field similar to (53). The coordinates are in an inertial frame moving with the needle's tip and are defined to be

$$\mu = (r - z)/\rho \qquad \nu = (r + z)/\rho$$

where ρ is the tip radius of curvature, r is the radial distance from the origin, z is along the needle axis and θ is the angle around the $\hat{z}$. The diffusion equation (48) is then written

$$\frac{\rho}{\ell(\mu+\nu)}\left(\nu\frac{\partial u}{\partial \nu}-\mu\frac{\partial u}{\partial \nu}\right)+\frac{1}{\mu+\nu}\left(\frac{\partial}{\partial \nu}\nu\frac{\partial u}{\partial \nu}+\frac{\partial}{\partial \mu}\mu\frac{\partial u}{\partial \mu}\right)+\frac{1}{4\mu\nu}\frac{\partial^2 u}{\partial \theta^2}=0 \qquad (79)$$

where the dimensionless thermal field u is defined by (47) and we have again assumed the quasi-stationary context. The needle crystal interface is then a surface $\nu_\perp(\mu,\theta,\tau)$ where τ is the dimensionless time $2vt/\rho$. The continuity equation (52) becomes

$$\nu_\perp+\mu\frac{\partial \nu_\perp}{\partial \mu}+(\nu_\perp+\mu)\frac{\partial \nu_\perp}{\partial \tau}=\begin{cases}\alpha\Upsilon/p & \textit{solid}\\ -\Upsilon/p & \textit{liquid}\end{cases} \qquad (80)$$

where p is the quantity known as the Péclet number

$$p\equiv\frac{\rho v}{2D}=\rho/\ell$$

and

$$\Upsilon\equiv\nu_\perp\frac{\partial u}{\partial \nu}-\mu\frac{\partial \nu_\perp}{\partial \nu}\frac{\partial u}{\partial \mu}-\frac{\nu_\perp+\mu}{4\nu_\perp}\frac{\partial \nu_\perp}{\partial \theta}\frac{\partial u}{\partial \theta}$$

For simplicity, we will ignore the effect of the Gibbs-Thomson relation and assume that u goes to zero at the interface (ie. as if it were flat). There is then a solution to (79) with $\nu_\perp=1$ for the thermal field

$$u=\begin{cases}0 & \nu\leq 1\\ -\Lambda+\frac{\Lambda E_1(p\nu)}{E_1(p)} & \nu>1\end{cases} \qquad (81)$$

where $E_1(X)$ is the exponential integral

$$E_1(X)=\int_X^\infty dx\frac{e^{-x}}{x}.$$

Combined with (80), the solutions (81) require the condition

$$\Lambda=pe^pE_1(p). \qquad (82)$$

This expresses a key relationship between the tip radius ρ and the tip velocity v through p; for a given undercooling and thermal properties (ie. heat capacity, diffusion constant and latent heat), there exists a critical tip curvature ρ which is associated with a specific velocity v. It has been shown to be roughly consistent with experiment (Glicksman 1984).

Unfortunately, this only determines their product and not each quantity. A more complete analysis is needed which also includes a finite surface tension and its inherent anisotropy. This appears to be provided by the microscopic solvability theory (see reviews (Langer 1987; Kessler, Koplik and Levine 1988)) which we will not need or examine in this thesis. Of particular importance is the role of the anisotropy which introduces a cusp in the solution for the needle interface, thereby stabilizing it and defining a unique pair of values for ρ and v associated with the largest tip velocity. These values of ρ and v depend directly on the strength of the anisotropy; reducing the anisotropy to zero in the description then causes the steady-state solution to disappear.

We will use results from each of these analyses, directly or indirectly, in comparisons with our simulation data presented in Chapters 6 and 7. In Section 6.1, we will explicitly check the predictions for a planar interface in the linear regime; our goal will be to reproduce the dispersion relation for the growth modes and identify the special critical and maximum instability modes. For reasons related to computational efficiency, we examine the behaviour in two dimensions; this does not affect the basic physics. In Section 6.2, we continue in the two dimensions, looking for the stability radius of a disk (as opposed to a sphere). Since the details of the prediction are important in this case, we re-derive some aspects of the analysis presented in Section 3.2 although, once again, the basic physics remains the same. Finally, in Chapter 7, we go beyond the linear behaviour to non-linear growth. However, since late-time descriptions are complex and difficult to apply, we continue to rely on our understanding of the Mullins-Sekerka instability as developed here. Specifically, in Section 7.4 we study the thermal fields associated with these growths and interpret them in terms of the anticipated linear behaviour. We validate this approach by directly comparing the solutions for the thermal fields with data from a moving, steady-state planar interface.

4 The Simulation Model

Our simulation model has been used to model many different processes which involve a thermal diffusion mechanism. These include first- and second-order phase transitions (Harris 1985), interface relaxation to an equilibrium roughened state (Jörgenson, Harris and Grant 1989), thermal conductivity (Harris and Grant 1988), dendritic growth (Harris, Jörgenson and Grant 1992) and numerous others. It has been shown to model thermal processes consistently in all these applications. We review the basic behaviour of the model and introduce an enhanced thermal diffusion algorithm for improved control. We also discuss alternate lattice geometries and configurations which have been used for various work presented in this thesis.

4.1 The Simple Cubic Ising Model With A First-Order Transition

Our model is based upon a regular, cubic lattice of N Ising spins ($\sigma = \pm 1$) of size $L_x \times L_y \times L_z$. The spin interaction is nearest neighbour and the spin energy is defined by the Hamiltonian

$$\mathcal{H} = -J \sum_{<ij>} \sigma_i \sigma_j - \Delta \sum_i \sigma_i \qquad J > 0.$$

The first term is the spin-spin interaction and the second term represents a uniform external field of strength Δ. As a lattice-gas model, the $+1$ spins are associated with an occupied site or *atom* and the -1 spins are vacant sites. With $\Delta = 0$, this model exhibits a second-order transition from an ordered to disordered state at the critical temperature $k_B T_c = 4.51151\ J$ (Pawley et al. 1984); the Boltzmann constant k_B is subsequently defined to be unity and will be dropped from further use. For convenience, all temperatures will be referred to in units of T_c of the 3D Ising model.

Since we are interested in modeling thermal diffusion-limited processes at an interface, it is necessary and desirable to modify the basic model so that it has a first-order phase transition and thus a latent heat. We do this by making Δ finite and introducing a degeneracy in the upper spin state $\sigma = -1$. To illustrate their effect, we shall derive a simple mean-field description for this model with a degeneracy.

For a system with Boltzmann statistics, the number of states for a given energy E is

$$\Omega(E) = \frac{N!\ \delta_+^{N_+}\ \delta_-^{N_-}}{N_+!\ N_-!}$$

where $N = N_+ + N_-$ and the degeneracies of the spin states are δ_+ and δ_-. The entropy density can then be defined as

$$\begin{aligned} s = \frac{S}{N} &\equiv \frac{1}{N}\ln(\Omega(E)) \\ &\simeq (n_+\ln(\delta_+) + n_-\ln(\delta_-) - n_+\ln(n_+) - n_-\ln(n_-)) \end{aligned} \qquad (83)$$

where we have introduced the number density $n = n_+ + n_- \equiv 1$ and the approximation $\ln(A!) \simeq A\ln(A) - A$. We define the degeneracy to be the ratio $\delta = \delta_-/\delta_+$; then using $n_+ = 1 - n_-$, we can eliminate δ_+ and δ_- except for a constant term $\ln(\delta_+)$ which is unimportant. In general we will want to use non-integer values for δ.

For convenience, we redefine the number densities in terms of the mean magnetization;

$$n_\pm = \frac{1 \pm \bar{m}}{2} \qquad \Longleftrightarrow \qquad \bar{m} = (n_+ - n_-) \qquad (84)$$

The meanfield spin energy is then

$$\epsilon \equiv \frac{E}{N} = -(\frac{1}{2}\alpha J\bar{m}^2 + \bar{m}\Delta) \qquad (85)$$

where α is the number of nearest neighbours (eg. $\alpha = 6$ in 3D) and the prefactor of

1/2 is for double-counting in the summation over the spins. This can be inverted to solve for $\bar{m}$ as a function of ϵ

$$\bar{m} = -\frac{\Delta}{\alpha J} \pm \sqrt{\left(\frac{2\Delta}{\alpha J}\right)^2 - \frac{2\epsilon}{\alpha J}} \tag{86}$$

The entropy density is

$$s = \frac{1}{2}\left(\ln\left(\frac{4\delta}{1-\bar{m}^2}\right) - \bar{m}\ln\left(\delta\frac{1+\bar{m}}{1-\bar{m}}\right)\right) \tag{87}$$

We then apply Boltzmann's principle, defining the temperature T,

$$\frac{\partial s}{\partial \epsilon} = \frac{\partial s}{\partial \bar{m}}\left(\frac{\partial \epsilon}{\partial \bar{m}}\right)^{-1} \equiv T^{-1}$$

where

$$\begin{aligned} \frac{\partial s}{\partial \bar{m}} &= -\frac{1}{2}\ln\left(\delta\frac{1+\bar{m}}{1-\bar{m}}\right) \\ \frac{\partial \epsilon}{\partial \bar{m}} &= -(\Delta + \alpha J\bar{m}) \end{aligned}$$

$$\Longrightarrow T = 2\frac{\alpha J\bar{m} + \Delta}{\ln\left(\delta\frac{1+\bar{m}}{1-\bar{m}}\right)} \tag{88}$$

Inverting (88), we get a recursive solution for $\bar{m}$ in terms of T;

$$\bar{m} = \tanh\left(\frac{\alpha J\bar{m} + \Delta}{T} - \frac{1}{2}\ln(\delta)\right). \tag{89}$$

By inserting (86) into (88), we find an expression for the temperature in terms of the average spin energy ϵ

$$T = \pm 2\sqrt{4\Delta^2 - 2\alpha J\epsilon}/\ln(\Pi) \quad \text{where} \quad \Pi = \delta\frac{\alpha J - \Delta \pm \sqrt{4\Delta^2 - 2\alpha J\epsilon}}{\alpha J + \Delta \mp \sqrt{4\Delta^2 - 2\alpha J\epsilon}}. \tag{90}$$

The solutions (89) and (90) are shown in Figures 15 and 16 respectively.

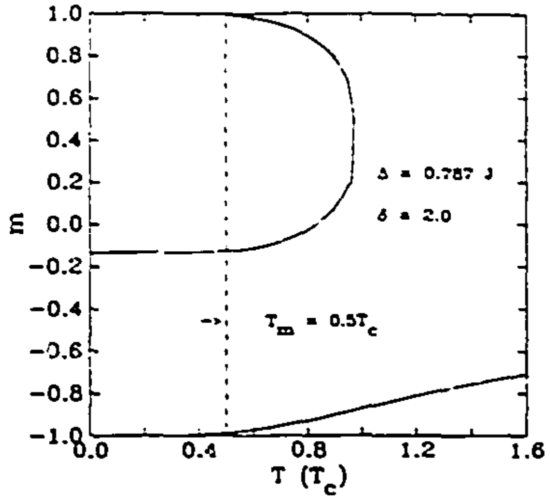

Figure 15: The meanfield solution for the average spin magnetization $m(T)$ for the Ising model. Although there are three branches to the solution, only two are physical. The first order transition is represented by the dashed line where the $m(T)$ passes from $m \sim 1$ below T_m to $m \sim -1$ above.

The path of the first-order transition is also shown in the figures even though it is not explicitly part of the solutions. Its existence can be shown by writing the meanfield partition function for two equivalent systems, one with $\bar{m} = m_+ \sim 1$ and the other with $\bar{m} = m_- \sim -1$;

$$\begin{aligned} \mathcal{Z}_i &= \sum_{\sigma=\pm1} e^{-\mathcal{H}_i/T} \\ &= e^{(J\bar{m}+\Delta)/T} + \delta\, e^{-(J\bar{m}+\Delta)/T} \end{aligned} \tag{91}$$

where $\mathcal{Z}_i$ is for site i and the partition function for the entire system of N spins can be constructed from $\mathcal{Z}_N = (\mathcal{Z}_i)^N$ because in meanfield the spins are non-interacting and localised. The two partition functions for the two systems will be designated $\mathcal{Z}_N^{\pm} = \mathcal{Z}_N(m_\pm)$. We know that at coexistence ($T = T_m$) the partition functions must be equal. Assuming that $m_+ = -m_- = m$ (which we will justify later), we then write

$$e^{(m_+J+\Delta)/T_m} + \delta e^{-(m_+J+\Delta)/T_m} = e^{(m_-J+\Delta)/T_m} + \delta e^{-(m_-J+\Delta)/T_m}$$

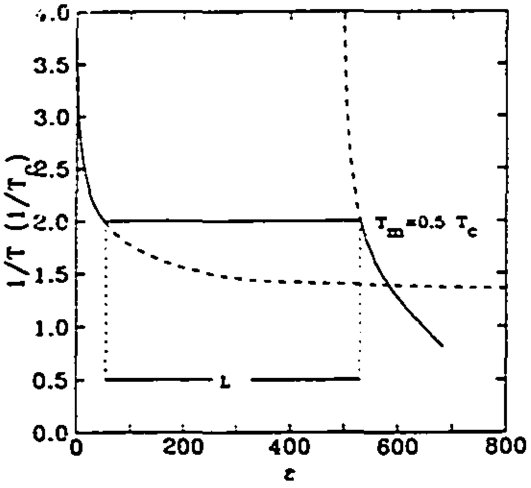

Figure 16: The meanfield solution to the average spin energy $\varepsilon(T)$ for the Ising model. Note that the physical solution is represented by the solid line. The width of the transition region corresponds to the latent heat $\mathcal{L}$.

$$e^{(mJ+\Delta)/T_m} + \delta e^{-(mJ+\Delta)/T_m} = e^{-(mJ-\Delta)/T_m} + \delta e^{(mJ-\Delta)/T_m}. \tag{92}$$

This is only true if $e^{\Delta/T_m} = \delta e^{-\Delta/T_m}$ or

$$\ln(\delta) = \frac{2\Delta}{T_m}. \tag{93}$$

We can see that, by raising δ into the exponential in the second term of $\mathcal{Z}_i$ (91) so that it appears like $e^{-(Jm+\Delta-T\ln(\delta))/T}$, the degeneracy acts like a temperature dependent field. At T_m, it exactly cancels Δ and the effective field is zero; we once again have the basic Ising model which we already know satisfies our original assumption $m_+ = -m_- = m$. The transition temperature has been established using the meanfield description but it should be noted that it is an exact result.

The main advantage of this model in terms of simulation studies of interfaces is its tunable coexistence temperature T_m. This makes it possible to study stable interfaces at a range of temperatures in a manner which is similar to manipulating the coexistence temperature of a real substance by changing the pressure. For example,

Figure 17 shows the phase coexistence boundaries of a material in a standard P-T (or pressure-temperature) phase diagram compared with a similar diagram for the modified Ising model. The pressure is analogous to the spin degeneracy and/or applied external field.

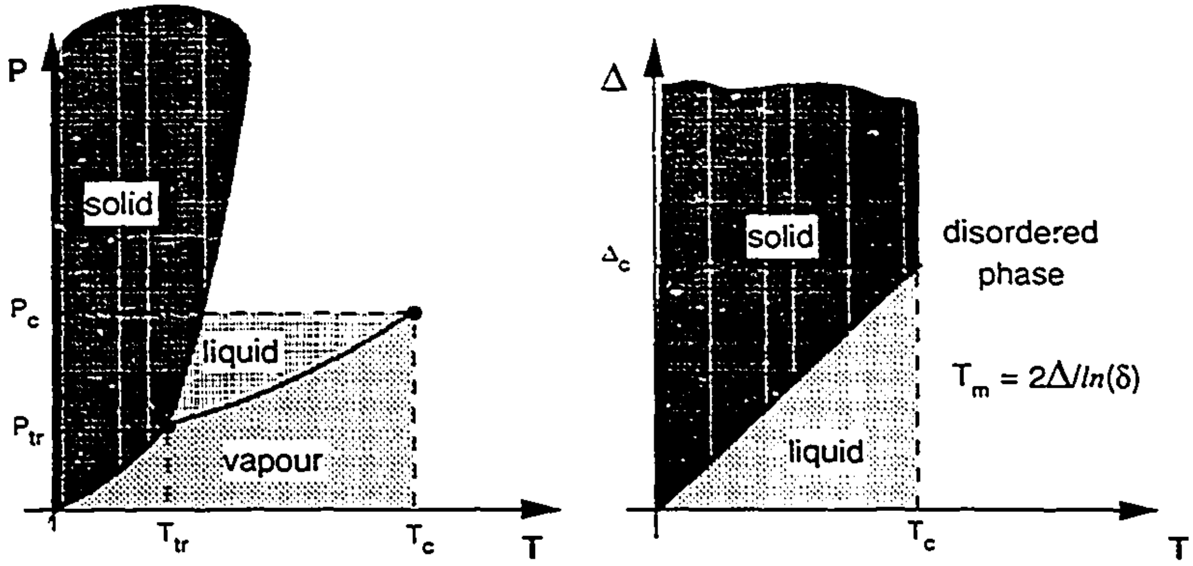

Figure 17: The pressure-temperature phase diagrams for a typical substance and for the Ising model with a first order phase transition. Shown are the critical point and triple point on the real P-T diagram and the critical point of the model P-T diagram. Note that δ is assumed fixed and greater than unity.

4.2 Spin Degeneracy and the Multi-Demon Creutz Algorithm

The dynamics of the system are controlled by a variant of the Creutz multi-demon algorithm (Creutz 1984; Creutz 1986). An $L_x \times L_y \times L_z$ lattice of non-interacting demons has a one-to-one correspondence with the spins. Each demon carries a non-negative amount of energy, ϵ_D. Spin sites are visited one-at-a-time at random. At each, a spin-flip to the other phase is attempted. The potential change in energy $\Delta\epsilon_\sigma$ for the flip is calculated and compared with the energy available in the demon which corresponds to the current site. The amount of energy available from the demon decides the course of action; the following events occur under the respective conditions:

Condition	**Action**
$\triangle\epsilon_\sigma < 0$	**flip and demon absorbs energy**
$0 < \triangle\epsilon_\sigma < \epsilon_D$	**flip and demon gives up energy**
$\epsilon_D < \triangle\epsilon_\sigma$	**no flip and no change in demon energy**

A Monte Carlo step (MCS) is defined to be when every spin site has been visited once, whether it flipped or not.

The spin degeneracy can be implemented in several ways. We have chosen to explicitly bias the upper spin state $\sigma = -1$ in our simulation engine. In lieu of flipping every spin of either phase to its opposite state (eg. $\delta = 1$), we visited x sites attempting a flip regardless of sign, then visited $x(\delta - 1)$ more sites and only attempted to flip them if they were $\sigma = 1$. This is algorithmically equivalent to flipping any spin to any one of the $\delta + 1$ possible states, including its own state and any degenerate states. The accuracy of any implementation is easily tested by checking if (93) holds for a range of Δ and/or δ.

Typically, after several 100 MCS, the spin and demon systems will be in thermal equilibrium. The distribution of demon energies will then conform to Boltzmann statistics. This makes it possible to define a local spin temperature in terms of the average energy (in time or space) of a group of demons; we follow the recipe from the canonical ensemble description (Reichl 1984) for the average energy of the system. The simplest derivation is for the $\Delta = 0$ and $\delta = 1$ case; it demonstrates the relationship more concisely than the general derivation. We first construct the partition relation for a single demon

$$\mathcal{Z}_i = \sum_{\epsilon_D=0}^{\infty} e^{-\epsilon_D/T}$$

where the demon energy ranges from 0 to ∞ in increments of $2J$; the increment $2J$ is the smallest possible exchange of energy between a demon and spin. Again, since the demons are non-interacting, the partition function for the entire system can be constructed $\mathcal{Z}_N = \mathcal{Z}_i^N$ and, thus, $\langle E_D \rangle = N\ \langle \epsilon_D \rangle$. From the canonical ensemble analysis, we use the formula

$$\begin{aligned}
\langle \epsilon_D \rangle &= \frac{\partial}{\partial \frac{1}{T}} \frac{1}{T} \ln \mathcal{Z}_i \\
&= \sum_{\epsilon_D=0}^{\infty} \epsilon_D e^{-\epsilon_D/T} / \sum_{\epsilon_D=0}^{\infty} e^{-\epsilon_D/T} \\
&= T \frac{2J/T}{e^{2J/T} - 1} && (94) \\
\Longrightarrow \quad & T = \frac{2J}{\ln(2J/\langle \epsilon_D \rangle + 1)}. && (95)
\end{aligned}$$

This result is derived using the relation

$$\frac{xe^{-x} + 2xe^{-2x} + 3xe^{-3x} + \ldots}{e^{-x} + e^{-2x} + e^{-3x} + \ldots} \equiv \frac{x}{e^x - 1}$$

where $x \equiv 2J/T$. For small x (high T or continuous spectrum of energies, $J \to 0$), we can expand e^x to first order and (94) becomes

$$\langle \epsilon_D \rangle \simeq T. \tag{96}$$

The more general case of $\Delta > 0$ and $\delta > 1$ can be done by separating the already non-interacting demons into two groups, those associated with *up* spins ($\sigma_\uparrow = +1$) and those associated with *down* spins ($\sigma_\downarrow = -1$). If we assume that the energy of a demon associated with a down spin (the lowest energy spin state) at $T = 0$ is zero, it is easy to show that the possible energy states of $\epsilon_{D_\uparrow}$ are nJ where $n \in [0, 2, 4, 6...]$ and of $\epsilon_{D_\downarrow}$ are $(n + 2)J - 2\Delta$. Their average energies are then

$$\langle \epsilon_{D_\uparrow} \rangle = \frac{x}{e^x - 1} \qquad \langle \epsilon_{D_\downarrow} \rangle = \frac{xe^x}{e^x - 1} - 2\Delta. \tag{97}$$

As is obvious, the field Δ introduces a bias into the definition of temperature. This makes it more awkward to accurately measure the temperature based on a simple average. Precise measurements require careful attention to the system parameters and the spin and demon configurations.

For general purposes however, the demon energy, averaged over space or time, provides a reliable measurement of the local or global temperature. This assumes, of course, that the average can be taken of an equilibrium or steady-state system on a temporal or spatial timescale which is short compared to any dynamical processes.

4.3 Thermal Diffusion

The Creutz algorithm has an inherent thermal diffusion where thermal energy is passed from demon to demon via the spin-flip mechanism. This process has been studied (Harris and Grant 1988) and it has been shown to give a good account of thermal diffusion in a dynamic context. However, it has the drawback of being strongly dependent on temperature since the rate of spin-flip is related to the strength of thermal fluctuations. This makes controlling the diffusion process difficult and introduces complications into the analysis. We have therefore introduced an enhanced diffusion process which is independent of T and provides for ease-of-control. Thermal diffusion is modeled by having the demons randomly exchange positions (or equivalently, energies) via a Kawasaki-like exchange with no penalty. The demon exchanges are between randomly chosen nearest-neighbours and thus the demons perform a random walk in 3D. The walk is described in 1D by the probability of finding a specific demon (or its energy) a distance x away from its starting place at time t (Reichl 1984);

$$P(x,t) = \frac{e^{-x^2/2nta^2}}{\sqrt{2\pi nta^2}}$$

where n is the number of exchanges per unit time and a is the distance of the exchanges, the unit lattice spacing. This is equivalent to the 1D diffusion equation where the diffusion constant is $D = na^2/2$. In terms of the algorithm, $n = 1$ is defined to be when every demon site has been exchanged during one Monte Carlo pass; in general, n is the fraction of demons which have been exchanged in a single MCS. Extending this to higher dimensions, D is defined

$$D = \frac{na^2}{2d} \tag{98}$$

where d is the dimensionality. We can therefore directly control D by changing the number of demons which are exchanged in each MCS. This procedure has been tested extensively and has been shown to be consistent for n as high as 10 (ie. 10N demon exchanges occur per MCS). Normally, we use $n \sim 1$ or lower. In comparison, the intrinsic diffusion process is sufficiently weak at all values of T used in this study that it can be safely ignored.

An added advantage to this algorithm is that thermal field can be mapped out graphically providing insight into the thermal diffusion mechanism and its effect on interfaces. In Section 7.4, we will examine the thermal fields associated with the Mullins-Sekerka instability driven by a thermal gradient. We will be able to further define the thermal characteristics of the model and relate them to the critical lengthscales of the instability.

4.4 Configuring the Simulations

The simulation systems can be configured in a variety of lattice sizes and shapes, interface geometries and initial conditions, depending on the physical context which is being modeled. Here we shall review the basic configurations and make a special note of lattice and interface geometries in the next Section.

All the simulation trials were on regular, cubic lattices of dimensions $L_x \times L_y \times L_z$. For reasons of memory alignment, L was usually a power of 2. With currently available hardware, the largest possible system sizes were approximately 10 million ($\approx 10^7$) spin or sites. Due to time constraints, we generally limited ourselves to 2 million sites (eg. 128^3 lattice). The spins are contained in Boolean values, having only two values, but the accompanying $L_x \times L_y \times L_z$ demon system can have greater range of values and usually requires the greatest amount of memory. Due to the fact that cpu speed was usually the bottleneck, no real attempt was made to optimize memory usage; the bulk of our efforts was spent on developing the speed of the algorithm.

A finite number of Monte Carlo steps are always required to allow the spin and demon systems to *relax* into an equilibrium state. In order to limit the effects of relaxation, the spin and demon systems were both initialized close to thermal equilibrium with each other. For the spins, the meanfield expression (89) was used to introduce random bulk fluctuations appropriate to the chosen temperature. The average demon energy was extracted from (96) and the total energy was distributed randomly in units of $2J$. Relaxation times were limited to several hundred MCS. No attempt was made to initialize the system with a thermal gradient; since thermal diffusion is necessarily faster than the interface dynamics (in order to satisfy the quasi-static approximation of Chapter 2), gradients are always in place before the initial relaxation has been completed. Systems pre-initialized with gradients were tested without finding any noticeable advantage; it was found to be sufficient to ignore the early times of each simulation trial.

The system's boundaries were handled in two ways: First, periodic boundary conditions were applied on the four sides perpendicular to the $\hat{x}$ and $\hat{y}$ directions for both the spin and demon systems. Second, the two sides perpendicular to the $\hat{z}$ directions (top and bottom) were each pinned to the desired phase and maintained at a constant temperature via a heat bath, using the Metropolis algorithm (Metropolis et al. 1953). For certain simulations involving enclosed volumes (finite crystals in Chapter 5), the four sides were periodic for the spin system but maintained at constant temperature.

The bulk phase interfaces were initialized perfectly flat without thermal fluctuations; at finite temperatures, equilibrium surfaces display their own thermal fluctuations, either as small flat islands (micro-facets) on an otherwise flat surface or as random variations in surface height (roughness). The planar interfaces were initially perfect planes and the droplets were perfect cubes. As mentioned before, an initially flat interface will relax to its equilibrium state very quickly (depending on the rate of thermal diffusion and size of the latent heat). In non-equilibrium contexts, local steady-state is usually reached just as quickly.

4.5 Lattice and Interface Geometries

While both the physical crystal structure and the simulation lattice are regular and cubic, there are several different ways to approach the simulation of a crystal interface. We shall look at several different applications of our model which we shall use in later sections and comment on the importance of the geometry. In Appendix A.1, we have included details for the definition of the crystal plane notation used below as well as the implementation of the following geometries in the standard algorithm.

{100} Block Planar Interface

The simplest configuration is the $L_x = L_y = L_z$ system with a bulk phase interface perpendicular to the $\hat{z}$ direction. When the nearest neighbours are defined to be the nearest sites in the $\hat{x}$, $\hat{y}$ and $\hat{z}$ direction, the system models a planar interface with

$\{100\}$ orientation. As will be shown, this interface exhibits a structural transition at a finite temperature $T_R < T_c$ which affects equilibrium and non-equilibrium behaviour. Figure 65 in the Appendix depicts the (001) plane. Note that the term *block* is used to distinguish it from the *slab* configuration described below.

$\{111\}$ Block Planar Interface

Using the same regular cubic lattice, we can change the definition of the nearest neighbours so that the system models a planar interface with $\{111\}$ orientation. This involves redefining the spatial representation of the lattice so that adjacent rows in an $\hat{x}-\hat{y}$ plane are staggered in a two-step cycle. Similarly, vertically adjacent $\hat{x}-\hat{y}$ planes are staggered in a three-step cycle (see Figure 66 in the Appendix). Thus, each site has three neighbours in the plane above ($\hat{z}$ direction) and three in the plane below. Aside from the redefinition of the nearest neighbours, the algorithm is identical to the $\{100\}$ system.

This re-orientation of the crystal interface is very important for studies of the Mullins-Sekerka instability. As we noted in Section 2.1, the $\{111\}$ interface in the simple cubic lattice has a roughening temperature $T_R = 0$ and it is roughened at all finite temperatures. Consequently, its behaviour is unmodified by the transition throughout the range of finite temperatures. This is particularly important at low T_m and for large undercooling when the interface may be far below $T_R^{\{100\}}$. If facets form perpendicular to the direction of the instability, its growth will be strongly inhibited. As we observe in Section 5.4, the response of a faceted interface to a driving force is weak and non-linear compared to a roughened interface.

It is worth noting that this nearest neighbour scheme provides access to several other crystal lattices. With some minimal changes, we can simulate the hexagonal close-packed structure (HCP). With somewhat more extensive modifications, we can produce the body-centered and face-centered cubic lattices as well. Time constraints kept us from exploring all of these possibilities.

{100} and {111} Slabs

Using either definition for the nearest neighbours, we can reduce the size of L_y so that $L_y \ll L_x$. This configuration is referred to as a *slab*. It has three advantages which are useful to us: First, we can run much larger sizes in L_x and look at long wavelength behaviour. Second, we can examine the behaviour of physical systems which are studied experimentally; it is common that dendritic growth experiments in succinonitrile are conducted using an undercooled melt held between plates of glass (Chou and Cummins 1988; Qian and Cummins 1990).

Finally, we can examine the transition from 2D to 3D behaviour by varying L_y between 1 (2D) and L_x (3D). This is helpful in extending results from 2D simulations to 3D and understanding the importance of an additional degree of freedom. In Chapter 6, we employ a 2D system in order to examine the linear stability of the Mullins-Sekerka instability at very large wavelengths on long timescales; this is currently not possible in 3D systems due to hardware constraints.

Bulk Inclusions

Using an $L_x = L_y = L_z$ lattice and the normal nearest-neighbour scheme, the interface is initialized as the boundary between a cubical inclusion of size $\ell \times \ell \times \ell$ of one phase (ie. solid crystal) within a background of the other (ie. a liquid melt). Typically, the initial size of the inclusion is $\ell = 0.75\ L$, the system size; this is just over half of all the spin sites. This configuration is used to study a droplet interface while in equilibrium (see Section 5.2) and also as it evaporates from an initially cubic shape to nothing (see Section 5.3).

It is this system which employs boundary cooling/heating on all six sides; it is important to properly simulate contact with a heat bath on all side of the droplet so that no artificial asymmetries are introduced. Although periodic boundary conditions are still maintained on four of the six sides, the solid droplet never makes contact with edges of the system.

Two-dimensional Systems

We also employ a two-dimensional version of this code for special use in the study of linear stability analysis presented in Chapter 3. The essential details of the model do not change significantly except for the case of the long-range interaction used in Section 6.1. In this case an extended range for the site-site interaction is used. Details are presented in that Section. The reasons for the 2D approach are related to the limit of resolution currently possible in three dimensions.

5 Equilibrium and Near-Equilibrium Interfaces: The Roughening Transition in Three Dimensions

As a first step toward characterizing the simple cubic crystal interface, we shall examine its equilibrium behaviour. Of particular import is the roughening transition behaviour as it was described in Chapter 2. By analysing the two structural *phases*, faceted and roughened, of an interface, we will be able to better define the behaviour of the transition both in terms of a planar interface and the surface of a bulk inclusion. In Section 5.1, we explore the equilibrium behaviour on a planar $\{100\}$ interface, both near and away from the transition temperature T_R. Then, in Section 5.2, we extend the description to a bulk inclusion or droplet interface, noting how the transition behaviour is modified by a stabilizing external field. Removing the external field so that the droplet interface is at coexistence, we study the phenomenon of a slowly evaporating droplet in Section 5.3; this is viewed as a *near-equilibrium* state which demonstrates a transition-like behaviour that is unrelated to the equilibrium or dynamic roughening transition. In Section 5.4, we examine another near-equilibrium state wherein a planar interface is subjected to a small driving force. We observe how the external field again results in a *dynamic* roughening transition.

5.1 The Planar Interface at Equilibrium

From the basic theory presented in Section 2.1, we know that the roughening transition of the $\{100\}$ interface of the 3D Ising model is an infinite-order Kosterlitz-Thouless transition with a characteristic temperature dependence of the step free energy, step-step correlation length and interface width. The behaviour of the interface above and below the transition is not as well-known. In this section, we introduce expressions for several useful quantities based on the surface fluctuations of the simple cubic crystal interface; they will help us to define its behaviour at equilibrium and subsequently to identify the transition. We then examine the results from our simulations of a $\{100\}$ planar interface to confirm their consistency with the well-known transition behaviour and to compare them with our new expressions away from the transition region. For reference, the transition temperature of the 3D Ising model has been identified analytically (Adler 1987; Holzer and Wortis 1989) as

$$T_R/T_c \simeq 0.546 \pm 0.004$$

and by computer simulation (Mon, Landau and Stauffer 1990) as

$$T_R/T_c \simeq 0.542 \pm 0.002.$$

Theory

Equilibrium interfaces, both physical and virtual, reflect the presence of thermal energy in the form of fluctuations in surface geometry which can be described in terms of a fluctuation probability density P_f. Analysis of this distribution provides a more reliable measure of the roughening transition, with better statistics, than other approaches in the literature. We define it in terms of a faceted reference plane, upon which there is a collection of *micro-facets* which reflect the stochastic balance between the available thermal energy and the free energy cost of forming a facet step. A micro-facet is a small *island* on the interface which is one lattice constant higher (or lower) than the reference plane and has a characteristic size ℓ; it is equivalent to a nucleation site in a 2D system. At a given temperature T, the distribution of micro-facet sizes is Boltzmann-like

$$P_f(\ell, T) = \Omega \; e^{-E_f(\ell)/T};$$

$E_f(\ell)$ is the free energy of a facet of size ℓ , given by

$$E_f(\ell) = 4\ell E_s(T) - a\ell^2 \triangle E_b(T)$$

assuming the site is square to first approximation (ie. small and on a cubic lattice) and far from any other site. Here, $\triangle E_b$ is the bulk free energy difference and a is the lattice constant. If the interface is assumed to be at coexistence (ie. $\triangle E_b = 0$), the condition $\int_0^\infty P_f(\ell, T) d\ell \equiv 1$ defines the prefactor to be

$$\Omega = \frac{4E_s}{T}.$$

The distribution $P_f(\ell, T)$ then measures the relative probability of a given size of micro-facet appearing on an interface of infinite extent in the continuum limit.

The mean micro-facet area $\langle A \rangle$ is then

$$\begin{aligned} \langle A(T) \rangle &= \int_0^\infty \ell^2 \; P_f(\ell, T) d\ell \\ &= 2\frac{T}{4E_s}^2 . \end{aligned} \tag{99}$$

Thus as E_s goes to zero at T_R (5), the mean facet area diverges strongly to infinity. This behaviour was anticipated by Weeks and Gilmer (Weeks and Gilmer 1979) from a visual inspection of Monte Carlo simulations of a flat interface.

Similarly, the variance σ^2, which measures the dispersion of the micro-facet area around $\langle A \rangle$, is

$$\begin{aligned} \sigma^2(T) &= \int_0^\infty (\ell^4 - \langle A \rangle^2) \; P_f(\ell, T) d\ell \\ &= 24\left(\frac{T}{4E_s}\right)^4 - 4\left(\frac{T}{4E_s}\right)^3 \qquad T < T_R. \end{aligned} \tag{100}$$

In the same regime, the interface width is proportional to total number of micro-facets which can be shown to be proportional to $\langle A \rangle$;

$$\begin{aligned}\langle w^2(T)\rangle &\propto \langle n(\ell)\ell^2\rangle^2\\ &\propto \langle A\rangle^2. \end{aligned} \qquad (101)$$

this can be shown to be consistent with (35) in the limit $T \to T_R^-$. The uncovered fraction A_o of the reference plane, which by definition, goes to zero as $T \to T_R^-$, becomes

$$A_o = 1 - C_{onst}\langle A\rangle \qquad (102)$$

where C is a constant which is model dependent.

As $T \to T_R^-$, micro-facets begin to overlap, corrections to equations (99), (100) and (102) for step-step interactions become important, and the simple micro-facet description would seem to be less useful. However, it can be used quite close to T_R, since the essential physics is captured by the abrupt manner in which E_s goes to zero. Indeed, near T_R, the description is consistent with the established relationship between the thermal correlation length and E_s as expressed by equations (3) and (5). To see this, we identify the mean facet size $\langle\ell\rangle$ as a measure of the correlation length, so that

$$\xi \propto \langle\ell\rangle = 1 + \frac{T}{4E_s}; \qquad (103)$$

note that in the thermodynamic limit of infinitesimal fluctuations (ie. using $\int_0^\infty$ instead of $\int_1^\infty$), we recover the form of the Fisher relation for the square Ising lattice (Fisher 1969), $\xi = T/\gamma_{2D}$ where the 2D surface energy corresponds to the step free energy, $\gamma_{2D} \sim E_s$. Since analytic results are available for the 3D Ising model (Holzer and Wortis 1989), this expression also provides a useful description of ξ when $T < T_R$.

Above T_R, the crystal surface is no longer faceted. However, the micro-facet distribution can still be defined via a geometric analysis, and the mean facet area $\langle A \rangle$ can be related to the mean curvature $\bar{\kappa}$, so that

$$\langle A \rangle \propto 1/\bar{\kappa} \propto T^{-1/2} \qquad T > T_R. \tag{104}$$

Details of this relation are given in Appendix A.3. We know (Grant 1988) that the width varies as

$$\langle w^2(L,T) \rangle \propto \frac{\ln(L)\, T}{\gamma(T)} \qquad T > T_R. \tag{105}$$

The factor T in this expression does not appear in (35) because, compared to $\sqrt{T - T_R}$, it is approximately constant near T_R.

Simulation

To examine the behaviour of an equilibrium planar interface of $\{100\}$ orientation at coexistence, the coexistence temperature was varied over $T \equiv T_m \in [0.2, 0.8]\ T_c$ through the external field via (93); the spin degeneracy was maintained at $\delta = 2$ for all runs. During the simulation, the interface was permitted to fully relax, requiring approximately 1000 MCS. The statistics were based on the final state of one to six runs, depending upon the proximity of T_m to T_R and upon lattice size L; larger systems required only one run to provide useful statistics. Lattice sizes were varied, $L \in [32, 512]$, with the system height held at a constant $L_z = 24$; this was sufficient to permit the largest systems at the highest T to relax to a fully roughened state without encountering the upper and lower boundaries. Figure 18 shows a series of equilibrium planar interfaces at temperatures above and below T_R.

In order to make contact with previous studies (Mon, Landau and Stauffer 1990) and the analytic predictions (35), (105) and (101), the width of the interface $\langle w(T)^2 \rangle$ was measured. This is defined as the mean square width of a single-valued surface

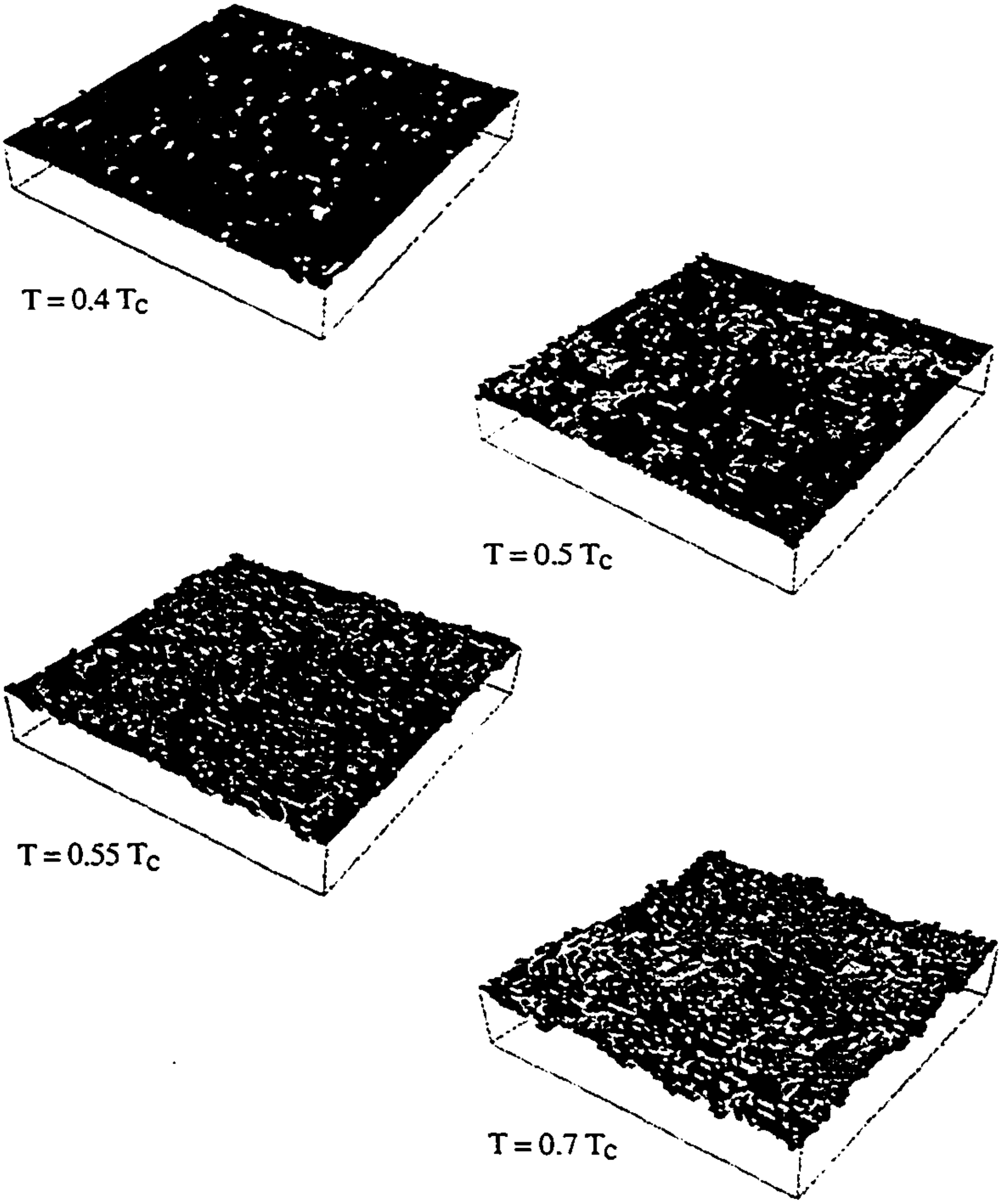

Figure 18: A series of equilibrium planar interfaces at temperatures around the 3D Ising roughening transition temperature $T_R \approx 0.54\ T_c$; the images shown are based on a $64 \times 64 \times 24$ system at $T = 0.4, 0.5, 0.55$ and $0.7\ T_c$. The lighter color indicates higher surface level. Systems up to $512 \times 512 \times 24$ were used in this study.

which is derived from the actual interface by eliminating all overhangs and bulk fluctuations. At most temperatures of interest, this is a very good approximation. Figure 19 shows $\langle w^2 \rangle$ for various L over a range of T: Away from $T_R \simeq 0.545\ T_c$ (Holzer and Wortis 1989), the data follows both (101) and (105) in a credible manner, and near T_R is consistent with (35) (see inset) although too sparse to confirm them in detail. The data is similar to that of a recent study by Mon, Landau and Stauffer (1990) for systems of comparable size, in that finite size effects are not very pronounced. From the position and sharpness of the cusp in the data, the roughening transition is estimated to be $T_R/T_c \simeq 0.54 \pm 0.01$; this can be improved by producing more data points with better statistics near the critical region, using the critical expressions for the width for analysis as did Mon *et al.*

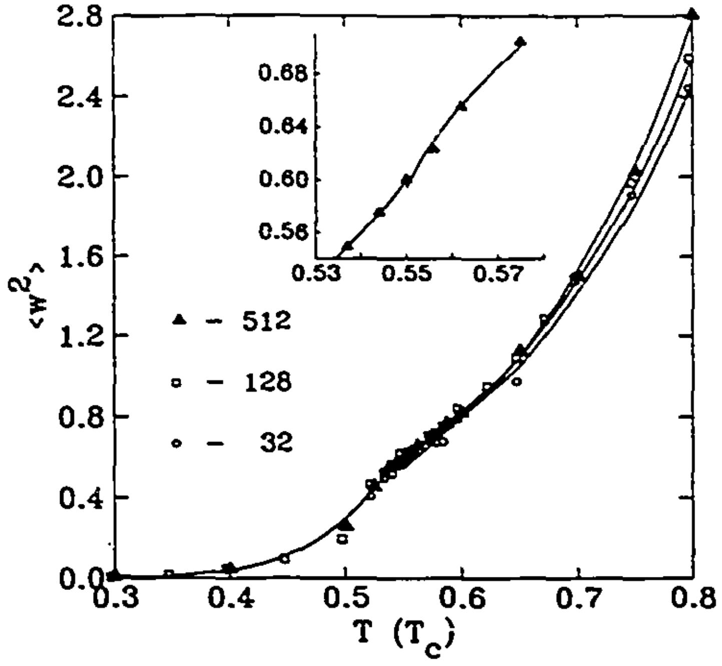

Figure 19: The mean squared width of the equilibrium planar interface at $T \in [0.2, 0.8]\,T_c$ for system size $L = 32, 128$ and 512. The 3D Ising roughening transition is at $T_R \approx 0.54\ T_c$. The solid lines are fits to analytic expressions (101) and (105); note the finite size dependence of the data above T_R. The inset shows the data near to T_R with fits for the critical expression (35).

However, the analysis of the facet-size distribution displays the transition much more clearly using the same data. Figures 20 and 21 show $\langle A\rangle$ and σ^2. Their

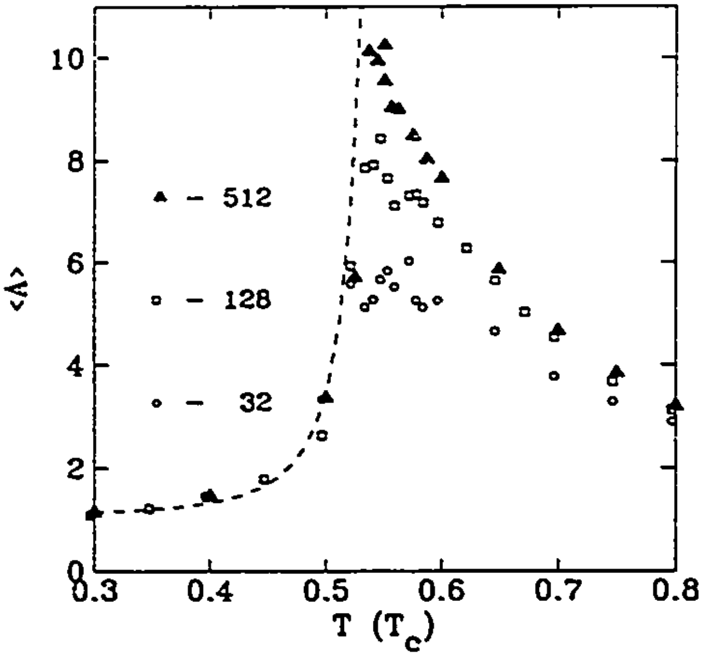

Figure 20: The mean micro-facet area for the equilibrium planar interface at $T \in [0.3, 0.8]\, T_c$ for system size $L = 32, 128$ and 512. The dashed line is a fit to the analytic expression (99).

behaviour is divergent near T_R and shows a distinct finite size scaling at and above the transition, with σ^2 most clearly indicating the transition. Examining the divergence in the data, the transition temperature is estimated to be $T_R/T_c \simeq 0.542 \pm 0.005$. Using the modified expressions for (99) and (100) (see Appendix A.4) which have been corrected for a minimum micro-facet size of unity, we find that they are in good agreement with the data, using the temperature as the fitting parameter and the low-T expansion for $E_s(T)$ of the 3D Ising model from Holzer *et al* (Holzer and Wortis 1989). Above T_R, $\langle A(T)\rangle$ is expected to follow $T^{-\frac{1}{2}}$ (104); our results are consistent with this prediction although the power law is too weak to fit unambiguously to the limited range of data.

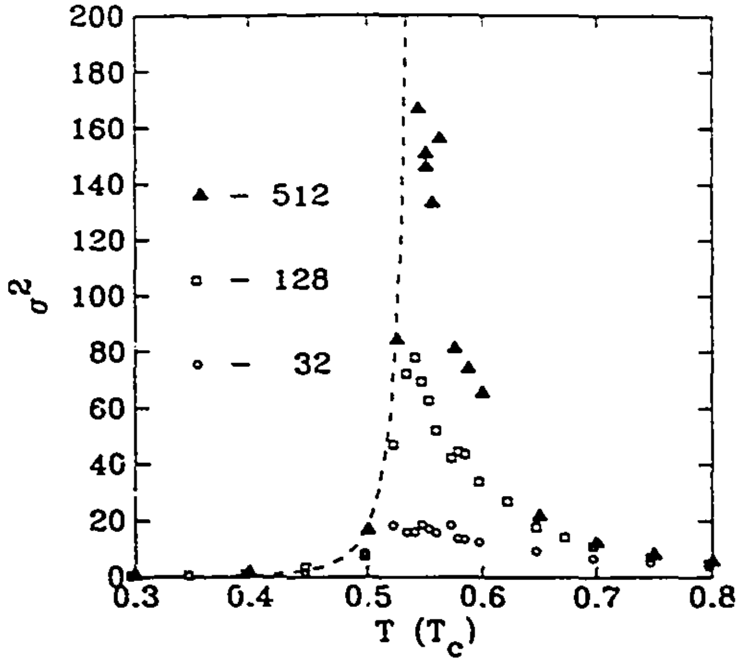

Figure 21: The variance in the mean micro-facet area for the equilibrium planar interface at $T \in [0.3, 0.8]\,T_c$ for system size $L = 32, 128$ and 512. The dashed line is a fit to the analytic expression (100).

In Figure 22 we show the fractional area of the reference plane A_o; note the finite-size behaviour at $T < T_R$. Although, we have not been able to provide a satisfactory argument for a scaling ansatz, we point out that this behaviour is consistent with the observation that E_s scales like $1/L$ by Mon *et al.* (1988). The data displays a clear point of inflection near the anticipated T_R; from this, we estimate $T_R/T_c \simeq 0.542 \pm 0.008$. The data for the largest system ($L = 512$) agrees well with corrected version of (102) (see Appendix A.4), again using the expansion expression for $E_s(T)$ and fitting the temperature and C as parameters.

Results

The characterization of a planar $\{100\}$ crystal interface has been extended from the critical behaviour at the roughening transition temperature T_R to $T \ll T_R$. The

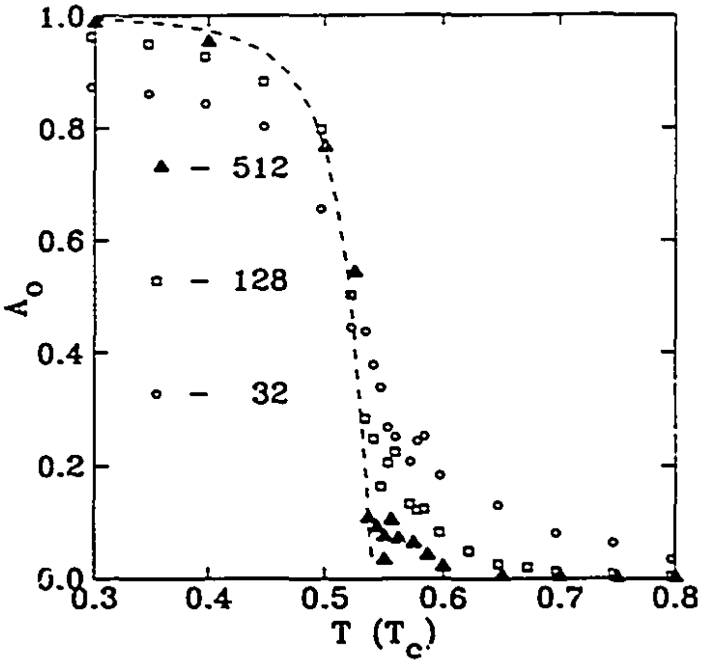

Figure 22: The normalized area of the reference plane which is not obscured by micro-facets for an equilibrium planar interface at $T \in [0.3, 0.8]\ T_c$ for system size $L = 32, 128$ and 512. The dashed line is a fit to the analytic expression (102).

micro-facet population on the interface can be described in terms of the mean micro-facet area $\langle A \rangle$ and its variance σ^2, both of which diverge at T_R. The mean square width of a faceted interface has been shown to be proportional to $\langle A \rangle^2$ below T_R. The fraction of the exposed reference plane is related to $\langle A \rangle$; we expect these quantities to show finite-size effects. All of these quantities, including the critical expressions, have been shown to be in good agreement with simulation. As well, a relationship between the step-step correlation function and the step free energy has been suggested, based upon the micro-facet distribution. It is consistent with critical theory.

Simulation results have been compared favourably with established expressions for $\langle w^2 \rangle$ near and above T_R. A geometric argument subsequently provides a measure of $\langle A \rangle$ above T_R which is consistent with simulation.

5.2 The Metastable Droplet at Equilibrium

When the solid-liquid interface bounds a finite droplet instead of an infinite plane, all possible surface orientations are present. Below the roughening transition, the faceted {100} reference plane manifests itself as six *macro-facets* with {100} orientation on a roughly cubical form. The macro-facets are macroscopic, flat, circular regions on each of the faces, joined by curved, roughened surfaces. As described in Section 2.2, they are an intrinsic part of the equilibrium crystal shape, decreasing in size and finally disappearing as the temperature approaches T_R. However, equilibrium transition behaviour is not strictly observable on a static, finite droplet. At coexistence a finite droplet is not stable; the system tends to minimize the energy contribution of the interface by reducing the surface area and evaporating the droplet away. A counter-force is required to balance the surface tension and provide a metastable interface. The equilibrium roughening transition is modified by the presence of this force. Using the techniques outlined in the previous section, we demonstrate the effect of a force on a static interface and compare the results with predictions made by Nozières *et al.* (1987).

Theory

Consider the free energy of a spherical droplet of radius R;

$$E_F = 4\pi R^2\gamma - \frac{4}{3}\pi R^3 \triangle E_b$$

where $\triangle E_b$ is the bulk free energy difference and γ is the surface energy. There is a metastable point where $dE_F/dR = 0$ at the critical radius

$$R^* = \frac{2\gamma}{\triangle E_b}.$$

When $R > R^*$, the droplet will tend to grow; and when $R < R^*$, the droplet will tend to shrink. At coexistence, when $\triangle E_b \equiv 0$, R^* becomes infinite, and all sizes of droplet will shrink. In order to study the roughening transition of a finite droplet at equilibrium, there must be a finite bulk free energy difference $\triangle E_b$. There will only be a static interface in the presence of a driving force or *over-pressure*, $F \propto \triangle E_b$. The effect of this force on the roughening transition is that the T_R^* of the finite droplet interface is depressed below the transition temperature of the planar interface; as well, the transition behaviour is spread over a greater range of T. Neither curvature nor finite size effects can be suggested as the origin of this behaviour; they may influence the scaling of the critical behaviour but not the critical temperature itself.

For a static, faceted interface at temperature T, Nozières and Gallet (1987) predict that a characteristic force F^* is required to shift the roughening transition to $T_R^* < T_R$ such that the interface *appears to be rough*;

$$F^*(T_R^*) = \gamma a/\xi^2 = E_s^2 a^3/\gamma \tag{106}$$

where $\xi(T)$ is the step correlation length and a is the lattice constant. This expression can be compared to our data using values from analytic sources (Holzer and Wortis 1989) for E_s and γ.

Visual inspection of the equilibrium crystal shape (ECS) shows a distinct dependence on T (see Figure 23). The droplet is exactly cubic at $T = 0$; the corners become rounded as T increases; the faceted faces of the cube are circular and shrink as T approaches T_R; the macro-facets disappear completely at T_R, leaving only a roughened surface. Finally, as T approaches T_c and the surface tension becomes isotropic, the cuboid becomes spherical. It has been noted that the surface of a finite crystal can be mapped onto a two-phase system (Nozières 1989), with the curved, roughened portions of the surface representing one phase and the flat, faceted regions representing the other. The edges of the macro-facets below T_R are then phase boundaries and their size and shape correspond to the equilibrium crystal shape of a 2D droplet; this shape has been well-defined theoretically for the nearest-neighbour 2D Ising model (Rottman and Wortis 1981; Holzer 1990a). The radius of the approximately circular face has been analytically defined through perturbative expansion as a function of T (Holzer 1990a); the inset in Figure 24 shows the analytic normalized facet radius $r_f(T)$ as a function of temperature for directions parallel and diagonal to the Cartesian axes.

Simulation

To study the meta-stable droplets, we choose to look at an $L \times L \times L$ system with a droplet of size $\ell \times \ell \times \ell$ where $\ell = 0.75L$. The system parameters are chosen to satisfy metastability (ie. $R \approx R^*$), and the over-pressure required to maintain metastability, F^*, is provided by a bulk free energy difference resulting from setting T_m slightly higher than the ambient simulation temperature T. No exact prediction for F^* is available for a non-spherical droplet; consequently, the parameters are chosen empirically such that the droplet is metastable after quickly relaxing from a $T = 0$ cube to local equilibrium. If the droplet were not metastable, it would then begin to decay or grow. Above T_R, the metastable parameters are unique to within the amplitude of thermal fluctuations. Below T_R, the choice is complicated by exceedingly long time scales for the evaporation of an unstable, faceted interface; this is discussed in greater detail in Section 5.3. The consequence is that our results well below T_R may be only *near* equilibrium. On the other hand, the results nearest to T_R are very precise and the correct transition behaviour is preserved.

The droplet was initialized as a cube (ECS for $T = 0$) and allowed to relax to equilibrium for 5000 to 30000 Monte Carlo steps. The trial temperatures ranged from $T \in [0.2, 0.8]\ T_c$ for system sizes $L \in [32, 128]$. The largest contiguous facet on each of the six faces of the cube is identified with the anticipated macro-facet. The

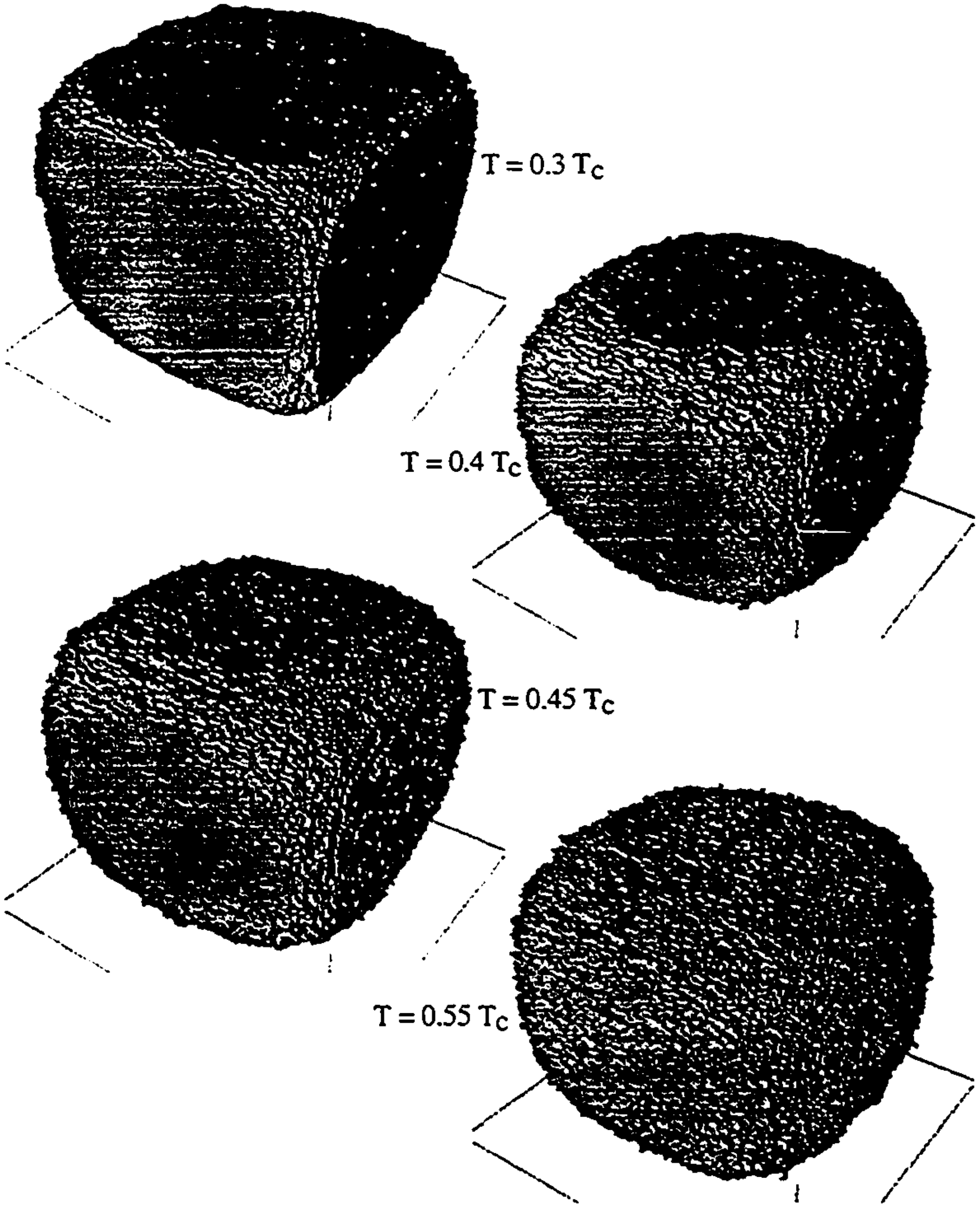

Figure 23: A series of equilibrium droplet interfaces at temperatures around the modified roughening transition temperature $T_R^* \approx 0.46\,T_c$; the images are based on 128^3 system with a 96^3 bulk inclusion at $T = 0.3, 0.4, 0.45$ and $0.55\,T_c$. Note that these droplets are only metastable and in the presence of a stabilizing *over-pressure*.

macro-facet radius r_f is based on the average area of the six largest facets $\bar{A}_f$ and the assumption that they are approximately circular (ie. $\pi r_f^2 \equiv \bar{A}_f$). In addition, the micro-facet size distribution for the entire surface is analysed in a manner similar to the planar interface. (To make an exact comparison to the planar case, it would be necessary to isolate the micro-facets on the macro-facets only. We judge the additional computational complexity not to be worthwhile.) Similarly, due to the inherent difficulty in defining the local width of a non-planar surface, $\langle w^2 \rangle$ is not measured. Figure 23 shows a series of metastable droplets above and below the effective roughening temperature T_R^*.

The macro-facet area was taken from the average of the largest contiguous facets on each of the six faces of the droplet. Assuming the macro-facet shape to be circular, Figure 24 shows the average macro-facet radius as a function of temperature; it has been normalized to the droplet radius, defined to be from the droplet center to the {100} face. The transition point is less apparent than in the planar case; this is consistent with the predicted blurring of the roughening transition. If the inflection point is taken to be the transition point, T_R^* would be well below the equilibrium T_R, as expected. Alone this information is not very useful. However, it is more or less consistent with the expected form of $r_f(T)$ (see inset of Figure 24).

The variance σ^2 shows the transition much more clearly as seen in Figure 25; $\langle A \rangle$, shown for L=128 as an inset, is not a useful quantity at least with the limited statistics provided by our simulations. However σ^2 indicates the transition distinctly at $T_R^*(\mathrm{L}=128)/T_c = 0.450 \pm 0.008$, well below the equilibrium transition temperature $T_R(\infty) \simeq 0.545\ T_c$. A weak dependence on L is discernible in both the strength of the divergence and the shift in T_R, consistent with the increase in the necessary over-pressure with decreasing system size.

Ideally the over-pressure should be varied through a range of values for a single

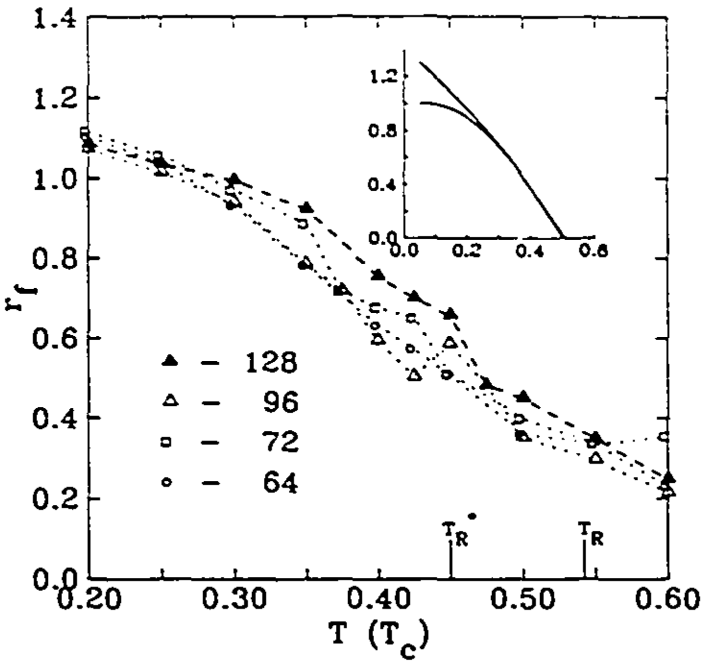

Figure 24: The average macro-facet radius r_f for the metastable droplet at $T \in [0.3, 0.6]\ T_c$ for system size $L = 64, 72, 96$ and 128; the effective roughening temperature T_R^* is indicated, derived from other quantities. The inset shows the analytic prediction for r_f for an infinite droplet; the two lines are for r_f parallel and diagonal to the lattice axes.

trial temperature T in order to identify the critical $F^*(T)$ required to induce roughening. Figure 26 shows the phase diagram of droplet interface; the solid and dashed lines indicate the critical $F^*(T)$ and the droplet metastability respectively; the vertical line of points indicates a hypothetical series of over-pressures that should be tested to identify the critical roughening force at a constant temperature T_{test}. However, only one value of $F^*(T)$ is accessible for each system size L; specifically, for the set of parameters for which the system is approximately at the modified roughening transition. For the L=128 system shown in Figure 23, this is at $T_R^* \simeq 0.450\ T_c$. We can now check the prediction by examining Figure 27: The data points are the empirically chosen over-pressures (controlled by varying the undercooling of the liquid phase) for two system sizes (L=128 and 64) required for metastability. The solid line is the

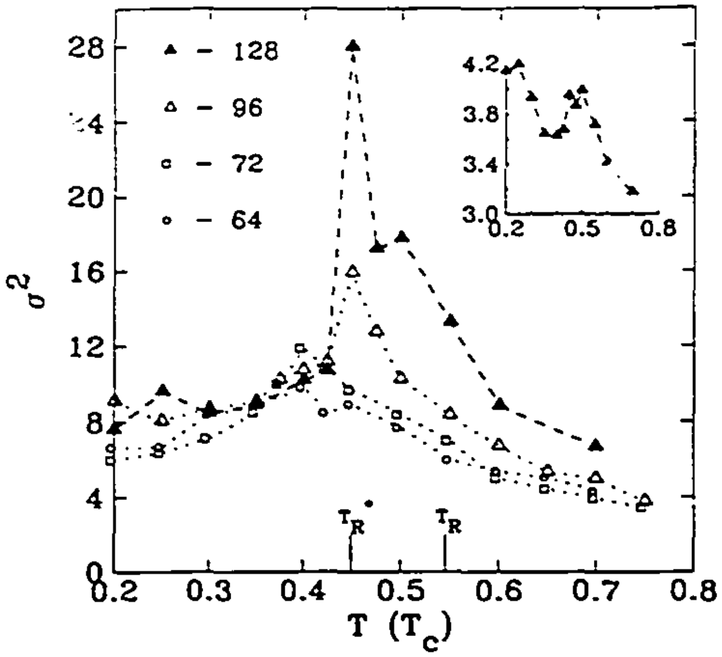

Figure 25: The variance in the mean micro-facet area for the metastable droplet at $T \in [0.3, 0.75]\,T_c$ for system size $L = 64, 72, 96$ and 128. The inset shows the mean micro-facet area for $L = 128$; this quantity was less reliable in the determination of the roughening transition. Note the shift in the peak with system size.

analytic prediction for $F^*(T)$ according to (106); it is the over-pressure required to roughen a static surface at temperature $T < T_R$. The point of intersection indicates the trial temperature at which we expect to see the roughening transition in our data: it is in good agreement. It also indicates a shift in F^* related to system size which is consistent with our observations.

Results

We have shown the system size dependence of the balancing force required to satisfy metastability on a finite droplet. We have also shown the presence of a roughening transition behaviour on the metastable crystal droplet both visually and in terms of the quantities $\langle A \rangle$ and σ^2. The predicted temperature dependence of the macro-facet

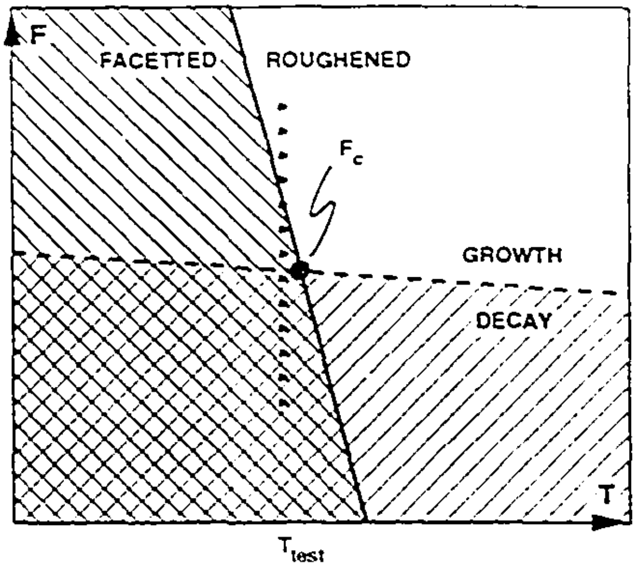

Figure 26: A rough representation of the droplet interface phase diagram at some range of temperatures below T_m; it shows the line of critical over-pressures separating the faceted and roughened states as well as the line of metastability for a droplet of a given size. The point of intersection is the overpressure where the metastable droplet becomes rough. The vertical line of points represents a desirable set of measured values needed to test for the presence of the critical over-pressure boundary.

radii has been demonstrated albeit with some difficulty due to finite-size effects. Most importantly, renormalization predictions for the depression of the transition temperature are in good agreement with simulation; the expected system size dependence of T_R^* is also weakly observed.

5.3 An Evaporating Droplet

Away from metastability, the droplet described in Section 5.2 will tend to grow or shrink due to the imbalance between the over-pressure and the surface tension. Since a growing droplet may be morphologically unstable, we restrict our attention to the context of shrinking droplets. For example, if the droplet is at coexistence, there is no balancing force at all and the droplet shrinks due to the surface tension effects [1].

---

[1] The evaporation of a droplet at phase coexistence assumes that the system is maintained at constant temperature via contact with a heat bath. Otherwise, a closed finite system undercools as the evaporation takes place until it reachs a metastable state.

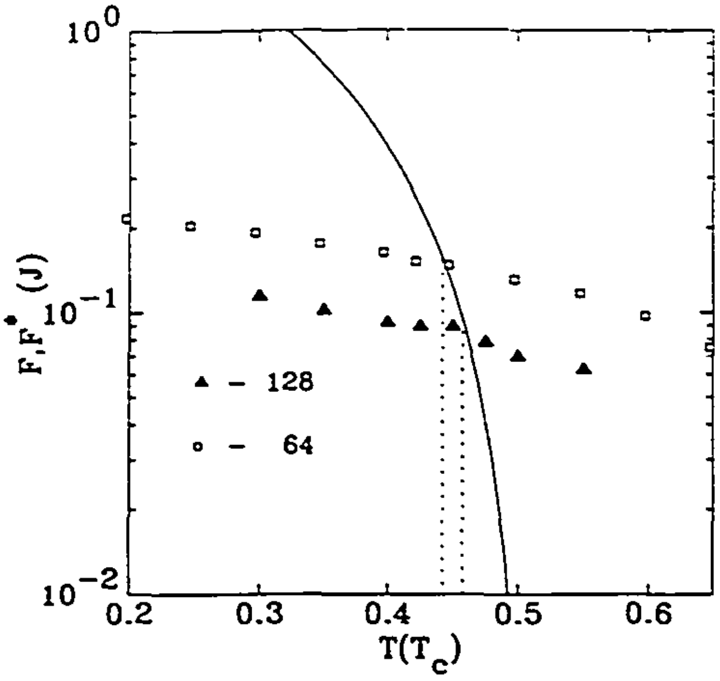

Figure 27: A comparison of the empirically chosen over-pressures required to satisfy metastability at $T \in [0.2, 0.65]$ T_c for system size $L = 64$ and 128 to the analytic prediction (solid line) made by Nozières and Gallet, (106). The point of intersection indicates where the effective roughening transition should appear. This is consistent with our observations.

It might be expected that the interface would move via a nucleation-limited process when it is at a temperature $T < T_R$; this is the case described in Section 5.4. However, we observe that the droplet is *forced* through a structural transition to permit the droplet to evaporate more quickly via a diffusion-limited process; we propose a description for this and a prediction for the time dependence of the macro-facet radii and the droplet radius.

Theory

A droplet at coexistence, $T < T_R$ such that it would be faceted in the metastable state, is constituted of both faceted and roughened regions, each evaporating at disparate rates. As the roughened portions quickly evaporate, the curvature along the edges of the faceted regions becomes more pronounced: in the language of a curved planar two-phase system, the phase boundary energy between the curved and planar phases increases. Figure 28 schematically represents this effect. Consequently, the system

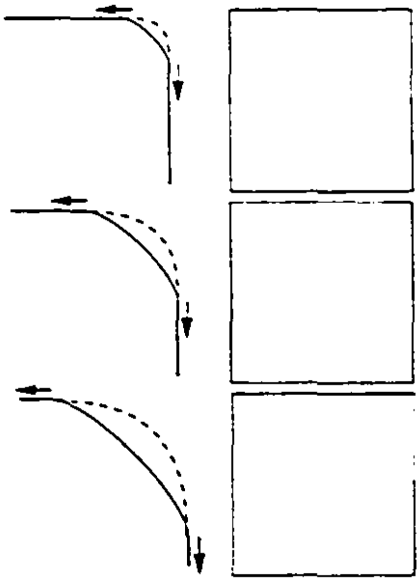

Figure 28: A rough diagram depicting the forced roughening transition on an unstable cube. The corners are rounded due to thermodynamic considerations. The roughened corners then evaporate much faster than the faceted surfaces. The increased curvature at the rough/smooth boundary reduces the size of the faceted region. Eventually, the facets disappear completely and the roughened cuboid continues to evaporate evenly.

will try to further minimize its surface energy by reducing the size of the macrofacets. Far away from metastability, the faceted phase will be forced out of existence and the surface will assume a completely roughened state, *not due to the kinetic effects of the moving planar interface* but rather due to rapid evaporation of the adjoining roughened regions. If the droplet is close to metastability, the facets will only shrink slightly, reaching a nucleation-limited evaporation regime where the faces remain faceted; for time-scales which are much shorter than the activation time of the nucleated evaporation, the droplet behaves like the static droplet described in Section 5.2.

These two evaporation mechanisms have characteristic dynamical time dependences. In the diffusion-limited regime, as the solid gives way to the liquid and latent heat of transition $\mathcal{L}$ is absorbed to form the liquid, heat must be transported from infinity to the interface. This is controlled by the diffusion constant D. Solving for the diffusion equation in radial coordinates for a sphere of radius R (Langer 1980), the growth rate is shown to be

$$\frac{dR}{dt} = \frac{D}{R}(\Delta u - \frac{2d_o}{R}) \tag{107}$$

where $\Delta u \equiv (u_\infty - u)/u_\infty$ is the dimensionless undercooling from infinity, u is defined as

$$u \equiv \frac{T - T_m}{\mathcal{L}/c_p}$$

and d_o is the capillary length

$$d_o \equiv \gamma T_m c_p/\mathcal{L}^2.$$

Note that this solution implies the *quasi-static approximation* where the timescale for thermal relaxation is much shorter than that for the interface dynamics; the diffusion constant D was chosen to satisfy this constraint. The $dR/dt = 0$ limit defines the critical droplet radius $R_c = 2d_o/\Delta u$ so that we can rearrange (107), and integrate it in the limit of small undercooling (ie. the limit of $R_c \rightarrow \infty$), to give

$$R(t) = (R_o^3 - 6Dd_o t)^{\frac{1}{3}}. \tag{108}$$

By contrast, the behaviour of the macro-facets is controlled by edge tension acting on their boundaries with the adjoining roughened regions. This is analogous to the *decay* of a 2D nucleation site which is smaller than the critical size, $r_f < r_f^*$. If it is assumed that the adjoining regions are near local equilibrium (ie. the time scale for their evaporation is much shorter than for the macro-facet dynamics), then we expect that the facets will shrink according to the Becker-Döring relation (Becker and Döring 1935); the volume of a droplet should decay at a rate proportional to its area,

$dV/dt \propto A$. For a near-circular 2D facet, the rate of evaporation then goes as the facet circumference, and we thus expect that $r_f(t)$ is linear in t.

We can also approximate the behaviour of the quantity $R(t)$ while $r_f(t)$ is still large. Let's assume that the curved (roughened) regions can be approximated to first order by a surface of constant curvature and that they are restricted to the corners of the evaporating cube (see Figure 29). We can then define the rate of change of volume in terms of the macro-facet radius $r_f(t)$. If the initial cubic volume is L^3, the roughened surfaces are quadrants of spheres of radius $R' \equiv L - r_f$. The volume of the truncated cube is then

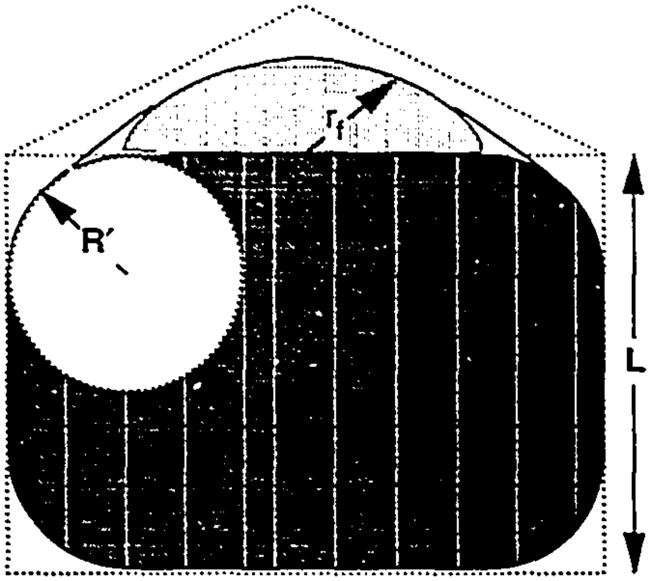

Figure 29: A schematic diagram depicting the evaporation of a cube; a partially faceted cube is shown in cross-section, cut diagonally through one of the faces. Only the corners are assumed to evaporate, maintaining a curved surface consistent with one quadrant of a sphere of radius $R' = L - r_f$.

$$V(t) = L^3 - (8 - 4\pi/3)(L - r_f)^3.$$

The droplet radius $R(t)$ shown in Figure 32 is defined in terms of the volume of a perfect sphere. Thus, the rate of change of volume is $dV/dt \propto dR^3/dt$; so if $r_f(t)$ is linear in t, we would expect $dR/dt \propto dr_f/dt \propto C_{onst}$.

To sum up, an evaporating, faceted droplet is expected to be limited by its facets, which shrink at a constant rate, until it becomes completely roughened. It will then be roughly spherical with a radius described by (108). It is expected that current experimental techniques should be able to observe this behaviour on faceted crystals away from metastability. Certainly, independent measurements have been made of nucleation- and diffusion-limited growth (Gallet, Balibar and Rolley 1987) and evaporation on planar and droplet crystal interfaces (Dougherty and Gollub 1988; Heyraud and Métois 1980; Métois and Heyraud 1982). In particular, the growth of crystals near equilibrium have been observed (Heyraud and Métois 1987); the crystals became strongly faceted with sharp edges. In contrast to the evaporation case, this appears as if the crystal is being forced into the completely faceted state. We present some of these experimental and simulation results in Appendix A.5.

Simulation

We ran several trials at the largest system size possible (L=128) to minimize finite size effects on the transition. The droplet was initialized as a cube of size $\ell = 0.75L$ at the ambient temperature, $T = 0.3\ T_c$, with the liquid background also at T. The coexistence temperature T_m was also set to 0.3 T_c so that the droplet completely evaporate (ie. $R_c = \infty$). Except for local cooling at the surface due to the absorption of latent heat, the system was maintained at constant T via contact with a heat bath at the boundaries. The latent heat and diffusion rate were chosen such that the trial ended with the complete evaporation of the solid within 5000 - 50000 MCS. The quantities r_f, $\langle A \rangle$, σ^2, and $\bar{m}$ (average system magnetization) were recorded; each gives a good indication of the transition of the cube surface from a faceted to a roughened state. Figure 30 shows a time series of the evolution of a typical evaporating droplet.

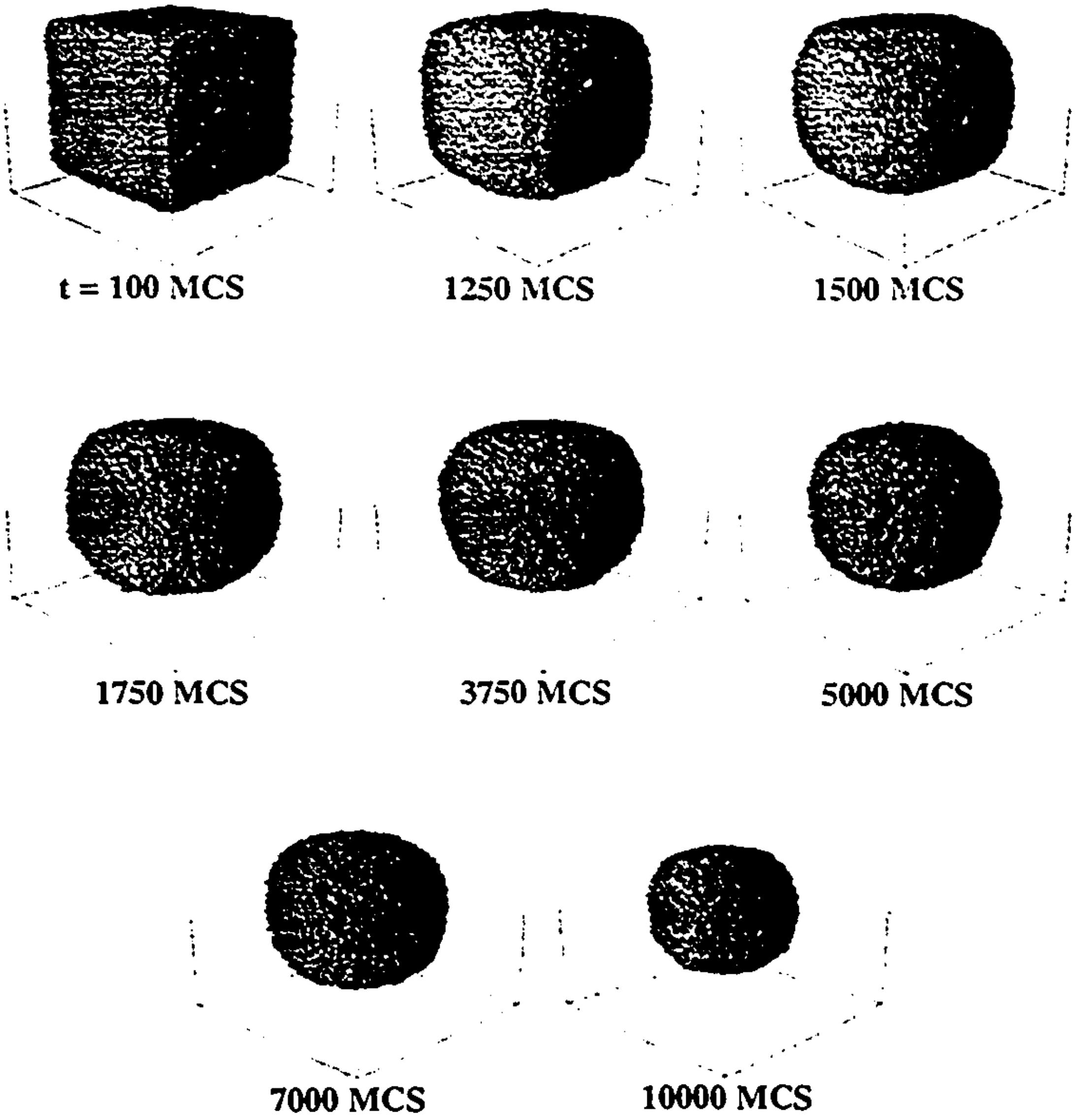
t = 100 MCS

1250 MCS

1500 MCS

1750 MCS

3750 MCS

5000 MCS

7000 MCS

10000 MCS

Figure 30: A time series of an unstable droplet as it evaporates from its initial cubic shape; the system is 128^3 with a 96^3 bulk inclusion at $T = 0.3\ T_c$. The transition from a faceted to completely roughened state occurs at approximately $t = 5000$ MCS. Note that even at $t = 10000$ MCS there is still a discernible facet on the cubes faces; this is inevitable as the Ising lattice is discrete and cannot otherwise represent a continuous curvature (see Figure 67).

Figure 31 shows the time-dependent facet radius, $r_f(t)$, for several runs with differing latent heat; the transition from the faceted to roughened state is marked by a distinct change in slope. This is confirmed by a visual inspection of the cube surface; the entire time series of cube images is observed in a continuous playback, similar to a movie, and the point at which the the macro-facets disappear is selected as the time of transition. Further, total surface energy $E_{tot}(t)$ and the moments of $P_f(t)$ have maxima at approximately the same transition point. Except for the first several hundred Monte Carlo steps before reaching local equilibrium, r_f is linear in t up to the transition point.

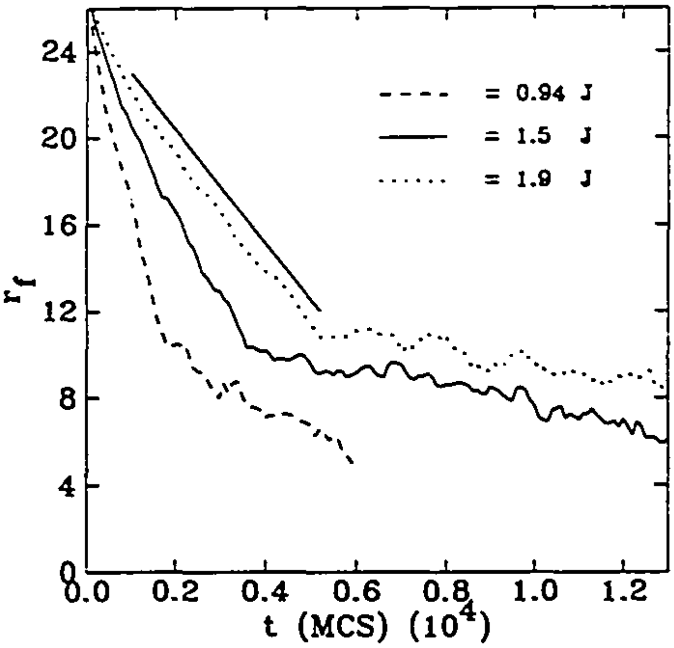

Figure 31: The average macro-facet radius as a function of time for unstable, evaporating droplets of system size $L = 128$ at $T = 0.3\ T_c$ for various latent heats. The radius is expected to decrease linearly in t until the droplet roughens; the solid line is to guide eye.

Figure 32 shows the time dependent droplet radius $R(t)$. The disappearance of the macro-facets is marked by a change in the behaviour of dR/dt. At early times, $R(t)$ appears to be linear in t, with droplet evaporation limited by the decay of the

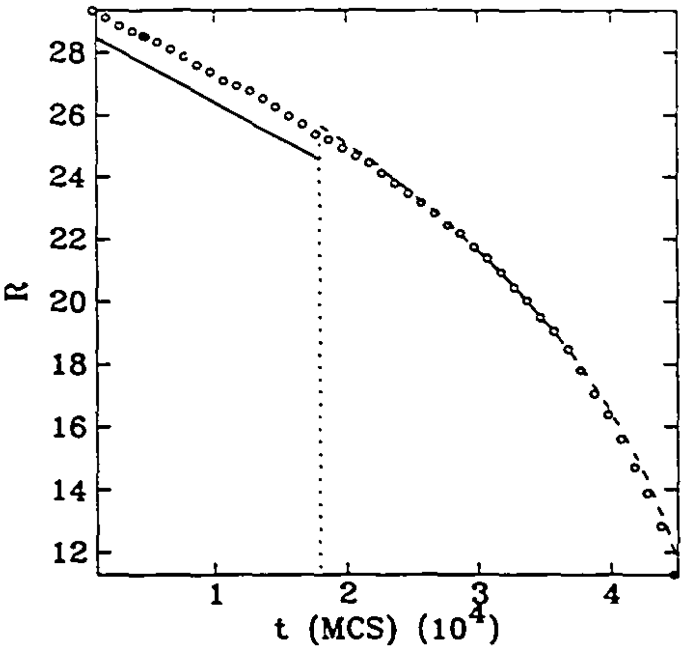

Figure 32: The droplet radius as a function of time for an unstable, evaporating droplets of system size $L = 128$ at $T = 0.3\ T_c$; the dotted line indicates the transition from a faceted to a roughened state. The dashed line is a fit to the analytic expression (76) for $R(t)$ of the fully roughened droplet. The radius appears to be linear in t while the droplet is faceted.

macro-facets. After the droplet is completely roughened, R(t) can be fitted by the expression (108) and as a by-product the capillary length d_o can be extracted for our choice of system parameters. We find $d_o \simeq 0.378 \pm 0.002$ in units of lattice spacing.

Results

Our simulation results are consistent with the proposed droplet evaporation mechanism, both with regard to the relaxation to a roughened state and the evaporation of the roughened droplet. We have used standard 2D and 3D nucleation language to describe the decay of the macro-facets and the droplet, respectively; the rate of decay of $r_f(t)$ and $R(t)$ is in good agreement with predictions. We also found a value for the capillary length from the fit for the diffusion-limited evaporation. It seems appropriate to describe the undriven evaporation of an initially faceted inclusion as *the decay of a 2D nucleation site imbedded in a decaying 3D nucleation site*, the 2D process acting as a limiting factor for the 3D process. This behaviour should be observable experimentally (see Appendix A.5).

5.4 The Weakly Driven Planar Interface

If a crystal interface is driven by an external force such that it has a steady-state behaviour and a constant velocity, it may exhibit a *dynamic* or *kinetic* roughening transition. We have chosen to examine a planar {100} interface with an undercooled melt; the bulk free energy difference between the *liquid* and *solid* phases provides a driving force which is limited by the diffusion of latent heat away from the interface. This case is representative of many crystal growth problems but is of particular interest to us because of the relevance to our studies of dendritic growth within the context of the Mullins-Sekerka instability (Harris, Jõrgenson and Grant 1992; Jõrgenson et al. 1993) (see Chapter 7). Theoretical predictions (Nozières and Gallet 1987) suggest that the dynamic roughening transition of the interface is broadened relative to the equilibrium behaviour and that the effective T_R^* is depressed as a function of the applied force. This is supported experimentally (Balibar, Gallet and Rolley 1990) and by other simulation studies (Grossman, Guo and Grant 1991). The interface is expected to have a highly non-linear response to a driving force while in a faceted state, compared to a nearly linear response when it roughens. This is due to the very different mechanisms responsible for the growth (Weeks and Gilmer 1979). Although we will not be able to quantify the effect of the driving force, we will characterize it in terms of the variables defined in previous sections.

Theory

At $T < T_R^*$ for a sufficiently small driving force, the interface moves via a nucleation process. Paraphrasing Nozières *et al* (Nozières and Gallet 1987), nucleation-limited growth is described in terms of micro-facets which spontaneously appear as thermal fluctuations on the faceted surface at a rate $I \propto e^{-E_f/T}$. The energy of formation is now

$$E_f(\rho) = 2\pi\rho E_s - a\pi\rho^2 \triangle E_b$$

for a circular micro-facet of radius ρ (ρ is expected to be larger than the lattice constant a); E_s and $\triangle E_b$ are the step free energy and bulk free energy difference respectively. The critical micro-facet radius (ie. for $\rho > \rho_c$, they grow; otherwise, they decay) is $\rho_c = E_s/\triangle E_b$. This introduces a timescale for the creation of growing micro-facets

$$1/\tau \propto e^{-E_f(\rho_c)/T}.$$

After time t, there will be on the order of t/τ micro-facets, each growing with a lateral velocity v_ρ which is approximately constant in time. Since the edges of the micro-facets are always rough (in 2D), the velocity is linearly dependent on the driving force (Weeks and Gilmer 1979). The separation between micro-facets is

$$\eta \sim \rho_c\sqrt{\tau/t};$$

thus, they will join to form a new reference plane when $\rho(=v_\rho t) \sim \eta$. This defines the forward velocity of the interface $v \equiv a/t$ as

$$v \propto \left(\frac{\triangle E_b^2}{E_s}\right)^{2/3} e^{-\pi E_s^2/3\triangle E_b T} \tag{109}$$

where a is the lattice spacing. The kinetic roughening transition occurs when the fluctuation correlation length is on the order of the critical micro-facet size, $\xi \sim \rho_c$; this condition is equivalent to the expression (106).

At $T > T_R^*$, the interface is roughened and growth is diffusion-limited. The growth velocity is expected to depend approximately linearly on the driving force $F \equiv \triangle E_b \simeq \triangle T$ and should vary only with T for constant F.

Simulation

Our data refers to a $\{100\}$ planar interface in a system of size $256 \times 256 \times 48$, initialized at $T = 0.5\ T_c$. The driving force F is supplied through the bulk free energy difference $\triangle E_b$ by varying the melting temperature T_m, and thus the *liquid* undercooling $\triangle T \equiv T_m - T$. The spin degeneracy is fixed at $\delta = 2.0$ and the ends of the system are maintained at T. Under these conditions, $\triangle E_b$ varies linearly with $\triangle T$. The *solid* is also initialized at T to minimize heating at the interface by allowing it to absorb some of the latent heat which is produced. The latent heat tends to heat both phases slightly but temperatures are always maintained well below the equilibrium roughening transition temperature T_R. The undercooling is varied with $\triangle T \in [0.01, 0.12]\ T_c$ and the simulations are run for 2000 to 10000 MCS until steady-state is reached; each data point is an average over one configuration (ie. no time-averaging). Figure 33 represents a series of driven planar interfaces at $T < T_R$.

Our first observation is that the experimental parameters such as A_o, $\langle A \rangle$ and σ^2 exhibit an oscillatory behaviour related to the activated growth mechanism; the period is $\tau = a/v$, where a is the lattice unit and v is the interface velocity. For example, Figure 34a shows A_o, the surface area of the reference plane, as a function of time for the slowest interface; A_o has a minimum when the growing micro-facets cover exactly half of the reference plane and a maximum when the current reference plane has just finished forming. The quantities based on the micro-facet distribution change in a similar manner; only a roughened plane will have a constant steady-state distribution. As the velocity of the interface increases with increasing driving force

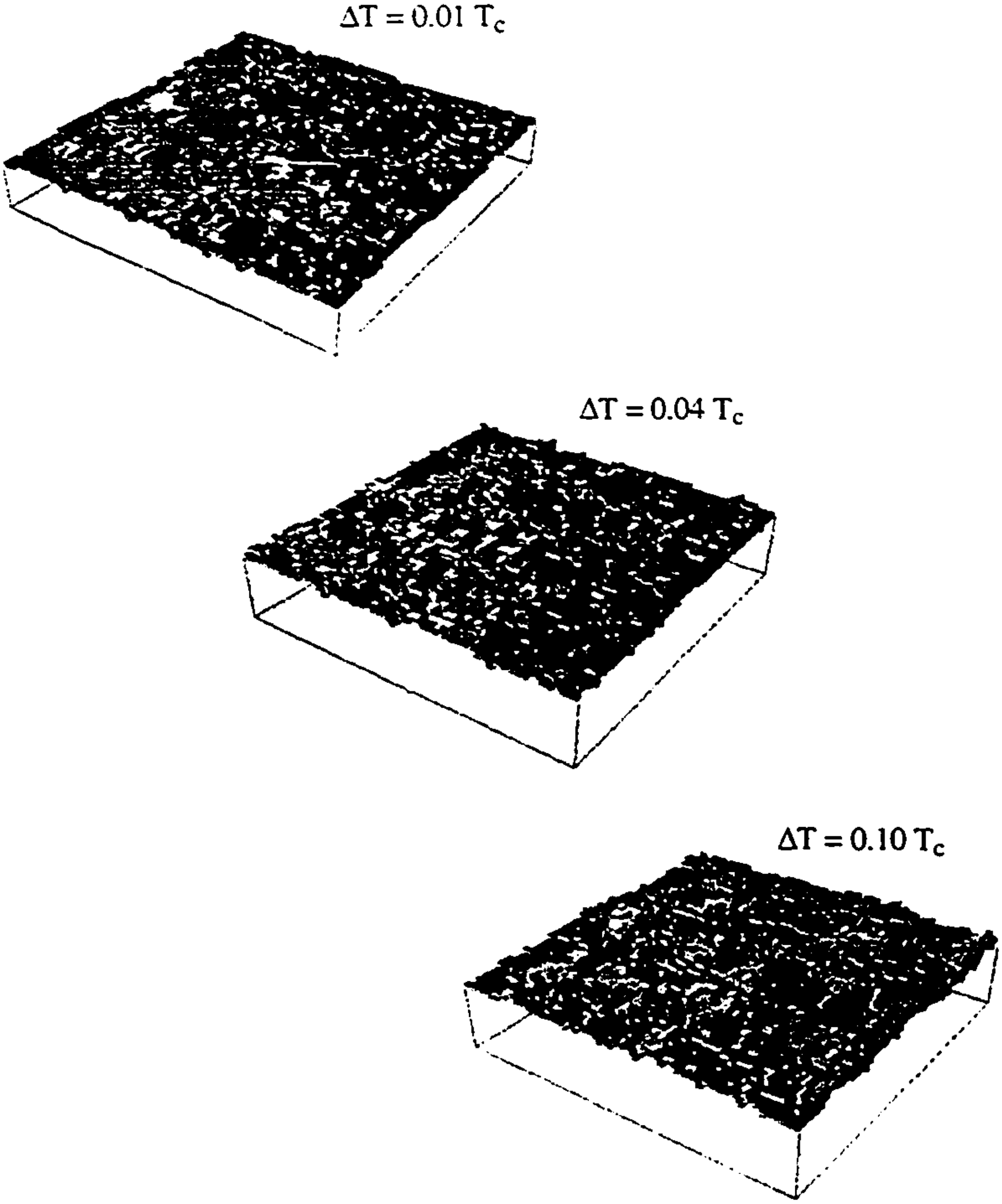

Figure 33: A series of driven planar interfaces at $T = 0.5\ T_c$; the images shown are based on a $64 \times 64 \times 48$ system with under-cooling of $\Delta T = 0.02, 0.04$ and $0.1\ T_c$. Systems up to $256 \times 256 \times 48$ were used in this study. The lighter color indicates higher surface level. Note that the equilibrium planar interface at $T = 0.5\ T_c$ in Figure 18 is the undriven equivalent of this interface.

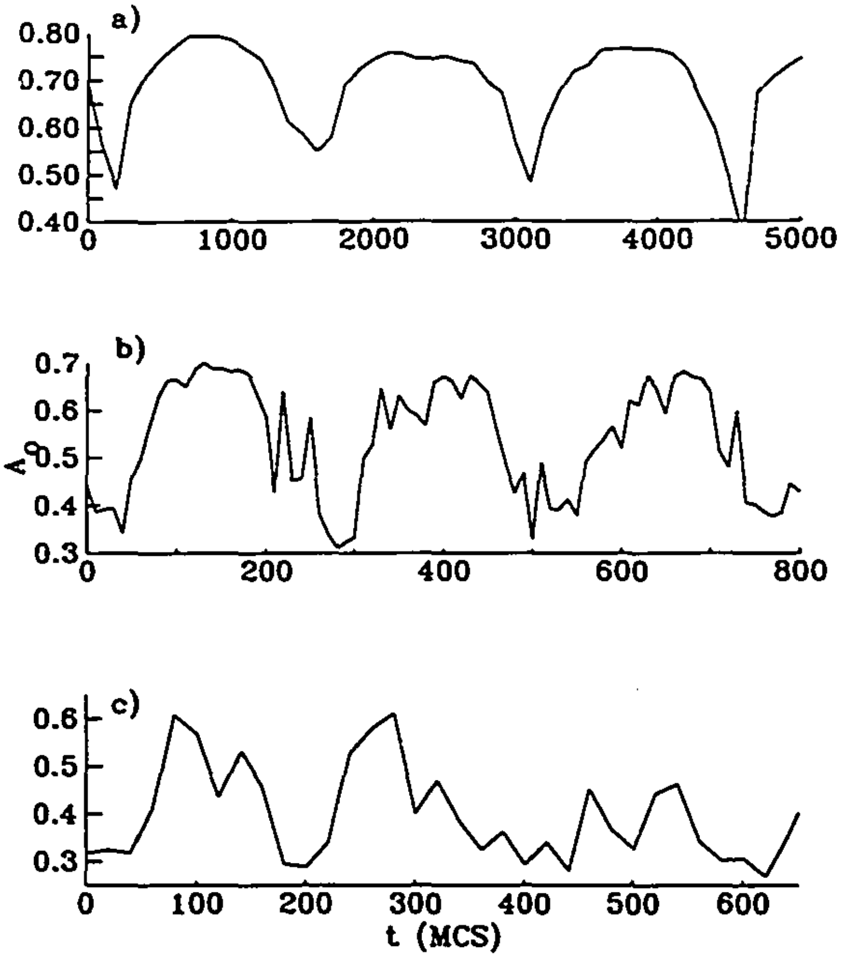

Figure 34: he normalized area of the reference plane which is not obscured by micro-facets for driven equilibrium planar interfaces at $T = 0.5\ T_c$ for under-coolings of $\Delta T = 0.02, 0.04$ and $0.10\ T_c$, from top to bottom; they are for interfaces which are below, at and above (respectively) the critical driving forces required to roughen the interface. Note that the time scales for each plot has been stretched for easy comparison.

$\triangle T$, the period of the cycle decreases as shown in Figures 34b and 34c.

Figure 35 shows the velocity of the interfaces as a function of $\triangle T$ (closed triangles); the data is non-linear and consistent with (109) up to $\triangle T \approx 0.04\ T_c$ where it then becomes linear. Also shown is the *reduced* velocity v/v_r (open circles). The reference velocity $v_r(\triangle T)$ is measured at a temperature above the equilibrium roughening temperature T_R where v_r is only dependent on the value of $\triangle T$. The reduced velocity clearly indicates that the effective dynamic transition is near $\triangle T^* \simeq 0.04\ T_c$.

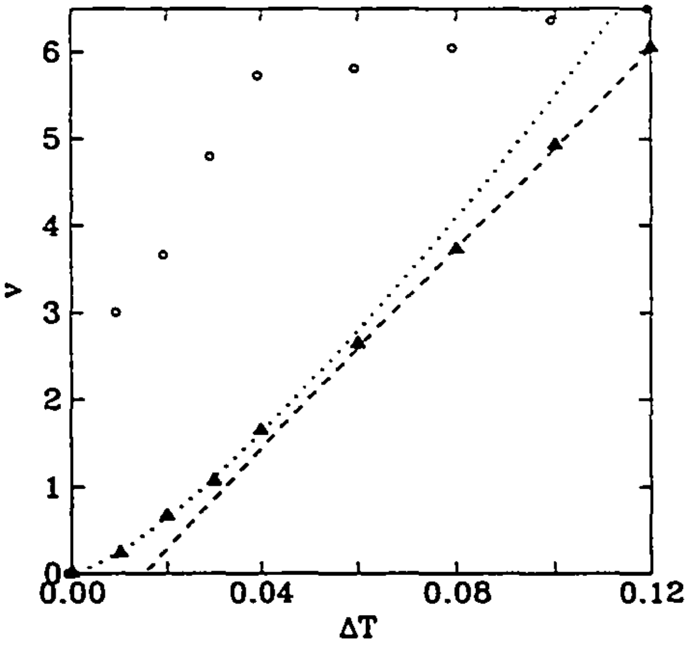

Figure 35: The average interface velocity (closed triangles) in units of lattice spacings per 1000 MCS for driven steady-state planar interfaces at $T = 0.5\ T_c$. The undercoolings are $\Delta T \in [0.02, 0.12]\ T_c$. Also shown is the *reduced* velocities $v/v_r(\Delta T)$ (open circles) where $v_r(\Delta T)$ is the velocity of a completely roughened interface under the same driving force. The dotted line is a best fit for the analytic expression for v, (109); the dashed line is a straight line. The critical driving force is estimated to be $\Delta T \approx 0.04\ T_c$.

Further evidence for this value comes from the character of the oscillations shown in Figure 34. As the dynamic roughening transition is approached, the smooth oscillations begin to break up. However, due to the broadened nature of the transition, oscillatory behaviour is still observed at and above ΔT^*. This is consistent with the description of dynamical roughening near T_R^* offered by van Saarloos et al (van Saarloos and Gilmer 1986) wherein the interface is expected to be rough at long length scales but nucleated growth is still pre-dominant at short length scales. Only near $\Delta T \simeq 0.12\ T_c$ does it appear that the interface has roughened at nearly all length scales.

The interface width $\langle w^2 \rangle$ does not exhibit any cyclic behaviour except at the very lowest undercooling. Despite the changing micro-facet distribution, $\langle w^2 \rangle$ is relatively smooth and relaxes to an average value once the thermal gradient reaches a steady state. Even in the case of $\Delta T = 0.01\ T_c$, the oscillatory behaviour eventually damps out and $\langle w^2 \rangle$ reaches a steady state value. Presumably this behaviour is a reflection of

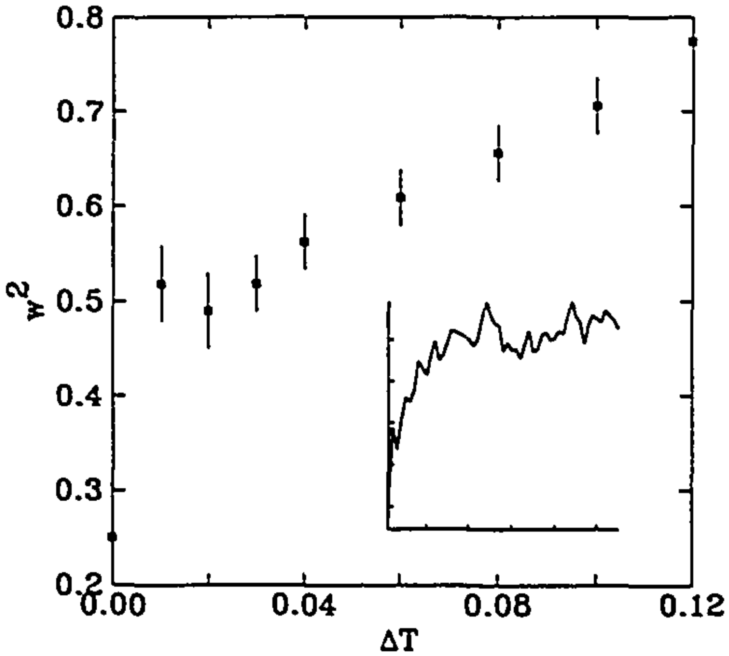

Figure 36: The average squared width of driven steady-state planar interfaces at $T = 0.5\ T_c$ for under-coolings of $\Delta T \in [0.02, 0.12]\ T_c$; the inset shows the time dependent width of a typical driven interface. The critical driving force is estimated to be $\Delta T \approx 0.04\ T_c$. Note: The width for zero driving force is from equilibrium simulations.

the relatively large activation energy required for growth; when thermal fluctuations are smaller than the critical fluctuation size, the growth may hesitate between layers. Figure 36 shows steady-state values of $\langle w^2 \rangle$ for various $\triangle T$, showing a weak transition near 0.04 T_c; the inset shows a typical time evolution of the width of an interface.

Results

We have qualified the behaviour of a driven steady-state interface in the presence of a thermal gradient in terms of $\langle A \rangle$, A_o and $\langle w^2 \rangle$. We have confirmed the fact of distinct responses for faceted and roughened interfaces to changes in the driving force; in both cases, simulation results are in good agreement with analytic expressions. We have observed an oscillatory behaviour in the interface which is related to nucleation-limited growth. We suggest that the presence of these oscillations beyond the measured kinetic transition point is consistent with the broadening of the transition.

6 Linear Stability: the Mullins-Sekerka Instability in Two Dimensions

Before we begin to examine the non-linear late-time non-equilibrium behaviour of the Mullins-Sekerka instability, it is prudent to compare our algorithm's behaviour to the predictions of the linear stability analysis in Chapter 3. This will serve two purposes: First, it will be the first direct confirmation of the theoretical analysis ever performed in simulation or experiment. Second, a positive result will lend additional credence to the supposition that our model is capable of reproducing the basic elements of the instability dynamics; consequently, conclusions drawn on the non-linear behaviour presented in Chapter 7 could be presumed to be applicable to the general Mullins-Sekerka mechanism. In Chapter 3, we examined the case of a planar interface and of a droplet interface in the presence of thermal gradient.

In the planar case, we have found the linear regime of the Mullins-Sekerka instability to be short-lived in the Ising model, and subsequently difficult to observe. Following the approach of other studies of linear behaviour (Heermann 1984; Grant et al. 1985), we will extend the timescale for the linear growth by using a longer range of spin interaction; the basic Hamiltonian is modified to include neighbours over a range ϱ. In order to produce reasonable results, we will require a very large ensemble of trials to reduce statistical noise and a very large system size to see a sufficient range of instability modes. The cpu-intensive nature of the interaction, coupled with hardware and time constraints, suggest that we examine the linear stability regime in two dimensions. There are no important differences in the basic instability behaviour between interfaces in two and three dimensions at temperatures above the three dimensional roughening transition, so this creates no particular problems. In Section 6.1, we summarize the reasoning behind the long-range interaction approach and outline the modifications to the standard code. We then present our results for the dispersion relation of the growth modes.

Similar difficulties working with the droplet instability in three dimensions have also led us to study an unstable disk in two dimensions, looking for the predicted instability radius. This case is less sensitive to the problems of the linear growth regime since the timescale is set by the rate of growth of the interface. In Section 6.2, we re-derive the linear stability description for a disk (slightly different results from 3D) and compare the predictions for the onset of instability with our simulations using two distinct measurements.

6.1 The Planar Interface Instability at Early Times

Theory

Based on the analysis in Section 3.1, we expect an exponential time dependence of the growing modes k on a planar interface in the linear regime

$$h(x) = h_o(x) + \sum_k \hat{\zeta}(k) e^{ikx+\omega(k)t}.$$

We are interested in extracting the dispersion relation $\omega(k)$ from the measured power spectra of the interface. Recall that the linear stability analysis predicts the form of equation (63),

$$\omega(k) \cong kv \left(1 - d_o \ell k^2\right).$$

To extend the regime of the linear stability on the planar interface, we first modify the basic simulation model to include a longer range of interaction. This slows the dynamics without changing the overall characteristics of the system and thus permits us to measure the onset of the instability. Binder (1984a) originally showed that an increased range of site-site interaction extends the linear behaviour of quenched systems during the early stages of coarsening; we can use this same approach to access the linear regime of the Mullins-Sekerka growth mechanism.

First, let's look at the timescales of the linear regime in the instability. Examining the expressions for the perturbed thermal field, (56) and (57), we see that, at the interface $z = 0$, the field has a time dependence like

$$u(t) \propto e^{\omega_k t} + \mathcal{O}(h) \tag{110}$$

where $\mathcal{O}(h)$ is an interface perturbation; from (54), we can see that it also has the form $h(\mathbf{x}, t) \sim e^{\omega_k t}$. The perturbation expansion of (110) is singular; this suggests that the linear behaviour is likely very difficult to observe. This has been found to be the case in other unstable systems such as alloys undergoing order-disorder transition (Binder 1983; Binder 1984b). Assuming that ϱ is the range of interaction we expect to observe correlations of size ϱ in the linear regime. Making some rough estimates, we can say that the wavenumber $k_\varrho \sim 1/\varrho$ represents the critical k for this interaction. To first order in ω_k, this mode should grow like $e^{k_\varrho t}$ and the correction $\mathcal{O}(h)$ should become important when it is of the order ϱ in size. Therefore we expect the linear regime to exist up to length scales $e^{t k_\varrho} \sim \varrho$ or timescales up to

$$\tau_{lin} \propto \varrho \, \ln(\varrho).$$

Thus, we conclude that extending the range of interaction increases the timescale of the linear growth regime.

The modified algorithm is essentially identical to the model described in Chapter 4 except that the interaction is extended over neighbours within ϱ of each spin. The neighbourhood is a *diamond* shaped region containing $2\varrho(\varrho + 1)$ sites around the central site (see Figure 37); ϱ is restricted to integer values and refers to the distance in lattice spacings along one of the Cartesian axes. We have empirically chosen $\varrho = 3$ as the best compromise between cpu time and the timescale for linear stability. With

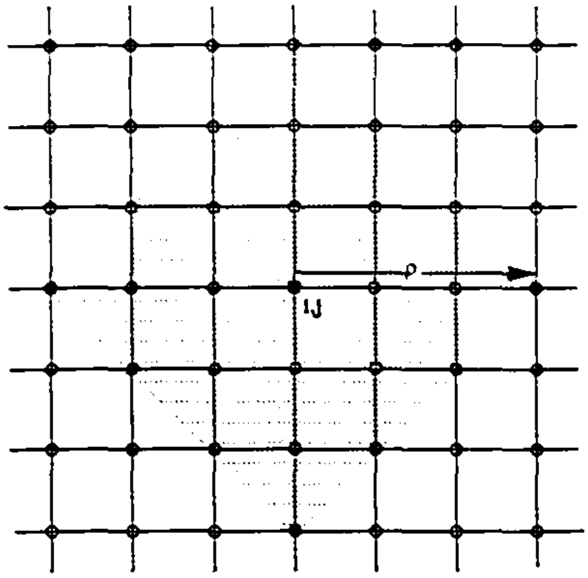

Figure 37: A diagram of the long-range interaction neighbour scheme. The range of interaction is defined to be ϱ. The coupling is equal between all neighbour spins.

this value, linear stability appears to last for approximately 1000 MCS, based on the behaviour of growth modes.

Simulation

Our data was from a planar interface of size 8196 × 28 at $T_m = 0.9\ T_c$ with an undercooling in the liquid melt of $T = 0.2\ T_c$ where $T_c \simeq 2.269\ J$ in two dimensions. The spin degeneracy was $\delta = 3$ with a latent heat of transition $\mathcal{L} = 1.22\ J$. The

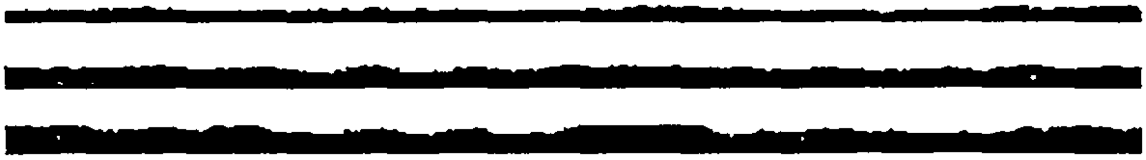

Figure 38: A time series of the 2D planar instability with long-range interactions. The system size is 8196 × 24 but only a section 550 × 24 is shown here.

interface was pre-initialized from the same interface in equilibrium at T_m. The system was allowed to go unstable for 1000 Monte Carlo steps during which time the Fourier spectrum of modes was measured. Figure 38 shows a time series of a typical 1D planar interface during the linear stages of the instability. An earlier study (Harris and Grant 1990) examined the late-time behaviour of a similar interface using the same model and comparable system parameters. They observed dendrite-like fingers with a characteristic lengthscale, consistent with the conventional picture of the Mullins-Sekerka instability.

As in previous studies (Jörgenson, Harris and Grant 1989; Harris and Grant 1990), the most informative method for analysing the interface is via the power spectrum of its fluctuations; the telltale roughening modes and the time dependence of the instability are easily identifiable. The interface power spectrum $P(k,t)$ was averaged over 400 trials where

$$P(\mathbf{k}) \equiv |\mathcal{F}\{h(\mathbf{x})\}|^2 \tag{111}$$

and $\mathcal{F}\{h(x)\}$ is the spatial Fourier transform in one dimension

$$\begin{aligned} \bar{h}(\mathbf{k}) &\equiv \mathcal{F}(h(\mathbf{x})) \\ &= \int d\mathbf{x}\, e^{\imath \mathbf{k}\cdot\mathbf{x}}\, h(\mathbf{x}). \end{aligned} \tag{112}$$

Figure 39 shows a time series of the averaged spectra over the time of the run for $t = 100, 500$ and 1000 MCS. Note the modes at high k which are typical of interface roughening. The modes which extend above the solid line representing the steady-state roughening level are the growth modes; the area between the solid line and the curve(s) is the excess power attributed to the instability.

We are looking for an exponential time dependence of k; Figure 40 shows some typical growth modes as a function of t. As we can see, the behaviour is more or less consistent with our expectations. The higher k modes are rougher and tend to saturate at late t. Also, the occasional k mode like that shown in Figure 40 c) appears

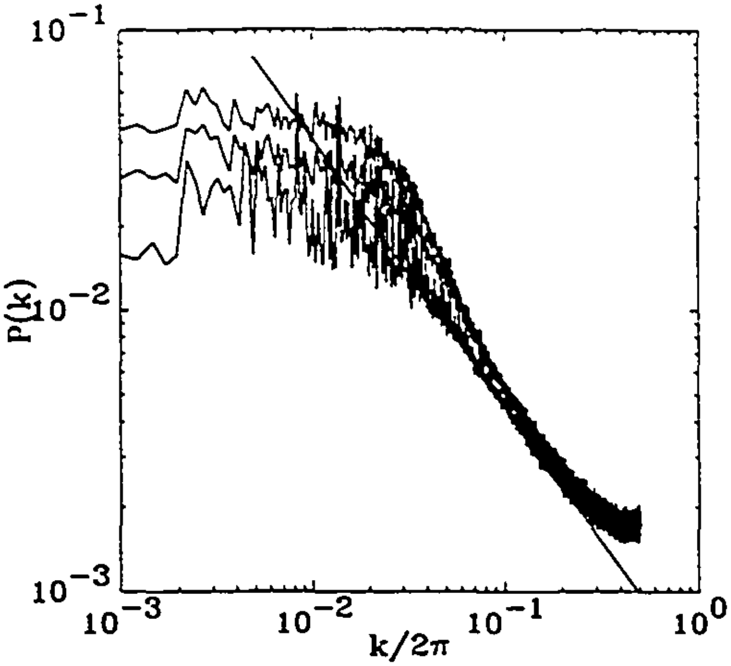

Figure 39: The power spectra of the unstable planar interface at t = 100, 500 and 1000 MCS as shown in Figure 38. Note the static modes at high k which are characteristic of interface roughening. The solid line approximates the steady-state roughening modes.

to have been initialized with too much power; it exhibits an early-t tail as it quickly relaxes to local equilibrium and begins to grow normally again.

We would like to extract the dispersion relation (63). Each k mode was individually fitted via a least-squares algorithm with an expression $Ae^{\omega_k t}$ where A and ω_k were the fitting parameters. The very earliest and latest times were ignored to avoid the influences of poor initialization and saturation, respectively. In Figure 41, we show ω_k for all of the k modes in the power spectrum up to $k = 2\pi/10$ (higher k modes were uninteresting); errors in the fits of ω_k are much smaller than the variations in their value. Despite the large number of runs (n=400), the noise is still significant.

There are several features which are different from the theoretical curve shown in Figure 13: First, the decay modes are not represented; this is because they are overwhelmed by the equilibrium capillary modes, already present because of the initial

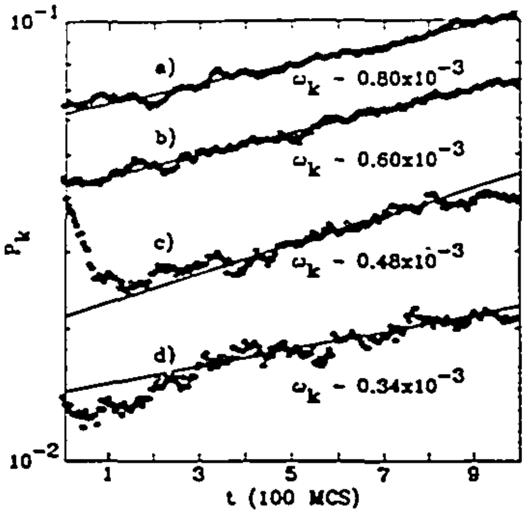

Figure 40: Time series of some typical growth modes below the critical mode $k_o \equiv 2\pi/\lambda_o \sim 2\pi/17\,a$; a) $k \sim 2\pi/74\,a$, b) $k \sim 2\pi/41\,a$, c) $k \sim 2\pi/26\,a$ and d) $k = 2\pi/21\,a$ in semi-log plots. The growth modes are predicted to evolve in time like $e^{\omega_k t}$; the straight solid lines are the fits to this form, disregarding the very earliest and very latest times. The fitted values for ω_k are indicated. Note that the higher k values fall off as they approach saturation values. Also, c) shows a tail at $t \simeq 0$; this appears to be due to an over-strong initial amplitude which quickly relaxed to local equilibrium.

conditions. Thus, we simply observe ω_k going to zero at the critical mode k_o. Second, the wavenumber of the dominant growth mode k_{max} is near the limit of the system size and consequently the lowest k modes beyond the dominant k mode are not all present.

Due to the noise in the measurements, it is difficult to identify the lengthscale of maximum growth λ_{max} and the critical lengthscale λ_o (64) as defined in Section 3.1. From Figure 41, we estimate by eye

$$\begin{aligned} \lambda_{max} &\equiv 2\pi/k_{max} &&\sim 51a \pm 10 \\ \lambda_o &\equiv 2\pi/k_o &&\sim 16a \pm 4. \end{aligned}$$

It is apparent that these results are not consistent with the relationship $\lambda_{max}/\lambda_o = \sqrt{3}$. Further study would be required to determine if this is symptomatic of the noise or intrinsic to the model.

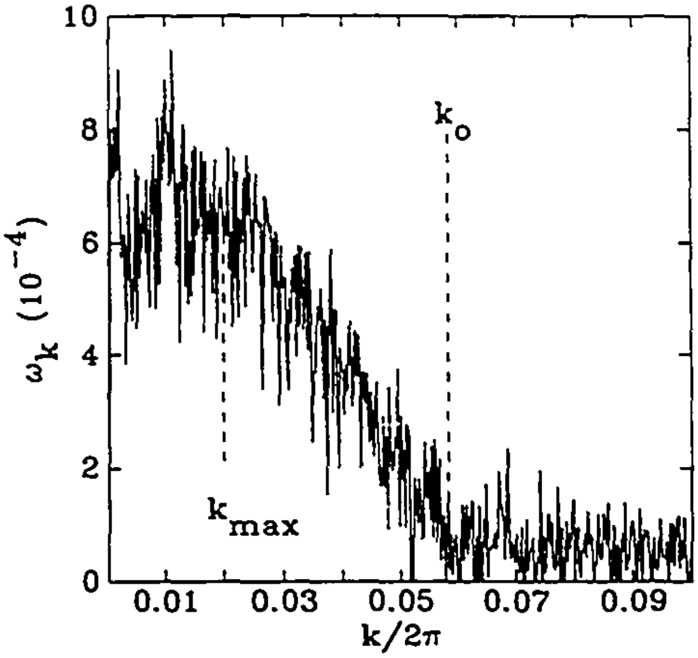

Figure 41: The linear stability dispersion function from fits of the planar interface modes to the expected exponential behaviour. These results are based on 400 simulation trials of an 8196 × 24 system which employs a long-range interaction ($\varrho = 3$). Error bars are much smaller than the noise.

In conclusion, we appear to have limited success in confirming the predictions of the linear stability analysis. The data is not inconsistent with expectations, however there are some questions which are not clearly answered due to the poor statistics. In particular, there is some concern about the ratio λ_{max}/λ_o.

6.2 The Circular Interface Instability at Early Times

Theory

Another simple test of the linear stability analysis is provided by the case of the circular droplet in an undercooled melt. If the initial radius of the droplet $R = R_o$ is larger than the critical radius R^*, it will start to grow. As described in Section 3.2 for the case of a droplet in 3D, it will remain circularly stable while $R < R^*_m$, where m is the mode of the instability. At R^*, it will become unstable and begin to grow fingers typical of the Mullins-Sekerka instability (see Figure 42). Here, we shall briefly derive solutions for the linear stability problem for a circular interface and then we compare them with simulation results.

Re-capping the relevant equations for the thermal diffusion problem, we use two-dimensional equivalents of (49)-(51);

$D\nabla^2 u = 0$	steady state thermal diffusion
$u_\perp = -d_o\kappa$	Gibbs – Thomson relation
$v_\perp = D[\alpha(\nabla u)\mid_{sol} - (\nabla u)\mid_{liq}]\cdot\hat{\mathrm{n}}$	interface continuity
$u(\infty) = -\Lambda$	boundary condition at infinity

Assuming a perfect circle of radius $R_o(t)$, we have unperturbed solutions for $u(r)$

$$u_o(r) = \begin{cases} (\Lambda R_o - d_o)/r - \Lambda & r \geq R_o \quad (liquid) \\ -d_o/R_o & r \leq R_o \quad (solid). \end{cases} \tag{113}$$

Using the continuity equation, we find the unperturbed interface velocity to be

$$\frac{dR_o}{dt} \equiv v_{R_o} = -D\nabla u \cdot \hat{r} = \frac{D(\Lambda R_o - d_o)}{R_o^2}; \tag{114}$$

this expression describes the rate of growth of the stable disk. We then introduce a small perturbation at the disk interface

$$R(\theta) = R_o + \rho_m cos(m\theta)e^{\omega_m t}; \tag{115}$$

assuming the quasi-static condition, this gives a solution for the perturbed thermal field

$$u(r) = u_o(r) + u_m(r)cos(m\theta)e^{\omega_m t} \tag{116}$$

where

$$u_m(r) = \begin{cases} A_m r^{-m} & r > R_o \quad (\mathit{liquid}) \\ B_m r^m & r \leq R_o \quad (\mathit{solid}) \end{cases} .$$

Following a linearizing procedure similar to that in Chapter 3, we evaluate the rates of the growth modes to be

$$\omega_m \simeq \frac{v_{R_o}(m-1)}{R_o}\left[1 - \frac{1}{2}(1+\alpha)\frac{2Dd_o}{v_R R_o^2}m(m-1)\right] \qquad (m \geq 2); \qquad (117)$$

where the lower limit of m for finite growth rates is 2 or greater. The instability radius for a given mode m is then defined by the limit $\omega_m \rightarrow 0$;

$$(R_m^*)^2 = \frac{1}{2}(1+\alpha)m(m+1)\frac{2Dd_o}{v_R} \qquad (118)$$

Using (114) and the 2D critical radius $R^* = d_o/\Lambda$ (see Appendix A.2), this can be re-written

$$\frac{R_m^*}{R^*} = 2m(m+1) + 1 \qquad (m \geq 2) \qquad (119)$$

where it has been assumed that the thermal characteristics of both phases are similar (ie. $\alpha \equiv (D_s C_s)/(D_l C_l) \sim 1$). If we assume that $m = 2$ will be the first unstable mode, the droplet should then be stable up to $R \sim 13\ R^*$.

The departure of the growing disk from a quasi-circular steady-state can be determined by two methods: First, the instability can be observed directly by the visual inspection of the simulation system. The onset of finger-like instabilities is dramatic and easy to identify. For greater precision, the onset can be related to the rate of change of the droplet size, dN/dt, where N is the number of sites which define the droplet. While the droplet remains stable and circular, we can use the expression (114) to fit dR_o/dt by assuming $N \simeq \pi R^2$. As it goes unstable, the droplet is no longer compact and $R(t)$ should no longer follow (114). In Appendix A.6, we offer a simple argument which suggests that $R(t)$ should follow $\sqrt{t}$ at early times and be linear in t at late times. It is unclear whether the cross-over should be apparent or not and whether it should obscure the instability behaviour.

Simulation

Since the the instability of a circular disk is tied to its radius, the timescale for the stable growth is directly defined by its radial growth rate. We can simply extend the linear regime by reducing the undercooling and we do not need to use the time-consuming long-range interaction algorithm. Subsequently, all of the results presented in this section employ the standard nearest-neighbour algorithm although we remain in two dimensions because of the same size constraints of the planar simulations.

Our simulation system size was 128 × 128 with an initial circular inclusion of $R_o = 5$ lattice units. The coexistence temperature was set to $T_m = 0.756\ T_c$ where $T_c \simeq 2.269\ J$ in two dimensions. The undercooled temperature was $T = 0.178\ T_c$ with the spin degeneracy set to $\delta = 3.21$. These particular parameters were chosen by trial and error to give a specific rate of growth without homogeneous nucleation while producing an instability at a droplet radius within the system size. The statistics were averaged over 500 trials of 2500 MCS each. The instability was observed to occur, on average, at $t \sim 1200 MCS$.

Figure 42 shows a time series of a typical droplet growth; note that although fluctuations appear before the indicated instability sets in, they are quickly damped out. Visual inspection shows that the disk becomes unstable at around $R \sim 20\ a$ where a is the unit lattice spacing. Figure 43 shows the reference radius $R(t) \equiv \sqrt{N(t)/\pi}$. We find that $R(t)$ grows like $\sim t^2$ (consistent with (114) for a large undercooling, $d_o/R_o \ll \Lambda$) up to $t \simeq 1250 MCS$ whereat $R(t)$ becomes linear in t. This corresponds to $R \sim 21\ a$.

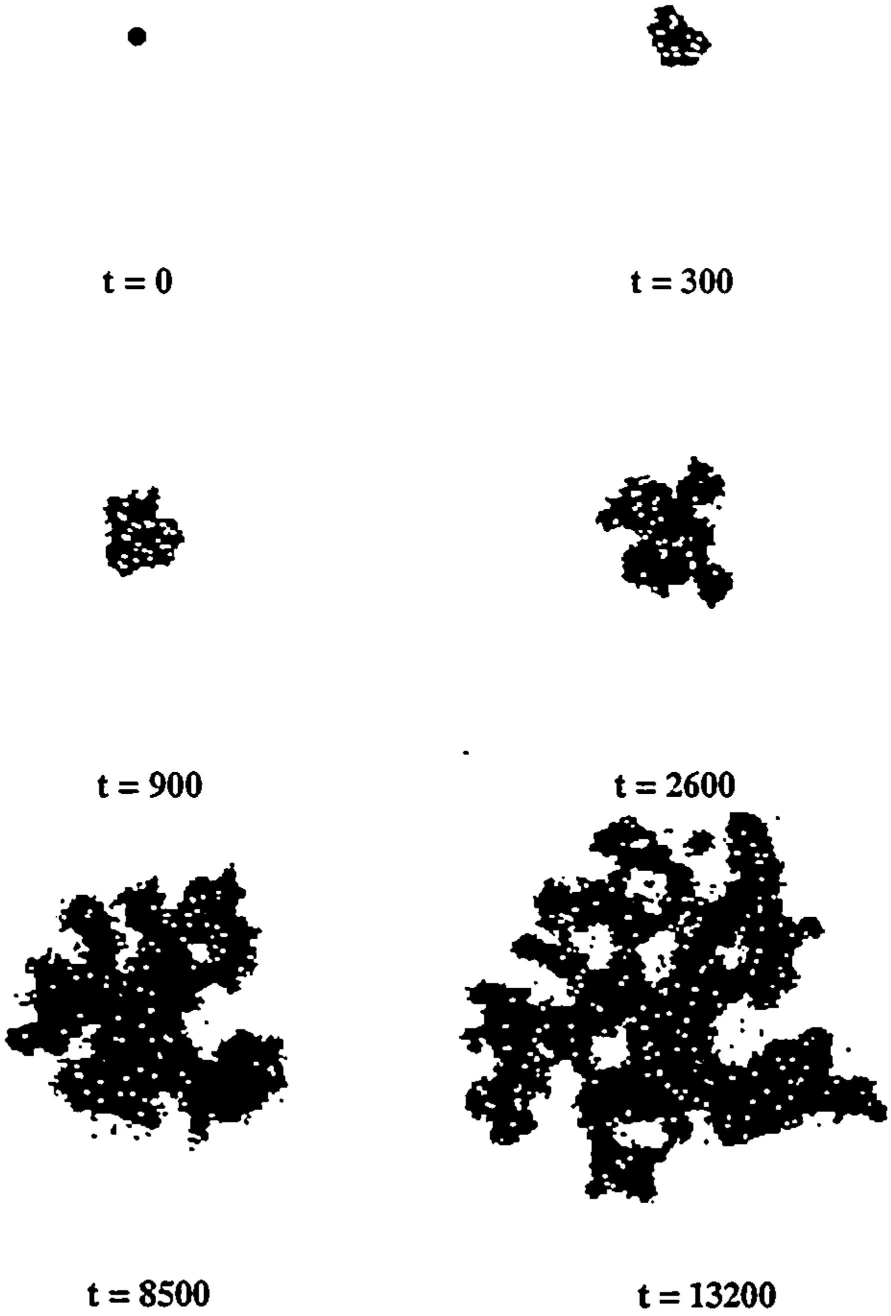

t = 0

t = 300

t = 900

t = 2600

t = 8500

t = 13200

Figure 42: A time series of the disk instability in 2D for a system of 256 × 256; images are for $t = 0, 300, 900, 2600, 8500$ and 13200. The disk remains circular up to the stability radius $R \sim 20\ x$ ($t \sim 1000$) where it then becomes unstable. Late times shows dendritic growth.

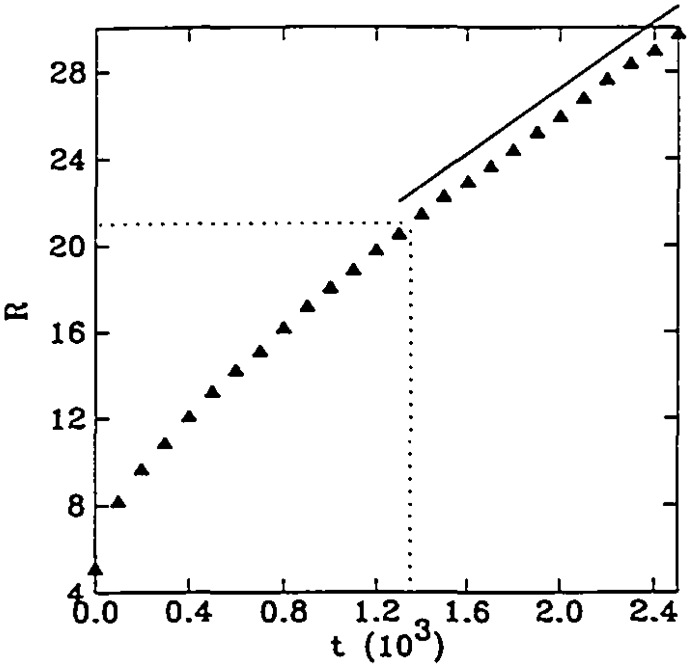

Figure 43: The reference radius $R(t) \equiv \sqrt{N(t)/\pi}$ as a function of time for the disk instability. While the disk is circular, R corresponds to the actual disk radius. When it becomes unstable and no longer compact, R grows linearly in time.

We can compare this result in two different ways using the expression (119). First we will use the critical radius from nucleation theory (see Appendix A.2) to re-express the expected instability radius as

$$R^* \equiv \frac{\gamma}{\triangle E_b}; \tag{120}$$

We can estimate R^* for a metastable disk at temperature T from values of the surface energy γ based on analytic results (Rottman and Wortis 1981) and $\triangle E_b$ based on meanfield results (see Section 4.1).

Since there is some ambiguity in identifying the local temperature at the interface, we shall choose intermediate values for these parameters, using values at the coexistence temperature and undercooled temperature at infinity as upper and lower limits. The surface energy is thus

$$\gamma(0.5T_c) \simeq 1.6\ J$$

and the bulk free energy difference between the solid at $T = 0.76\ T_c$ and the melt at $T = 0.18\ T_c$ is

$$\triangle E_b \sim 0.73\ J;$$

This gives a critical radius of

$$R^* \sim 2.3\ a$$

Needless to say, this is too small to be confirmed via a metastability test on a discrete lattice. Assuming that the lowest possible mode $m = 2$ dominates the growth, we find a prediction for the stability radius of

$$R_2^* \sim 25\ a$$

If we were instead to assume that $m = 4$ based on the square anisotropy of the lattice, we find $R_4^* \sim 93\ a$. Obviously this result supports the idea that the lowest growth mode dominates the instability.

A more direct measurement of R_m^* can be made by carrying out a secondary simulation. Returning to the prediction for R_m^*, we can re-write (119)

$$R_m^* = \sqrt{m(m+1)\frac{2Dd_o}{v_R}} \tag{121}$$

Although v_R is not strictly constant, it changes slowly and we can assign it a value for a given R. We then only need d_o and D to find a solution.

Since a droplet at $R < R^*$ is always circularly stable, we can observe the *evaporation* of the droplet from an initial radius R_o at the coexistence temperature T_m.

There is no undercooling except near the interface where latent heat is absorbed by the phase transition; the boundaries will add heat continuously to the system to keep it at T_m. The droplet then evaporates at a rate defined by (114); for example, $\Lambda \ll d_o/R_o$ gives an approximate expression

$$R(t) \simeq \sqrt[3]{R_o^3 - 3Dd_o t}. \tag{122}$$

Figure 44 shows the reference radius of an evaporating droplet from a typical simulation run for a 128 × 128 system with an initial droplet of size $R_o = 50$. The

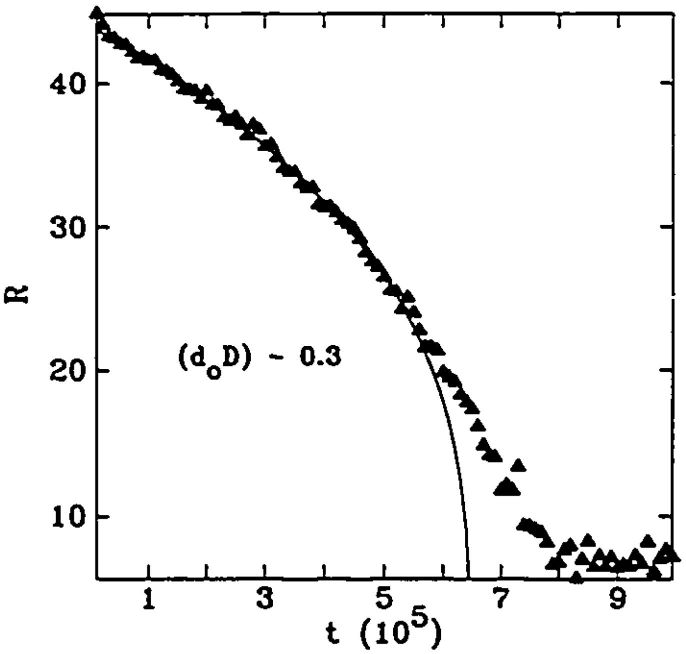

Figure 44: The radius R(t) for an evaporating disk. Also shown is a fit via a Runga-Kutta integration method to equation (114) with (d_oD) as a fitting parameter.

ambient temperature was set to the coexistence temperature $T_m = 0.756\ T_c$. From a fit of $R(t)$ using (114) via a Runga-Kutta integration method, we find $(d_oD) \simeq 0.3$; the fit is expected be poor for small R due to finite size effects. From the growth simulation data, we estimate the interface velocity to be $v_R \simeq 0.009$ lattice units per

MCS. This gives an instability radius

$$R^*_2 \simeq 20\ a.$$

It is apparent that both estimates of R^*_2 are consistent with our simulation results.

Results

The form of the dispersion relation of the linear regime of the planar instability has been found to be in good agreement with the prediction of theory. However, the ratio of the wavelength of maximum instability with the critical wavelength is somewhat larger than the expected value. The instability radius of a disk interface is in good agreement with predictions, using two distinct techniques for measuring it. Overall, this is viewed as a confirmation of the feasibility of our model for use in the study of dynamical processes.

7 Non-Linear Growth: the Mullins-Sekerka Instability in Three Dimensions

After passing through the brief linear stability regime, described in Chapter 3 and examined in Chapter 6, an unstable interface enters a non-linear regime of growth. Certain wavelengths begin to dominate the instability; fingers appear and advance ahead of the initial interface. These fingers or *dendrites* compete for space until only a few reach their steady state. The others slow and stop as the undercooled melt in front of them is heated by the excess latent heat released by their neighbours. The growing dendrites reach a terminal tip velocity which remains constant. As they grow, perturbations along their sides begin to appear. These grow to form secondary dendrites or *side-branches*. Tertiary growths may also appear as space allows. This cascading dendritic growth eventually forms highly intricate and structured patterns.

Figure 45: Dendritic growth in two distinct geometries: In a), a succinonitrile dendrite growing between flat glass plates (reproduced from (Qian and Cummins 1990)) and in b), dendrites observed in a crack in single-crystal alloy PWA-1480 at the Oak Ridge National Laboratory; reproduced from (Langer 1992).

Their symmetries reflect the underlying crystal anisotropy of the solid; Figure 45 shows some typical examples of physical crystal growths in a quasi-two-dimensional and a three-dimensional context. In some cases, like the snowflake shown in Figure 1 of the introduction, the faceting normally associated with roughening transition is observed on the leading tip of the dendrite; this is a special case of the interface instability in close proximity to the *dynamic* roughening transition, as discussed in Section 5.4.

Although the challenge of simulating the Mullins-Sekerka instability in three dimensions is not unsurmountable, it does create certain (currently) insoluble problems. For example, in order to apply the linear stability analysis, we must satisfy the quasi-stationary assumption; since the interface grows to first order like $\omega_{int} \sim kv$ and the thermal field relaxes like $\omega_{diff} \sim Dk^2$, we need $\omega_{diff}/\omega_{int} \sim k\ell \gg 1$. This implies that there exists a reasonably large separation in the two important quantities, the capillary length d_o and the thermal diffusion length ℓ. In the modified Ising model used in work presented here, d_o is usually of order of the lattice spacing. A reasonable separation of two orders of magnitude (recall that the instability wavelength $k \sim \sqrt{d_o\ell}$) suggests a system size that is, at minimum, 100^3 sites and preferably closer to 1000^3 since we don't want ℓ to be near the limit of the system size. This upper estimate is a billion lattice sites and somewhat beyond the upper edge of the technology available to us; moreover, a Monte Carlo step over so many sites requires several (real) seconds on the machines available to us. Two avenues were chosen to deal with this: We greatly reduced one dimension of the simulation system and subsequently increased the other two. This approaches the two dimensional system examined in previous studies (Harris, Jörgenson and Grant 1992). Alternately, we limited the vertical size of the system and examined only the early non-linear growth in three dimensions. We refer to these two approaches as the *slab* and *block* geometries respectively (see Section 4.4 and Appendix A.1).

7.1 Unstable Slab Interfaces

The original motivation for using the slab geometry was to be able to extend the length scales of the simulation well beyond any characteristic lengthscales. As we will observe in Section 7.2, the fully three dimensional system leaves very little room for growth; multiple dendrites are rare and sidebranching is nearly non-existent. The much larger slab interface permits many dendrites to grow for longer times. Further, we are supported in this choice by physical experiments on succinonitrile (Chou and Cummins 1988; Qian and Cummins 1990) and NH_4Br (Maurer, Bouissou and Perrin 1989) carried out with apparatus of similar proportions. Our simulations also provide some insight into the cross-over from the 2D to 3D regimes; we will see how the additional degree of freedom influences the growth.

A typical simulation system size is $8 \times 1024 \times 192$. A run begins from a flat interface with the solid bulk phase initialized at T_m, the melting temperature, and the liquid bulk phase at an undercooled temperature, $T_u < T_m$. Finger-like instabilities form immediately and quickly reach the asymptotic regime (typically within 400 Monte Carlo steps) where tip velocities are constant. The dendrites continue to grow until the end of the run when they reach the far side of the system. Figure 46 shows a time series of cross-sectional slices from a slab system; the section shown is only a selected portion of the entire interface.

Tip velocity is measured by identifying the maximum height of the interface as a function of time; while not strictly exact, this technique is highly effective and quite accurate for measuring the primary instability. Using a $8 \times 1024 \times 96$ slab system with $T_u = 0.4T_c$, $T_m = 0.8T_c$ and $\delta = 2.8$, the tip velocity v is measured to be 3.1 x 10^{-2} in units of lattice spacings per MCS, for $400 \geq t \geq 1000 MCS$. This result, shown in Figure 47, is based on 29 trials of 2400 MCS each.

As seen in Figure 47, the surface area increases with a t^2 power law; this is

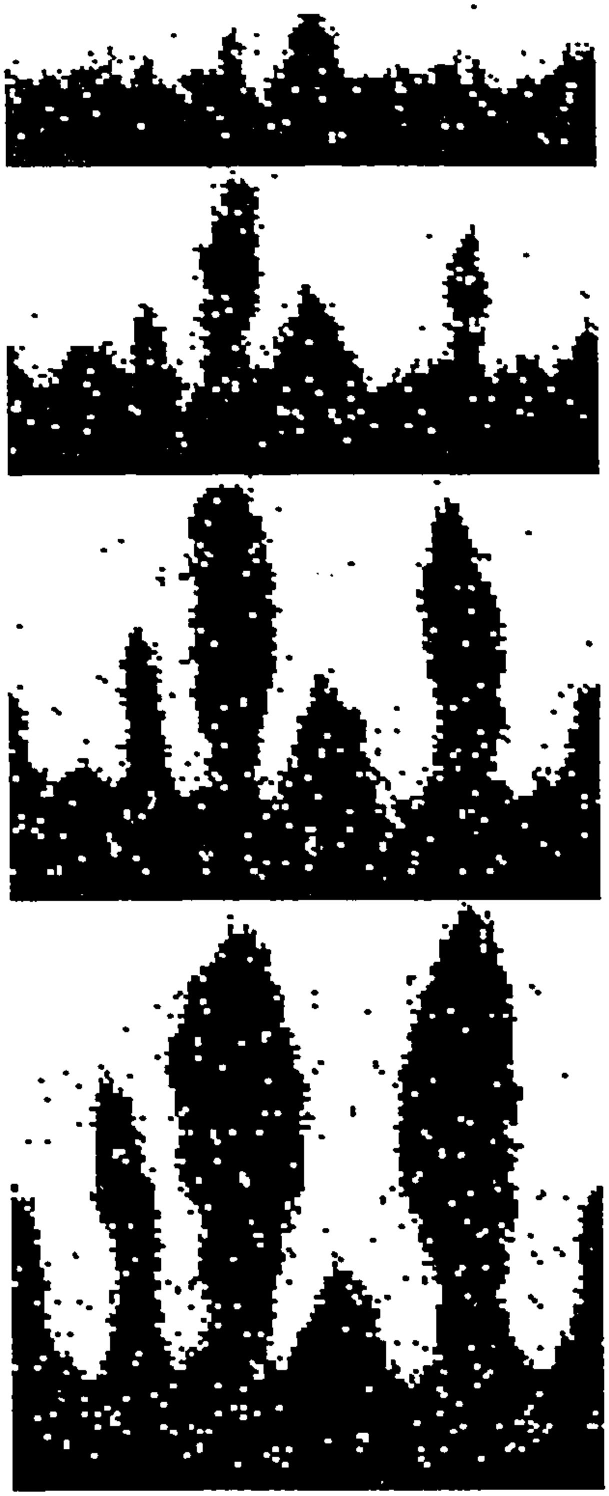

Figure 46: Time series of cross-sectional views of a *slab* system of dimension $8 \times 128 \times 92$. This is a sub-section of the larger $8 \times 1024 \times 92$ system used to generate data. The images shown are for t=1000, 4000, 10000, 26000 MCS. The corresponding thermal field for t=25000 MCS is shown in Figure 59.

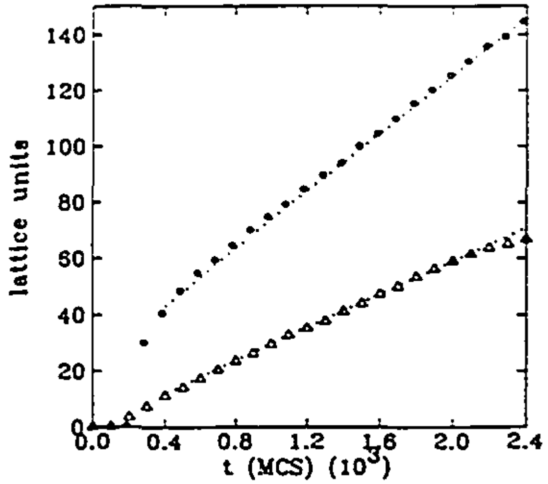

Figure 47: Maximum height (tip position) (∘) and the (square root of the) total surface area (△) plotted against time t for a $8 \times 1024 \times 96$ slab system. The surface area is shown as $\sqrt{A(t) - A(200)}$ to highlight the t^2 growth, with $A(200)$ being 28249 units. Data is averaged over 29 runs.

appropriate to fingers growing at a constant velocity v early in the non-linear growth. regardless of dimensionality (see Appendix A.6). The tip radii of curvature ρ are of order of the unit lattice spacing ($\simeq 3$) and tend to fluctuate strongly due to the influence of roughening. This value is needed to check the relationship between ρ and v (82) derived in Section 3.3. However, we have found that measurements of ρ are insufficiently accurate for use. This is unfortunate as the ρ/v relation is one of the most important ways of characterizing the instability (Langer and Müller-Krumbhaar 1978); in general, its complex nature makes it difficult to quantify its behaviour.

Thus we return once again to the most direct way to exhibit the unstable modes, via the power spectrum $P(k,t)$ of the interface. However, we find that the measurement of $P(k,t)$ is also difficult; typical interfaces have overhangs, bubbles and pockets. These are presumed to be unimportant since they occur on length scales which are much shorter than the lengths of interest. They are therefore masked out by projecting the multi-valued interface onto the X-Y plane such that the interface is approximated by an iso-valued surface. This surface is then collapsed to a 1D function $h(x)$ by averaging along the shortest axis and treated by Fourier transform to produce the power spectrum $P(k)$ as in (112).

In Figure 48, $k^2P(k)$ is shown; the scaling removes the expected k^2 roughening contribution. Only the unstable modes below the roughening continuum are shown; they indicate a wavelength of maximum instability of $\lambda_1 \simeq 50$ lattice units with a secondary peak $\lambda_2 \simeq 36$ units. The entire spectrum is shown as an unscaled log-log plot in the inset. This is consistent with a visual inspection (Figure 46) which

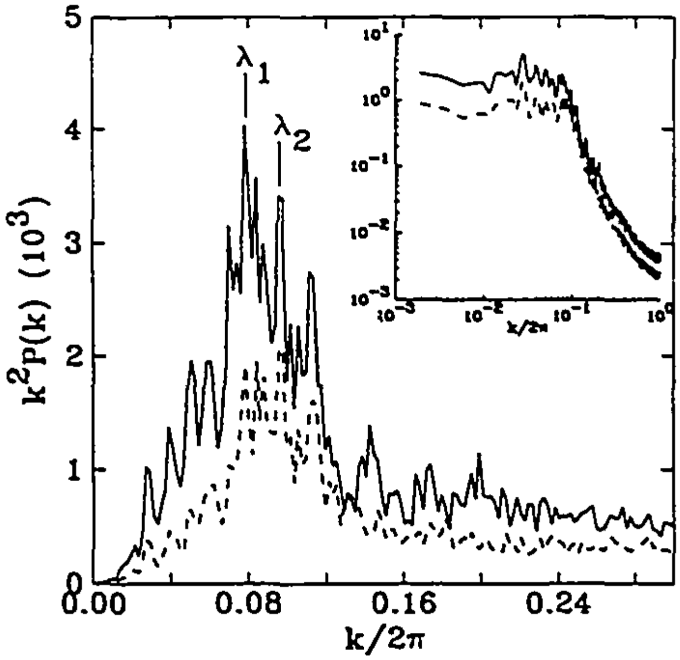

Figure 48: The power spectra for a slab system scaled by k^2. The large-k end of the spectrum, showing the expected k^2 roughening modes, is excluded to display the unstable modes more clearly. The inset shows the entire unscaled spectra in log-log plot. Spectra for t=2400 MCS and 1600 MCS are shown.

shows a typical separation between the instabilities of about 30-40 units. The same spectra are shown in Figure 49, scaled with the square of time, t^2; the fact that they are now independent of time is consistent with the surface area growing like t^2. The coarsening, as indicated by the lateral shift in the λ_{max} peak, can be ignored as

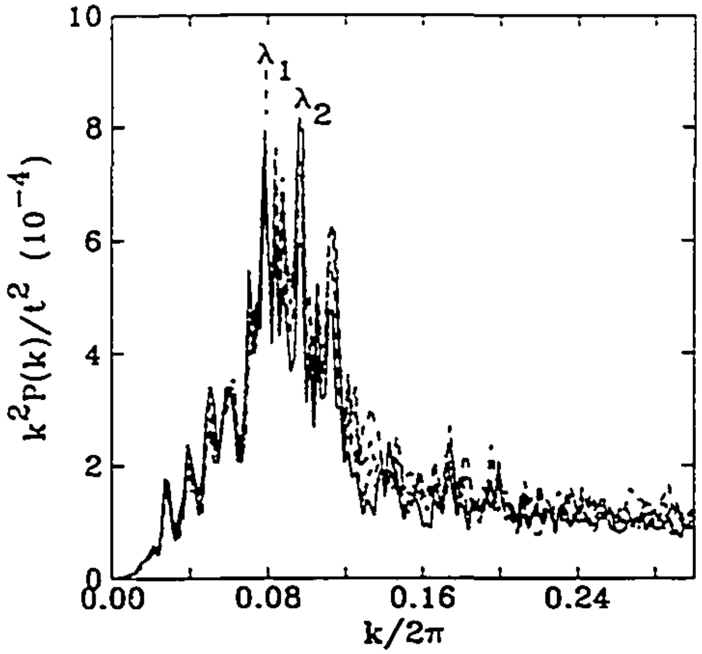

Figure 49: The power spectra from Figure 48 are shown scaled by t^2. Spectra are shown for t=2400, 2200, 2000, 1800 and 1600 MCS. The primary and secondary modes of the instability are shown as $\lambda_{1,2}$.

insignificant; in this respect, the data is very similar to that previously obtained for two dimensional systems (Harris, Jōrgenson and Grant 1992). The features to the left of the maximum are subharmonics of the primary and secondary instability peaks; they are located at $\lambda \simeq 66, 83, 100$ and 153 units.

7.2 Unstable Block Interfaces

Figure 50 shows 3D representations of *block* simulations at late time; note that dendrite growth is limited by the low ceiling on the system. In the block system of $128 \times 128 \times 96$ with $T_u = 0.3T_c$, $T_m = 0.7T_c$ and $\delta = 2.8$, the tip velocity is measured to be 2.9 x 10^{-2}; note that this is comparable to the slab value.

Similar to the slab systems, the surface area grows with a t^2 power law; this is

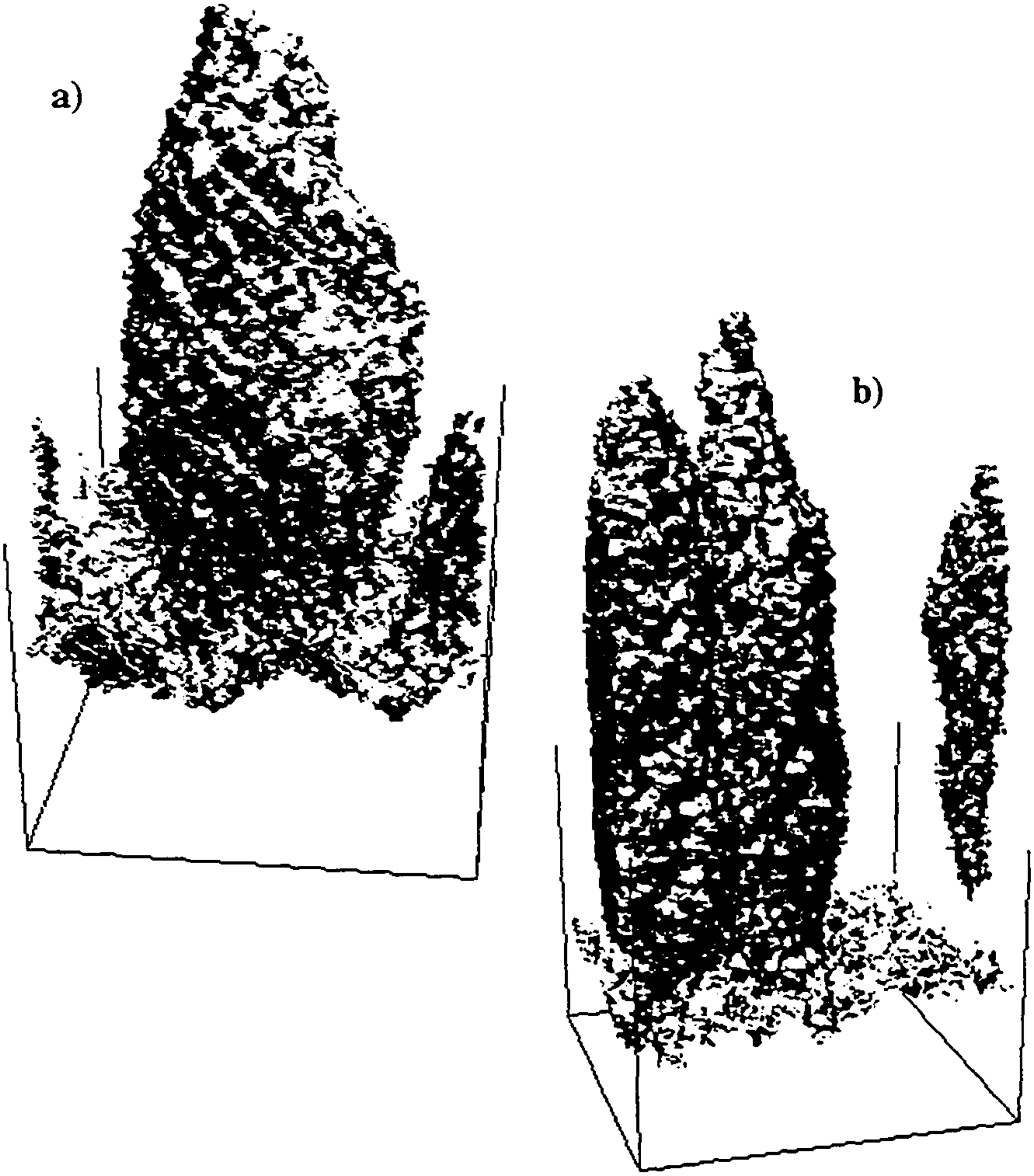

Figure 50: Two representations of 72 x 72 x 144 *block* system surfaces at late times. The image in a) corresponds to the thermal field in Figure 60 g) (right half) ; b) corresponds to Figure 60 h) (right half). Note that the boundary conditions are periodic on the sides.

shown in Figure 51. This is not suprising as no dimensionality is associated with this

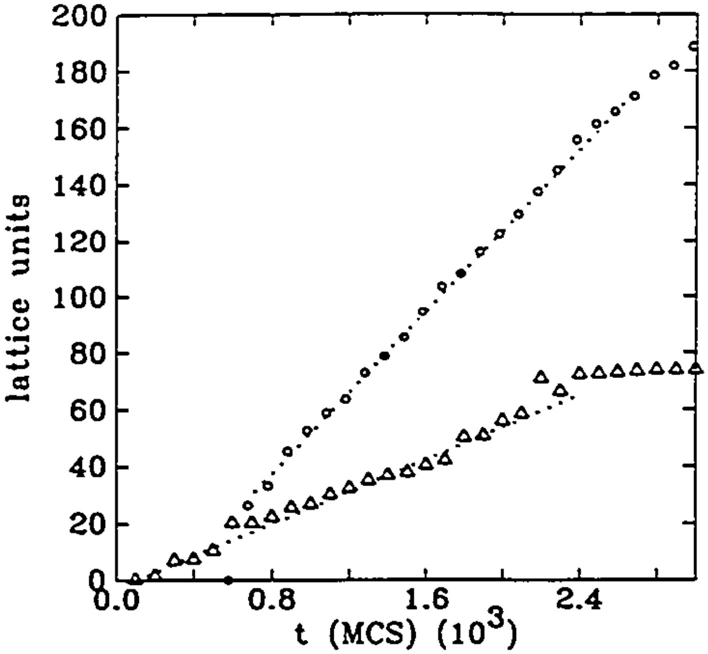

Figure 51: Point of maximum height (tip position) (○) and the total surface area (△) for a typical block system as a function of time. The surface area is shown as $\sqrt{A(t) - A(700)}$ to highlight the t^2 growth, with $A(700)$ being 42693. The tip position saturates at late times as the tallest dendrite reaches the top of the system. Data is averaged over 4 runs. The straight dotted lines provided as references.

behaviour (see Appendix A.6). The tip radii, ρ, are again of order of the unit lattice spacing and are still too roughened to be measured reliably.

Measuring the power spectrum is slightly more complicated than in the slab system. Similar to the slab systems, the block interface is reduced to a single-valued surface, eliminating overhangs and bubbles. It is then treated by a 2D spatial Fourier transform

$$\tilde{h}(\mathbf{k}) \equiv \mathcal{F}\{h(\mathbf{x})\} = \int\int dy\, dx\; e^{\imath \mathbf{k}\cdot\mathbf{x}}\, h(\mathbf{x});$$

the power spectrum $P(\mathbf{k})$ is then averaged over all orientations of the vector $\mathbf{k}$. Figure 52 shows the spectra $k^2P(k)$; it clearly shows the mode of maximum instability,

k_{max}. The expected k^2 roughening contribution at large k is apparent as is the time dependent relaxation of the roughening.

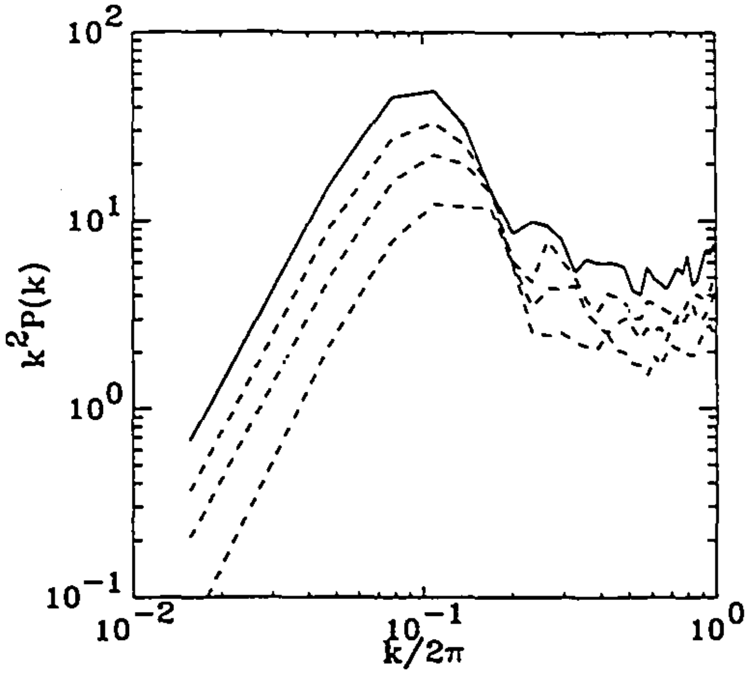

Figure 52: The power spectra for a block system scaled by k^2 is shown in a log-log plot. Spectra for t=3000, 2600, 2200, and 1800 MCS are shown. Note the k^2 region at large k, indicative of roughening fluctuations, and the lateral shift of the mode of maximum instability.

The block power spectra, shown in Figure 52, have better statistics than those of the slab in Figure 48; however, it is clear that λ_{max} is near the size of the system. In our experience, $128 \times 128 \times N_z$ is the minimum useful system size for the instabilities that we have been able to observe; results from systems of $64 \times 64 \times N_z$ clearly show the effects of finite size and are inappropriate for analysis. Consequently, this limits the height of the system permitted by hardware constraints to $N_z \sim 100$.

The k_{max} value is distinctly shifted in time by coarsening of the dendrites; this has been established by analysing the perpendicular cross-section of the interface profile at a fixed height. Figure 53 shows a times series of a typical cross-section. It starts from $t_o = 1000MCS$ when the interface first intersects the plane at the height where the lateral cross-sections are viewed. Figure 54 is the measured structure factor which is growing as a $t^{1/2}$. This is consistent with the geometric picture of the cross-section of a parabola moving through a plane with constant velocity: Consider a parabola defined $z(x, y) = at - b(x^2 + y^2)$ so that its apex is moving in the $\hat{z}$ direction at constant speed. At a fixed height z, the intersection with the $x - y$ plane is a circle defined by $x^2 + y^2 = R^2(t)$ where $R^2(t) = (at - z)/b$ and the radius goes like $t^{1/2}$. The structure factor corresponds to the average radius of the growing dendrite cross-sections.

The coarsening of the dendrites requires that a more sophisticated scaling of the power spectra be done. The scaling ansatz is of the form

$$P(k,t) = t^{2+\alpha}\tilde{P}(kt^{\alpha})$$

where $\alpha = 0.5$ is due to the coarsening. The scaling of k accounts for the shifting of the spectra's features due to the widening of the dendrite structures and the power of α on the prefactor t scales $P(k,t)$ for the enhanced rate of increase of the surface area.

To illustrate this, we show in Figure 55 a plot of $k^2\tilde{P}$ against kt^{α}.

7.3 Side Branching

The features which are missing from these simulations, both in the slab and block configurations, is the secondary instabilities along the sides of the growing dendrites; this phenomenon is generally referred to as *side-branching*. It is observed in many laboratory experiments (Dougherty and Gollub 1988; Qian and Cummins 1990) and has been reproduced in some simulation work in two dimensions using lattice-gas models (Saito and Ueta 1989) and numerical simulation of analytic dendrite models (Saito, Goldbeck-Wood and Müller-Krumbhaar 1988; Kessler, Koplik and Levine 1988). The origin and characteristics of the branches are of central concern in theories of the Mullins-Sekerka instability. Their conspicuous absence in this work is

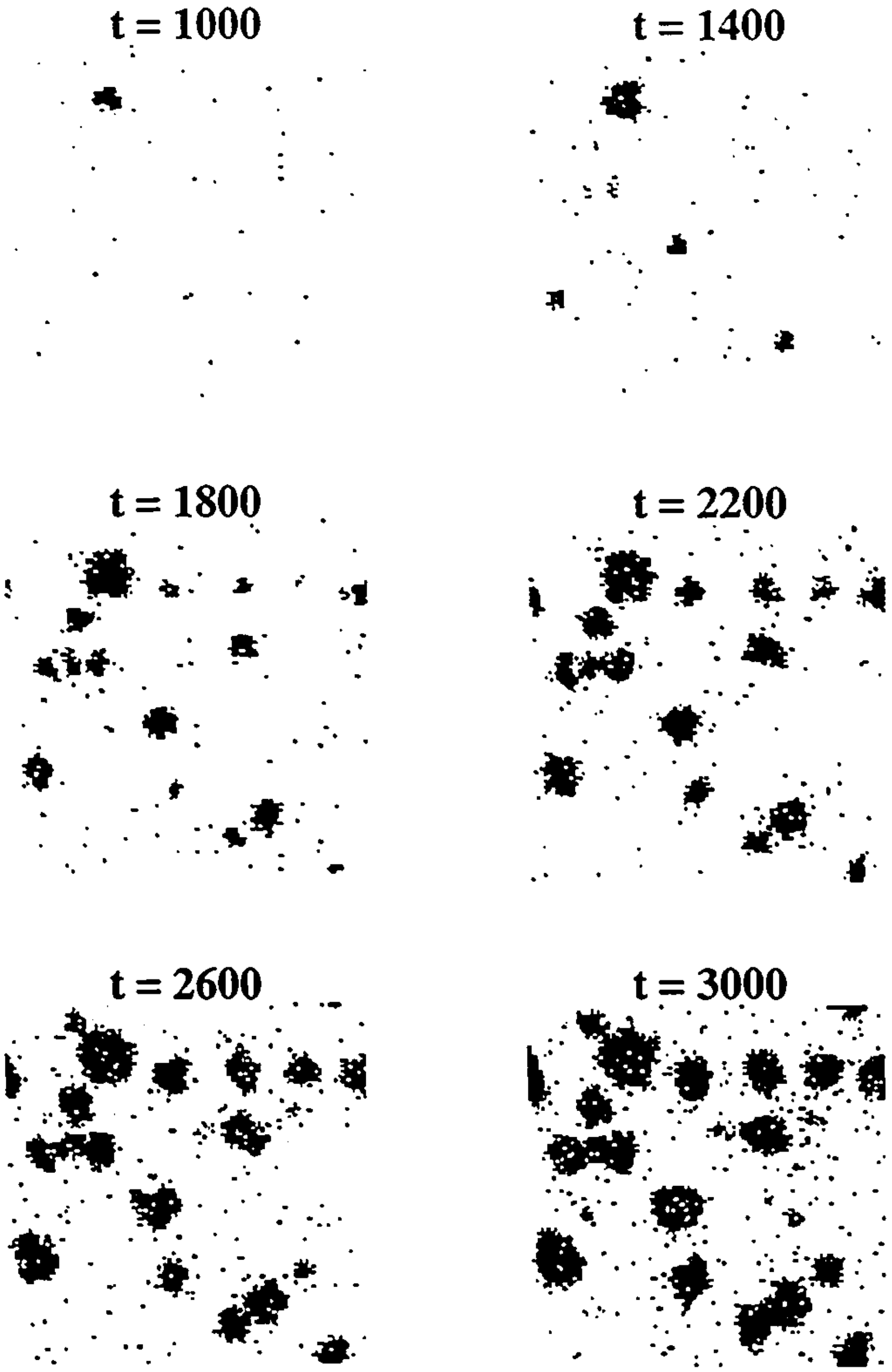

Figure 53: A time series showing lateral cuts at fixed height across the growing dendrites in a block system. The dark areas are the solid dendrite(s).

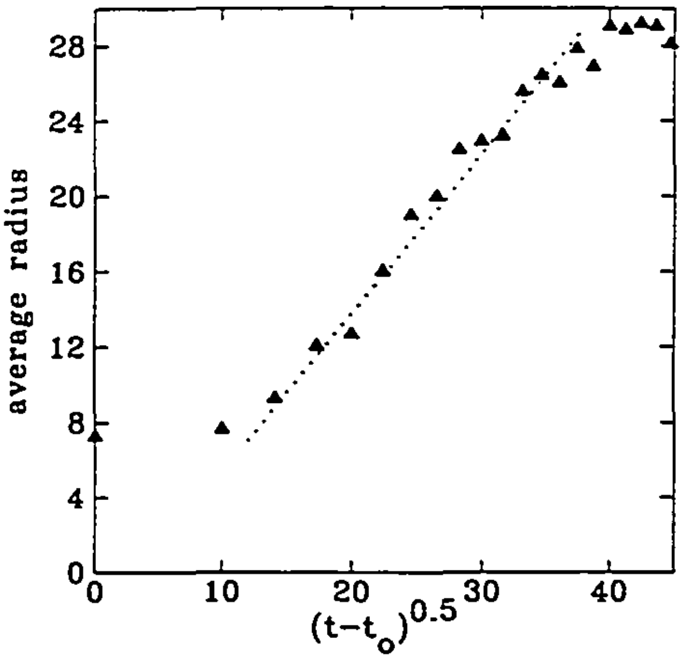

Figure 54: The radial structure factor from a *block* system. The time is rescaled as $(t - t_o)^{1/2}$ to show the $t^{1/2}$ growth. The initial time, $t_o = 1000MCS$, is the time at which dendrites first intersect the cutting plane at $N_z = 72$.

disappointing but not wholly unexpected.

The simulation geometries are not ideal for reproducing secondary instabilities. Due to the anisotropy of the crystal lattice, there are *preferred* directions of growth. In general, we find that $\{111\}$ interfaces become unstable more easily than $\{100\}$ interfaces. This is attributed to the finite roughening temperature on the $\{100\}$ interface ($T_R \simeq 0.54\ T_c$) which inhibits growth; as noted in Section 5.4, a faceted interface has a highly non-linear response to a driven force which is much weaker than a roughened interface. In most cases, the undercooled melt is set to a temperature $T < T_R$ and the moving interface experiences temperatures well below T_m. Consequently, the [111] direction is favoured over the [100] direction.

In the slab system, only one of the [111] directions is coplanar with the slab itself. The others pass obliquely through the narrowest dimension (see Figure 56).

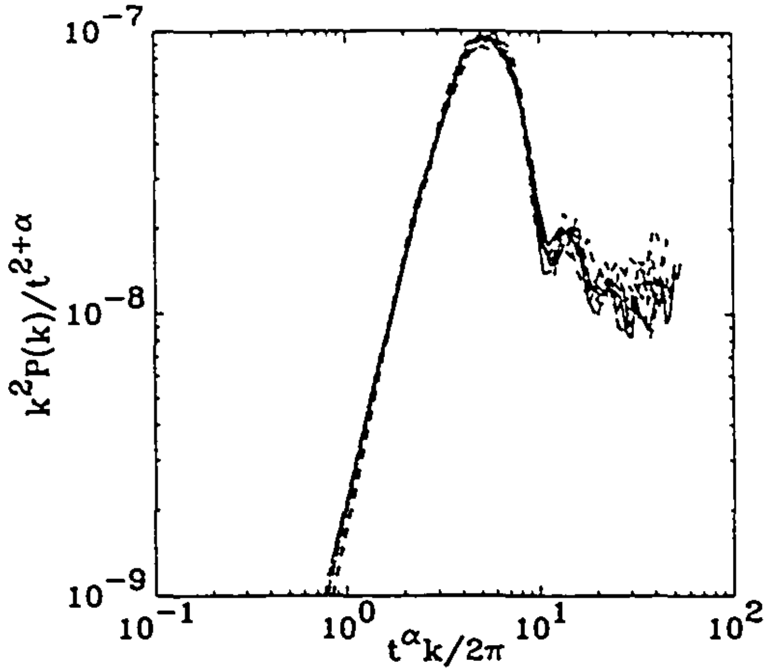

Figure 55: The power spectra from Figure 52 scaled by the ansatz $P(k,t) = t^{2+\alpha}\tilde{P}(kt^\alpha)$. The figure shows a plot of $k^2\tilde{P}$ against kt^α. Spectra are shown for t=3000, 2800, 2600, 2400, 2200, 2000, 1800 and 1600 MCS.

Consequently, with the primary instability growing along the coplanar [111] axis, secondary instabilities are driven by the thermal gradient in the less favourable [110] and [1$\bar{1}$0] directions. Although there is no finite roughening transition temperature for the {110} planes, the orientation is closer to the {100} planes and faceting effects become more pronounced. Perturbations observed on the sides of the dendrites are strongly damped and never become side-branches. On the other hand, tip-splitting has often been observed. This is curious since tip-splitting is usually associated with systems with no lattice anisotropy (Langer 1980). It may be that growth in other directions is so inhibited that it is easier to coarsen and split into two parallel fingers than to form side-branches. However, experimental results are not consistent with these results. Cummins *et al.* (1988; 1990) use a similarly slab-like geometry on succinonitrile which also has a cubic lattice structure. They have had no difficulty

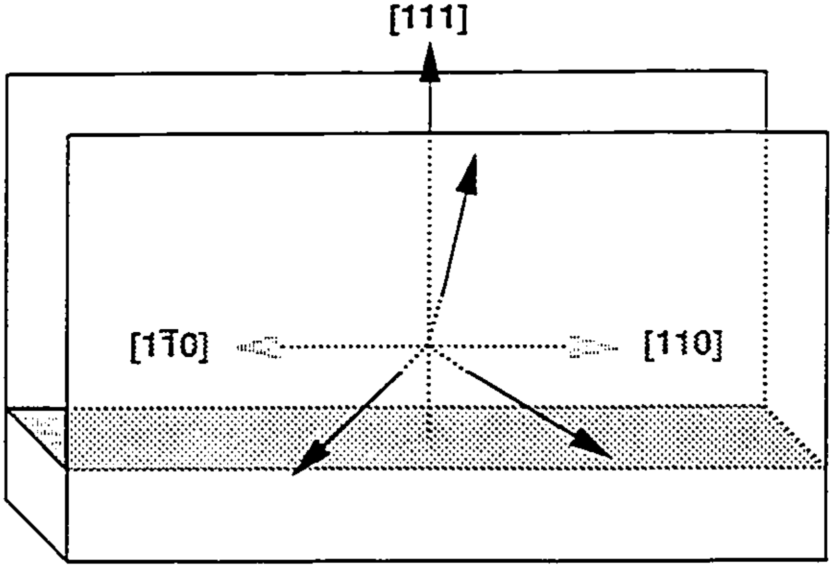

Figure 56: A rough diagram of the slab geometry with a {111} interface demonstrating the arrangement of the preferred directions of growth; secondary growth is inhibited by the sides. A similar but less severe problem is created in the block geometry due to the fact that the preferred directions are not perpendicular to the primary instability's sides.

producing side-branches in abundance. In fact, many of the most spectacular dendrite images with side-branches come from studies using succinonitrile (Glicksman 1984).

In the block geometry, there is another set of obstacles to side-branching. Although fully three dimensional, the [111] direction of the primary instability still creates problems; the two other preferred vectors $[\bar{1}11]$ and $[\bar{1}\bar{1}1]$ are not at right angles to it. A secondary instability growing along one of these directions would be oblique relative to its parent dendrite, either back towards the original interface or forwards along the parent (see Figure 56). This does not completely rule out side-branching as in the slab case; in fact, evidence suggests that secondary growths do appear but soon after they have extended away from the primary dendrite, they change direction and begin to grow along the same direction. In Figure 57, we show one of the clearest examples of this kind of behaviour; this system was the largest ever run at a size of $128 \times 128 \times 144$. We believe that besides having insufficient space and time to grow the secondary instabilities, this model may not behave in a manner typical of the

Figure 57: A cross-section from a *block* simulation of size 128 × 128 × 144 at steps t = 10000, 11500, 15000, 20000 and 25000 MCS. Note how the side-branch has grown sideways only far enough to free itself from the parent and then turned upwards. Arguably, this might be considered *tip-splitting*.

now-classic succinonitrile system (Figure 1) but rather in a less structured form like the salt mixture shown in Figure 7 a). What is certain is that an order of magnitude increase in computer speed and memory will be required to test this belief.

7.4 Thermal Fields

Since the attempts to reproduce full dendritic growth by simulation were only partially successful, we spend the remaining part of this final chapter describing our preliminary investigations of other lines of approach. First of these is the investigation of the thermal fields near the interfaces of our model, with the hope that we be able to confirm that the thermal diffusion process is being effectively simulated and possibly to shed additional light on the problem of the side-branching inhibition.

As described in Chapter 4, the local temperatures can be derived from the energy distribution of the demons by an appropriate averaging scheme. An analysis of the thermal fields associated with the instabilities will give us some additional insight into the processes at work. However, before attempting an analysis of the more complex geometry of late time dendritic growth, we shall check a simpler prediction from the linear stability analysis in Section 3.1. By choosing specific parameters for the simulation, the interface can be stabilized so that it moves forward but does not demonstrate any growth modes. This is done by reducing the latent heat, increasing the diffusion constant or decreasing the system size: Recall from (47) and (51) that the wavelength of maximum instability (64) is defined by $\lambda_{max} \propto \sqrt{\ell d_o}$; if λ_{max} is increased so that it exceeds the size of the system, the instability is effectively inhibited. The undercooling is then chosen so that the latent heat produced exactly heats the liquid phase to T_m. The resulting interface remains planar as it moves forward at a constant velocity. The planar symmetry of the interface then simplifies measurement of the temperature gradient and makes possible a comparison with the solutions for the thermal field (53).

Figure 58 shows the thermal gradient in the $\hat{z}$ direction from a system of size $72 \times 72 \times 144$ with $T_m = 0.7\ T_c$ and $T_u = 0.3\ T_c$; each layer of demons parallel to the interface was averaged to find the demon energy and subsequently the local temperature $T(z)$. The thermal gradient is obviously in good agreement with its analytic counterpart shown in Figure 12; the temperature falls from almost T_m at the interface to T_u at $z \to \infty$ like e^{-Az} where $A \simeq 2/\ell$ as demonstrated in the lower plot. The only discrepancy is the slight dip in temperature in the solid side of the interface $z \leq 0.22$; this is likely due to the finite curvature at the roughened interface (see Figure 12). Measuring the slope of $\ln(T - T_u)$, we obtain a value for the diffusion length of $\ell \simeq 45\ a$. When ℓ is then plugged back into its definition, $\ell \equiv 2D/v$, with

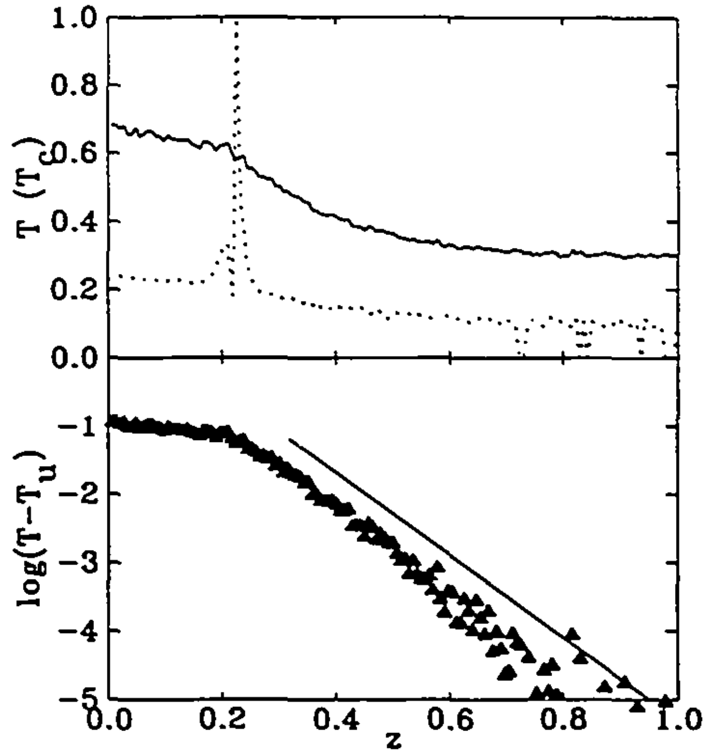

Figure 58: The thermal gradient of a stabilized, moving planar interface is shown in the upper plot: The solid line is the temperature based upon the average demon energy in the slice at height z perpendicular to the interface. The dotted line is based on the mean spin value in each slice and is the best measure of the interface position. The points in the lower plot are the logarithm of the temperature less the undercooling at infinity; the straight line is provided to aid the eye.

the measured interface velocity $v \sim 0.030\ a/MCS$, we find $D \sim 0.65 \pm 0.07$; for a single simulation trial, this is reasonably consistent with $D = 0.8\bar{3}$ which was set as a system parameter (see discussion leading to (98)).

Satisfied that the thermal diffusion field is consistent with its analytic description, we shall now examine the results from some typical dendrite simulations. Due to the arbitrary surface geometry of a dendrite, the simple planar averaging used above cannot be employed. Instead, thermal imaging is done by isolating a cross-section of the thermal field and applying a simple 3D Gaussian spatial-averaging scheme to each site;

$$\mathcal{E}(i,j,k) = \sum_{di,dj,dk=-n}^{n} e^{-s^2/\lambda^2}\epsilon(i+di, j+dj, k+dk)$$

where di, dj, dk are integers varying over the site's neighbours, $s^2 = di^2 + dj^2 + dk^2$ is the distance between sites and λ is the weighting factor. The range of averaging is $n = 2$ and thus the average is over the nearest 124 neighbours (ie. a cube of $5 \times 5 \times 5$ centered on each site) with no time averaging. This is adequate to identify thermal gradients on length scales beyond three lattice spacings. The resulting image shows the averaged temperatures using a pseudo-color scheme, representing from cold to hot by blue to red (or by a grey scale from black to white).

Figure 59 shows a collection of thermal fields: Each demonstrates some typical growth behaviour based upon a specific choice of system parameters (latent heat, undercooling, melting temperature). Fluctuations in the temperature on short length scales are due to the discrete nature of demon energy levels (spin flips are of order $\Delta\epsilon \simeq 2J$) and the limited statistics of the demon lattice. The solid-liquid interface (derived from the spin lattice) is drawn over the thermal field for reference.

Visual inspection identifies the presence of thermal gradients near the interfaces. As expected, the gradient between the liquid and bulk phases is strongest near the growing dendrite tips where the velocity is greatest. It is weaker along the nearly-

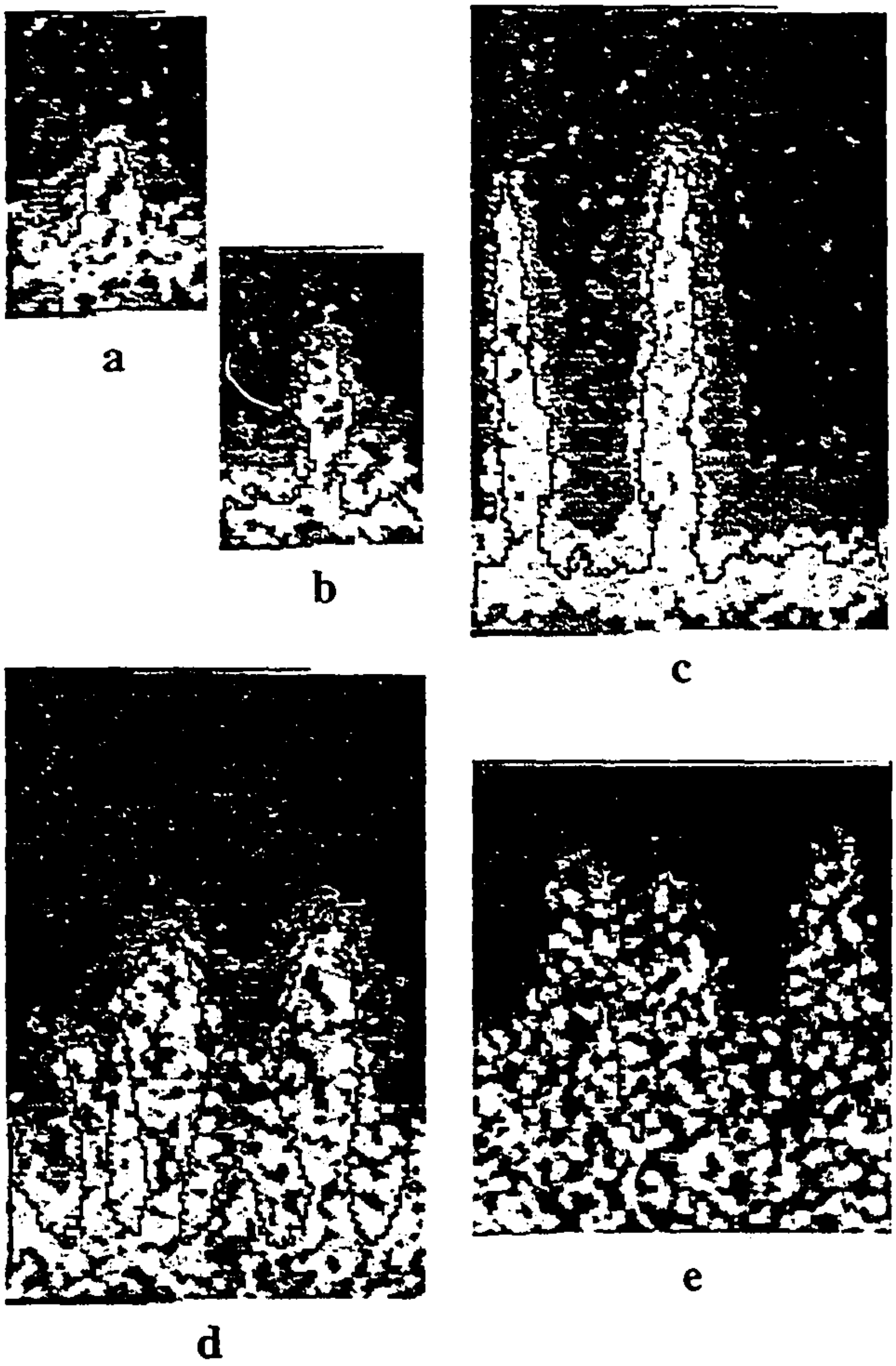

Figure 59: Representative thermal fields derived from an analysis of cross-sectional slices of demon lattices. Figures a) and b) are from *block* systems while c), d) and e) are from *slab* systems. The dark outline is the interface derived from the spin lattice. The lighter regions (on the bottom) are associated with the solid; above is the liquid. Temperature is shown as dark for cold and light for hot. The graininess of the temperature is related to the limited statistics of the demon distribution. Note that d) is from the same simulation trial as shown in Figure 46.

stationary initial interface. It is also evident that much of the liquid phase around the base of the dendrites has reached or exceeded the coexistence temperature. Indeed, where multiple dendrites appear, the region between them tends to fill with the excess latent heat produced by the moving interface. Recall that this excess is described by

$$\Lambda = C(T_m - T_u)/\mathcal{L}$$

where $\Lambda \equiv 1$ when the amount of latent heat released is identical to that required to heat the supercooled liquid phase to T_m. In general, Λ is much smaller than unity. As one of the dendrites begins to pull ahead of the others, it retards their growth by leaving its excess latent heat in their path, providing a natural selection mechanism (see Figure 46).

To explore more carefully the role of various system parameters in the instability, we examine a collection of more-closely related systems. Figure 60 shows a $72 \times 72 \times 144$ system at differing levels of undercooling ΔT, melting temperature T_m, latent heat $\mathcal{L}$, and diffusion constant D; Table 7.4 gives the specific values. The first system a) is considered representative with $T_m = 0.7\ T_c$, $\Delta T = 0.4\ T_c$, $\mathcal{L} = 5.23\ J$ and $D = 0.\bar{3}$, showing moderate surface roughening, a rounded tip and a typical growth rate. Both b) and c) have a higher T_m which results in greater roughening, faster growth and coarsening; in addition, c) has a slightly greater undercooling and thus is fastest. System d) has a greater undercooling than a) and is growing faster as a result; lowering T_m in e) slows the growth and reduces the roughness. Subsequently lowering the diffusion rate in f) slows the growth even more. If the latent heat is increased very slightly as in g), the growth rate jumps dramatically; this suggests that the ratio Λ in f) was near some critical limit. Increasing $\mathcal{L}$ significantly (nearly double) in h) slows growth again as there is then an over-abundance of released heat. The result is that the growth is much narrower and tapered; common to many low T_m trials, the tip of h) shows distinct faceting due to the roughening transition (see

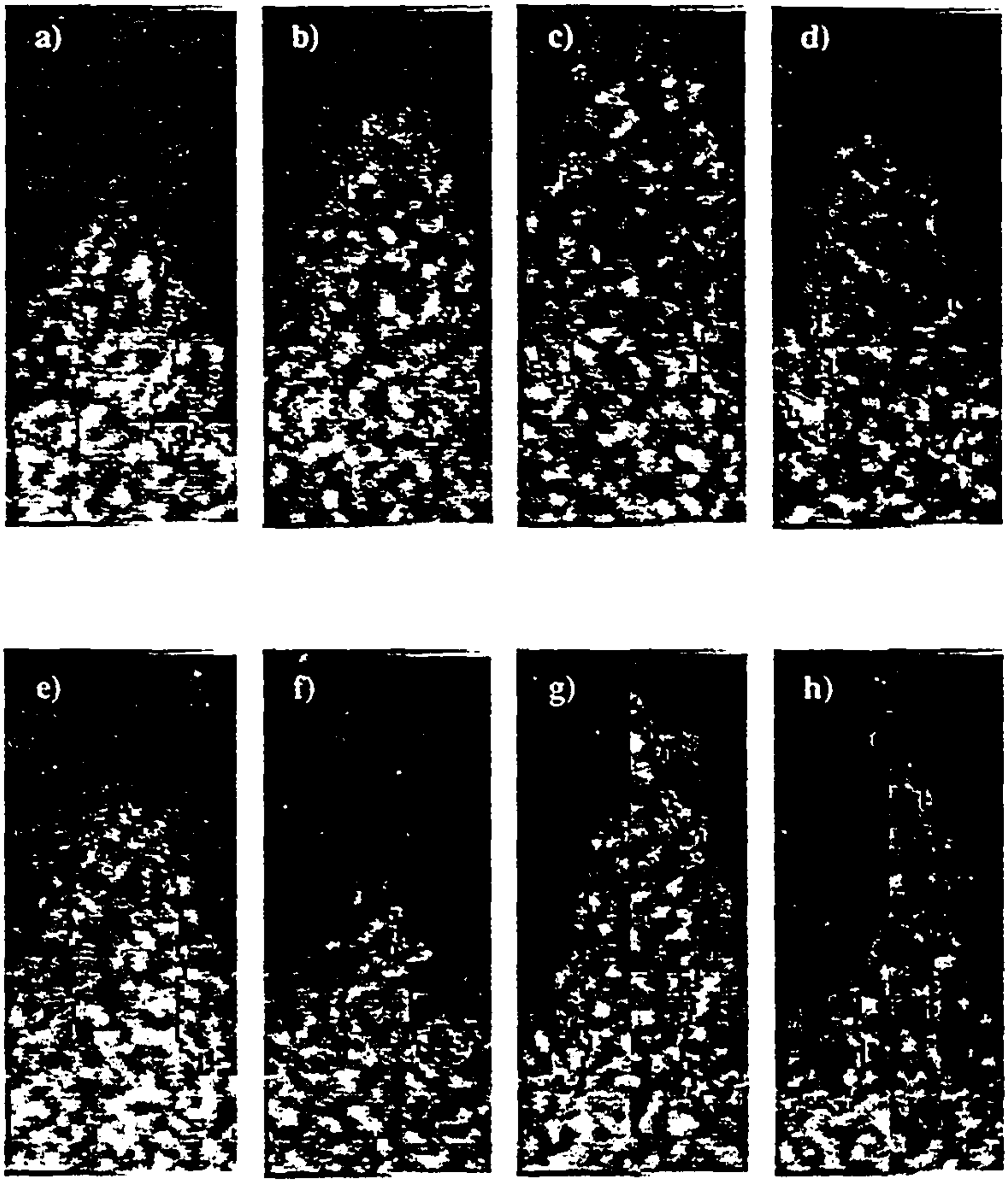

Figure 60: The thermal fields from closely related systems of size 72 × 72 × 144: Each field demonstrates the consequence of varying a system parameter; see Table 7.4 for the specific values. Field a) represents the typical growth behaviour. See the text for an analysis. Temperature is shown as dark for cold and light for hot. The split images in g) and h) show early and late times for comparison.

Section 7.5).

In general, results are entirely consistent with the description of the Mullins-Sekerka instability in terms of the thermal diffusion, as presented in Chapter 3, and the role of interface fluctuations. Specifically, we can see that the thermal diffusion field is directly coupled to the growth of the dendrites; the lack and over-abundance of latent heat tends to inhibit growth; higher melting temperatures roughen and accelerate the interface and lower melting temperatures slow it, introducing faceting at the tip attributed to the dynamic roughening transition; reduced diffusion rates limit growth. Also apparent, although not predicted by linear stability, is the relationship between the scaled undercooling Λ and the coarsening of the dendrite; larger Λ corresponds to enhanced coarsening even though the thermal gradients near the interface appear to be comparable. This suggests an area for further study.

	T_m	ΔT	$\mathcal{L}$	D	Λ	d_o	ℓ
a)	0.7	0.4	4.7	$0.\bar{3}$	0.35	0.18	26
b)	0.8	0.4	3.3	$0.\bar{3}$	0.61	0.51	19
c)	0.8	0.5	3.3	$0.\bar{3}$	0.76	0.49	13
d)	0.7	0.5	4.0	$0.\bar{3}$	0.47	0.22	18
e)	0.65	0.45	3.8	$0.\bar{3}$	0.35	0.18	42
f)	0.65	0.45	3.8	$0.\bar{1}$	0.35	0.18	37
g)	0.65	0.45	4.1	$0.\bar{1}$	$0.\bar{3}$	0.15	12
h)	0.65	0.45	5.8	$0.\bar{1}$	0.29	0.096	19

Table 1: The table entries correspond to the thermal fields in Figure 60; changes in each of the parameters, coexistence temperature T_m, undercooling ΔT, latent heat $\mathcal{L}$ and diffusion constant D, produce behavioural changes in the instability as described in the text. The units of T_m and ΔT are in T_c of the unmodified Ising model; $\mathcal{L}$ is in units of J; D is in square lattice spacings per Monte Carlo step. The other parameters, the scaled undercooling Λ, the capillary length d_o and the thermal diffusion length ℓ, are calculated from expressions derived in Chapter 3; Λ is dimensionless; d_o and ℓ are in lattice spacings. Note that ℓ depends on the tip velocity which is measured but not shown here.

7.5 Faceted Dendrites

The second direction in which we began preliminary investigations is the special case of dendritic growth with faceted tips. Often, crystalline forms characteristic of real dendritic growth (such as the snowflake in Figure 1) correspond to growth taking place below the roughening transition. We might hope that the model interfaces below $T_R^{\{100\}}$ will show behaviour resembling that of real, faceted crystals. Due the nature of dynamic roughening, there are difficulties in exploring this behaviour; recall that faceted interfaces have a very weak response to driving forces and move quite slowly (see Section 5.4). Moreover, lower temperatures involve reduced rates of spin dynamics, further slowing the interface. Subsequently very long runs are required for small undercooling and low temperatures. However we will be able to convincingly demonstrate this behaviour in our simulations.

As mentioned, the dynamic roughening transition plays a subtle role in the formation of dendrites. For example, it inhibits instabilities on certain planes where the local interface temperature is below the roughening temperature T_R (eg. the {100} faces) resulting in the phenomenon of *preferred* directions of growth. A case in point, the growth of the arms of a snowflake radially out from the hexagonal unit cell is much faster than perpendicularly out from the basal plane; this is why the classic snowflake shape is flat. In our simple cubic crystal simulation lattice, it has been observed that this effect is at least partly responsible for the atypical side-branching (see Section 7.3).

In Section 5.4, it was observed that the faceted interface phase continued to exist despite the presence of a driving force, at least, up to a critical limit. When the phase coexistence temperature is very low, the interface can be exposed to relatively large driving forces, exhibit instability behaviour and still be faceted. This has been observed experimentally (Maurer, Bouissou and Perrin 1989) in the growth of NH_4Br

crystals from a supersaturated solution; Figure 61 shows several of these growths at different velocities. Note that the faceting is restricted to the tip of the dendrite

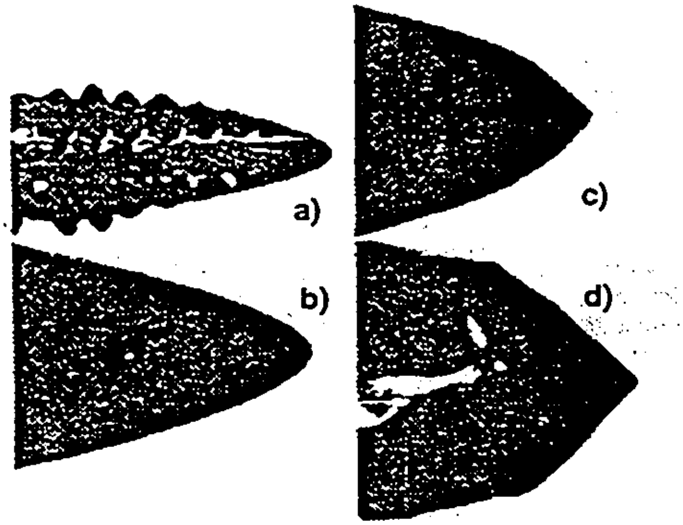

Figure 61: Experimental growth shapes of NH_4Br crystals at different velocities, a) $v = 0.43 \mu m/s$; b) $v = 0.042 \mu m/s$; c) $v = 0.015 \mu m/s$; and d) very close to equilibrium. These images are from work by J. Maurer *et al.* (1989).

where the thermal gradient, and subsequently interface undercooling, is greatest. Similar to the observations made of the stable planar interface, a *dynamic* roughening transition is observed such that the faceting at the dendrite tip gradually disappears with increasing velocity (and thus with increasing driving force).

Comparable results have been observed in some of our simulation trials. Using a coexistence temperature set to the equilibrium roughening temperature $T_m \sim T_R = 0.54\ T_c$ and a relatively strong undercooling, $\Delta T \simeq 0.40\ T_c$, single dendritic growths with faceted tips have been produced; Figure 62 shows a typical result. The tip velocity in this case is measured to be constant at $v = 6.4$ lattice units per 1000 MCS. By varying the undercooled temperature, the driving force at the tip can be changed. For the same system, we varied the undercooling $T_u \in [0.0, 0.2]\ T_c$ and observed the steady-state velocity of the tip as shown in Figure 63. Although the data is based on only one trial per point, there is a clear transition in the growth response near

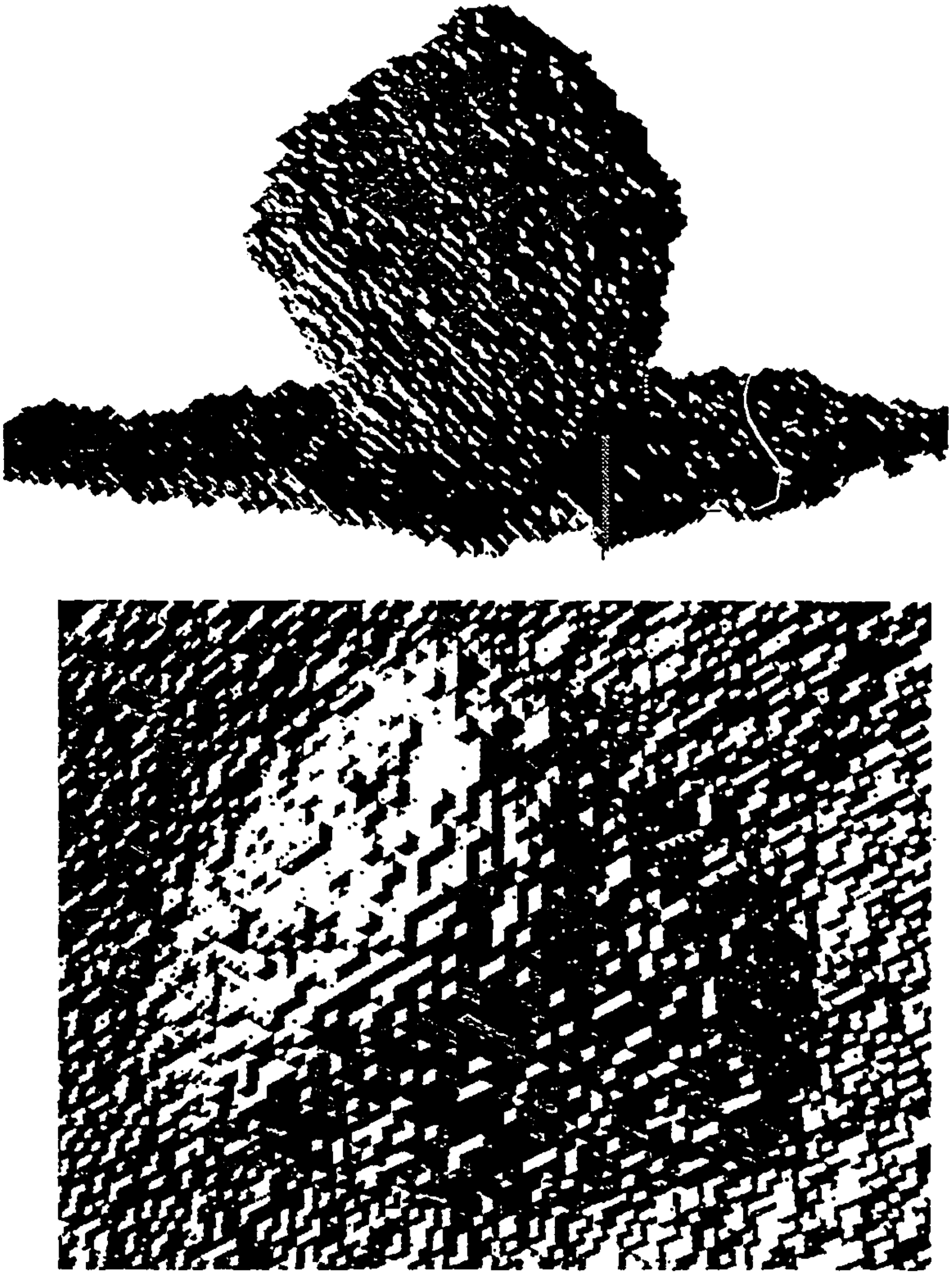

Figure 62: Two views of a simulation of a faceted dendrite; the lower image shows an *aerial* view of the tip, highlighting the cubic facets.

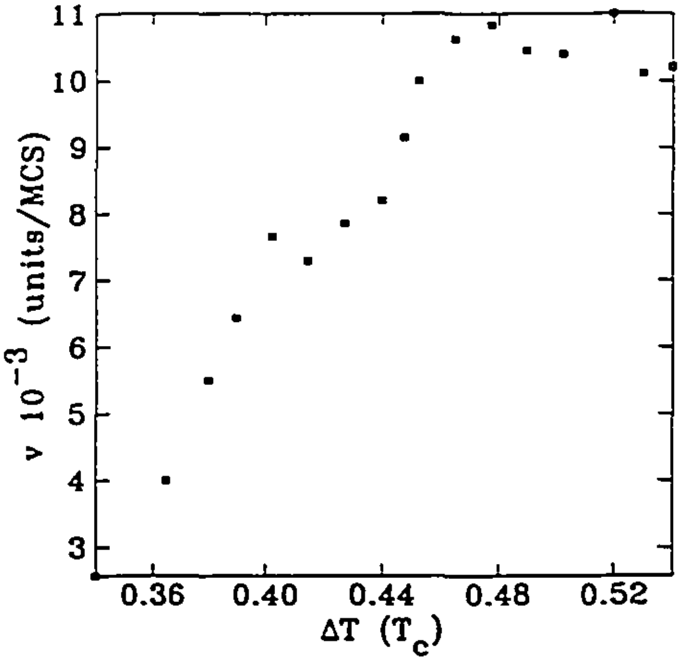

Figure 63: The growth response of a dendrite at temperatures below the equilibrium roughening temperature T_R for a given undercooling. Visual inspection of the dendrite tip at $\Delta T < 0.48\ T_c$ shows that it is faceted. Figure 62 shows the dendrite for $\Delta T = 0.40\ T_c$.

$\Delta T \sim 0.48\ T_c$; error bars are estimated at 10-15%. Due to the strongly non-linear response of the faceted tip, the velocites for the smallest undercooling are particularly low and difficult to measure accurately. However, the trend is unmistakable and completely consistent with our expectations. We fully expect to be able to perform a complete study of this behaviour in the future, making direct contact with existing results (Maurer, Bouissou and Perrin 1989) and analytic descriptions (Ben Amar and Pomeau 1988).

8 Conclusions

We have examined the behaviour of crystal interfaces using Monte Carlo simulation on a simple cubic Ising model of spins. The interfaces were simulated under a variety of conditions, highlighting several distinct surface phenomena. In particular, the roughening transition of equilibrium and dynamic interfaces and the Mullins-Sekerka instability at early times (linear regime) and late times (non-linear regime) were studied. In almost all cases, the results represented the first reported attempts at simulating these processes in three dimensions.

A planar {100} interface at equilibrium was first shown to demonstrate the well-known *equilibrium roughening transition* with changing temperature. The results of our simulations were compared favourably to previous studies and to current theoretical descriptions. An alternate approach to analyzing a faceted interface was presented; it was established as a greatly improved method of identifying the transition. This technique was then applied to the surface of a metastable bulk inclusion (or droplet) to measure its roughening transition behaviour. It was noted that the droplet required an external driving force to enforce metastability and subsequently that the roughening behaviour was modified. The modifications, a depression of the roughening temperature and a broadening of the transition region, were found to be in good agreement with theoretical predictions for the *dynamic roughening transition*. Comparisons with predictions based on the droplet shape were also found to be consistent although less clear.

Dynamic studies of these interfaces were then carried out. First, the balancing force on the metastable droplet was removed and it was observed to demonstrate behaviour resembling a roughening transition, passing quickly from a faceted to roughened state, although neither temperature nor driving force was changed. This was found to be a natural consequence of two distinct evaporation processes reducing the surface energy of the droplet at disparate rates. Next, the planar interface was observed in the presence of a weak thermal gradient. Again using our analytic technique, we showed the presence of a *dynamic roughening transition* as a function of undercooling (driving force). Although we were unable to compare the data directly with theoretical predictions, we did observe behaviour which was consistent with analytic descriptions.

Turning to the *Mullins-Sekerka instability*, we first undertook a test of the predictions of linear stability analysis, which are considered fundamental to this phenomenon at early times. In the light of technological limitations, we chose to use a two-dimensional version of our code. The linear analysis makes several very specific predictions for the linear regime growth of planar and circular interfaces which have never before been directly confirmed in either simulation or experiment. In the planar case, a special long-range interaction was used to extend the linear regime; the dispersion relation defining the growth modes of the interface was then measured and found to be consistent with the predictions. Despite the large ensemble of data used, noise was still significant, underlining the difficulty in extracting useful information. In the circular case, the stability radius of the growing disk was measured and shown to be in good agreement with theory, using two independent techniques. In concert, these results are very convincing validation of the linear stability analysis. They also support the use of our model for the simulation of dynamic processes.

Finally, we examined the *Mullins-Sekerka instability* at late times when the growth is non-linear and geometrically complex. Based on experience and on the limitations of computer hardware, we chose to examine two specific configurations of the {111} interface: First, we studied the quasi-two dimensional *slab* system which has one of the interfacial dimensions very small compared to the other; this permits relatively large, flat dendritic growths. Second, we studied the *block* system which is fully three dimensional but limits the size of the growths which are possible.

Both types of growth were characterized by tip velocity, surface area and power spectra and shown to be consistent with experimental observations and analytic results. The two systems were distinguished by the absence of coarsening in the *slab* growths, similar to previous simulation studies performed on true 2D systems. In neither case did we observe side-branching, the production of secondary instabilities on the sides of the growing dendrites; this feature is routinely observed in experiments. Noting the appearance of proto-branching in certain cases, we surmised that complications related to the crystal structure inhibit the formation of side-branches.

Turning to the analysis of the growths in terms of the associated thermal fields, we demonstrated the physically correct behaviour of the thermal diffusion mechanism again using predictions from the linear stability analysis. We then directly examined the appearance of a variety of growth shapes and commented on the effect of various system parameters on the instability. Lastly, we presented the results from a preliminary study on a special class of dendrite which has a faceted tip. Making direct comparison with existing experimental studies, we showed a comparable growth shape in low temperature simulations and demonstrated a transition behaviour in the growth response to changing driving force. This behaviour is consistent with the dynamic roughening transition observed and discussed in an earlier Section. Indeed, this appears to be the unique cross-over case where both the Mullins-Sekerka instability and the roughening transition are observable simultaneously.

The work presented here has established the viability of studying crystal interfaces with simulation in both equilibrium and dynamic contexts in three dimensions. We have reproduced accepted behaviour as well as produced unique results and provided a basis for interpreting them. We have laid the foundations for further studies of crystal interface problems, in greater detail and in new contexts. We envision the use of other crystal structures such as face-centered cubic, body-centred cubic and hexagonal close-packed to study their multiple roughening transitions and unique instability patterns as observed experimentally; simple cubic crystals are relatively rare in nature and most experimental results available for direct comparison involve materials with other structures. We also hope that they might provide the key to the side-branching phenomenon in the Mullins-Sekerka instability. In addition, more work needs to be done on the instability in the linear regime, both in terms of improving the statistics in two dimensions and extending the study to three dimensions. Several other results were left relatively unexplored including details of the dynamic roughening transition in our model, growth and evaporation processes in crystal droplets and the roughening behaviour of facetted dendrites. With constant and ongoing advances in computer hardware, we expect many new and beneficial results to be derived from future simulation studies of crystal interfaces.

Appendices

A.1 Crystal Plane Notation and Lattice Geometries

The simple cubic (SC) crystal structure is the simplest crystal in terms of its unit cell and indexing. The position and orientation of a crystal plane is denoted by an orthogonal set of three vectors which are, by convention, defined by the unit cell of the crystal. The cubic unit cell is a cube defined by the Cartesian vectors $\hat{x}$, $\hat{y}$ and $\hat{z}$ of unit length (see Figure 64). Crystallographic planes are then referred to in terms of (hkl) where h, j and l are found by the following recipe:

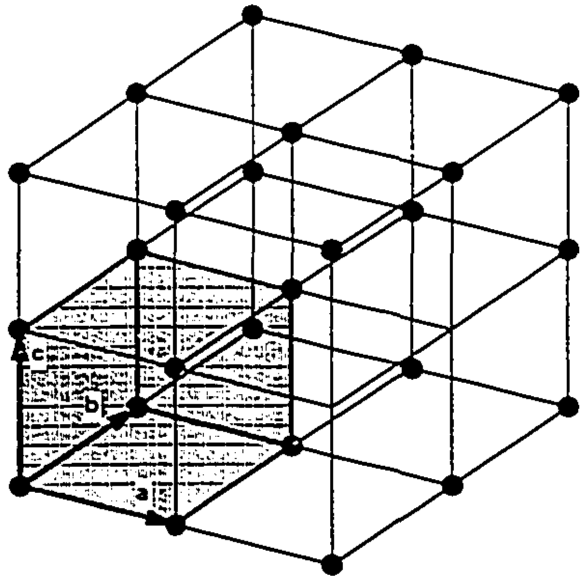

Figure 64: A schematic diagram of the simple cubic unit cell.

1) Starting from an arbitrary origin on a crystal lattice site, find the integer intercepts a, b and c along $\hat{x}$, $\hat{y}$ and $\hat{z}$ of the plane

2) Take the reciprocals of a, b and c and find the smallest integers h, j and l which preserve their relative ratios.

Ie. for $(a,b,c) = (3,2,4)$, change to $(1/a, 1/b, 1/c) = (\frac{1}{3}, \frac{1}{2}, \frac{1}{4})$ and find $(hkl) = (463)$. Negative numbers are denoted $-h \rightarrow \bar{h}$. This is the Miller index.

The primary *faces* of a cube are thus (100), (010) and (001) with the opposing faces denoted ($\bar{1}00$), ($0\bar{1}0$) and ($00\bar{1}$). Since they are symmetric with respect to rotation, they are referred to as a set as {100}, the curly brackets implying the equivalence. The three planes which each cut diagonally through three adjacent cube faces are the {111} planes. The *directions* $[hkl]$ are perpendicular to the planes (hkl); note that this is true for the simple cubic crystal but not necessarily so for other structures. For more details on crystal indexing, see Nicholas (1965).

The cubic Ising lattice is identical to the simple cubic crystal lattice and is usually implemented in a manner such that the sites are accessed according to the (a, b, c) convention. However, to reduce the complications of plane orientation issues such as the shape of the simulation system, the simple cubic crystal was mapped onto the simulation lattice such that the crystal interface always corresponds to the lattice (001) interface, no matter the crystal orientation. This was done by uniquely coding the definition of the lattice nearest neighbours for each crystal orientation.

In all cases, the algorithm uses a virtual lattice which is regular and cubic with $N_x \times N_y \times N_z$ sites; the choice of *nearest neighbours* and spin bond strengths determines which physical crystal structure the algorithm emulates. The initial interface is always parallel to the X-Y plane of the virtual lattice. The *sides* of the system are always periodic; the *ends* are pinned.

In the case where the nearest neighbours of a site at a, b, c are defined as the adjacent sites along the Cartesian axes (ie. $a \pm 1, b \pm 1, c \pm 1$) and bond strengths are equal and identical to J of the Hamiltonian, the system represents the SC structure and the interface corresponds to the {100} plane. Figure 65 demonstrates the basic lattice definition.

If the nearest neighbours are specially chosen triplets in the X-Y planes above and below the site (ie. $a_1, b_1, c-1$; $a_2, b_2, c-1$; $a_3, b_3, c-1$; $a_4, b_4, c+1$; $a_5, b_5, c+1$;

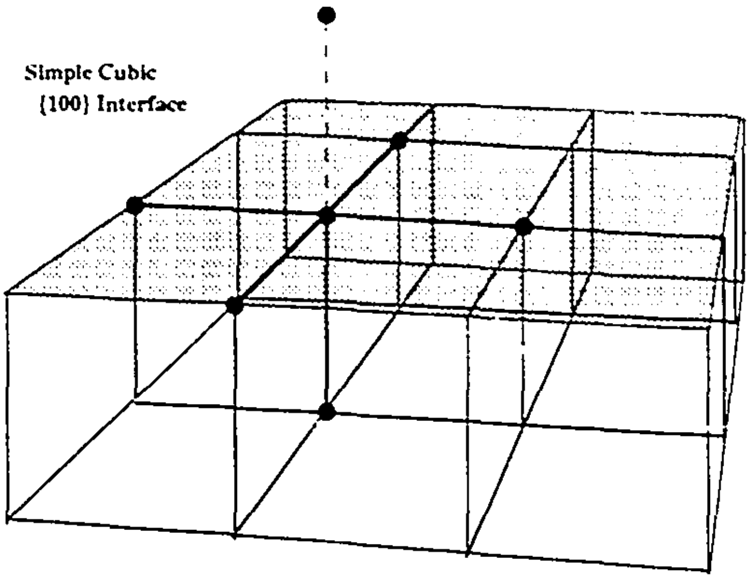

Figure 65: A schematic diagram of the {100} interface. The bonds to the neighbours of one interface site are highlighted.

$a_6, b_6, c+1$) and bond strengths are equal, the lattice represents the SC structure oriented with the {111} plane parallel to the X-Y plane. Each X-Y plane c defines the triplet neighbours for a site differently according to its designation as one of the three distinct laterally displaced SC {111} planes; the SC {111} structure is constructed by stacking these X-Y planes cyclically (ie. 1,2,3,1,2,3,1,...etc.). Figure 66 shows how the neighbours are defined on the cubic lattice.

Other crystal structures are immediately accessible using this approach such as hexgonal close-packed (HCP) and face-centered cubic (FCC). As well, the bond strengths can be varied to produce other non-rotationally symmetric variations.

A.2 Critical Droplet Radius

Consider the free energy of a spherical droplet of radius R;

$$E_F = 4\pi R^2\gamma - \frac{4}{3}\pi R^3 \triangle E_b$$

where $\triangle E_b$ is the bulk free energy difference and γ is the surface tension. The first

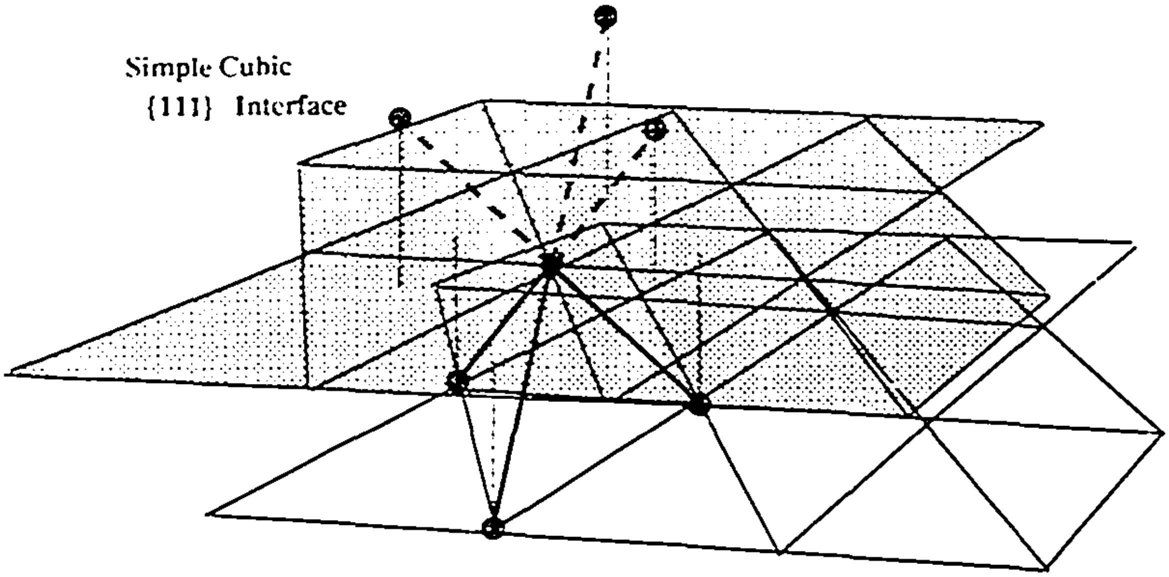

Figure 66: A schematic diagram of the {111} interface. The bonds to the neighbours of one interface site are highlighted.

term is the capillary contribution and scales with γ as the surface area. The second term is the bulk term and scales as the volume; it is assumed negative (ie. the *solid* has a lower bulk energy than the *liquid* melt) as there is no finite critical radius otherwise.

At the metastable point where $dE_F/dR = 0$, the droplet does not feel any force and thus does not grow or decay. The critical radius is thus defined to be

$$R^* = \frac{2\gamma}{\Delta E_b}.$$

At $R > R^*$, the droplet will tend to grow; at $R < R^*$, the droplet will tend to shrink. When $\Delta E_b \equiv 0$ (ie. at coexistence), $R^* = \infty$ and all sizes of droplets will shrink.

In two dimensions, the analysis is almost identical. The free energy of a disk is

$$E_F = 2\pi R\gamma - \pi R^2 \Delta E_b.$$

Here of course, γ is surface energy per unit length and the capillary term scales as the circumference; ΔE_b is the bulk free energy difference per unit area and the bulk term scales as the area. This leads to critical radius which only differs from the 3D R^* by a factor of 2;

$$R^* = \frac{\gamma}{\Delta E_b}.$$

Some analyses are performed with slightly different forms of the free energies. The *capillary length* is length scale which assigned to the surface free energy; it is defined to be

$$d_o = \frac{\gamma T_m C}{\mathcal{L}^2}$$

where T_m is the coexistence temperature of the system (which has a first-order transition) and $\mathcal{L}$ is the requisite latent heat. The bulk free energy of each phase $m_\pm \sim \pm 1$ is

$$E_b(m_\pm) = \epsilon(m_\pm) - s(m_\pm)T$$

where ϵ and s are the meanfield average spin energy and entropy density, equations (85) and (87) respectively. To first order $m_+ \simeq -m_- \sim 1$ near coexistence and thus the bulk free energy is $\Delta E_b \simeq \ln(\delta)(T - T_m)$ and we can express the critical radius as

$$R^*_{2D} = \frac{d_o}{\Lambda} \qquad R^*_{3D} = \frac{2d_o}{\Lambda}$$

A.3 Curvature of a Discrete Lattice

Here we derive an expression for the mean curvature $\bar{\kappa}$ of a discrete interface, and relate this to the mean facet area $\langle A \rangle$ for $T > T_R$. If the interface is at thermodynamic equilibrium and is single-valued $h(\mathbf{x})$, then the Fourier spectrum of modes has the form (Grant 1988)

$$\langle|\tilde{h}(\mathbf{q})|^2\rangle = \langle|\mathcal{F}(h(\mathbf{x}))|^2\rangle \propto \frac{T}{\gamma(T)q^2}$$

where γ is the surface tension and $\mathcal{F}$ signifies a Fourier transform

$$\bar{h}(\mathbf{q}) \equiv \mathcal{F}(h(\mathbf{x})) = \int d\mathbf{x}\, e^{i\mathbf{q}\cdot\mathbf{x}}\, h(\mathbf{x}).$$

When the local curvature κ is small ($\nabla^2 h \ll 1$) then

$$\begin{aligned}
\bar{\kappa}^2 = \langle\kappa^2\rangle \cong \langle(\nabla^2 h)^2\rangle &= \mathcal{F}^{-1}(\langle|q^2\bar{h}(\mathbf{q})|^2\rangle) \\
&= \int_{2\pi/L}^{2\pi/a} d\mathbf{q}\; q^4\langle\bar{h}(\mathbf{q})\bar{h}(\mathbf{q})^*\rangle \\
&\approx \frac{T}{3}\left(\frac{2\pi}{a}\right)^3 \qquad (L \gg a) \qquad (123)
\end{aligned}$$

so that

$$\bar{\kappa} \propto \sqrt{T}. \qquad (124)$$

To relate $\bar{\kappa}$ to the area of the local microfacet A, we show in Figure 67 the relationship of the interface to the underlying lattice with unit vector a. We choose a micro-facet whose center is approximately contingent with the apex of the curved interface, and define its size ℓ to be the solution of the expression

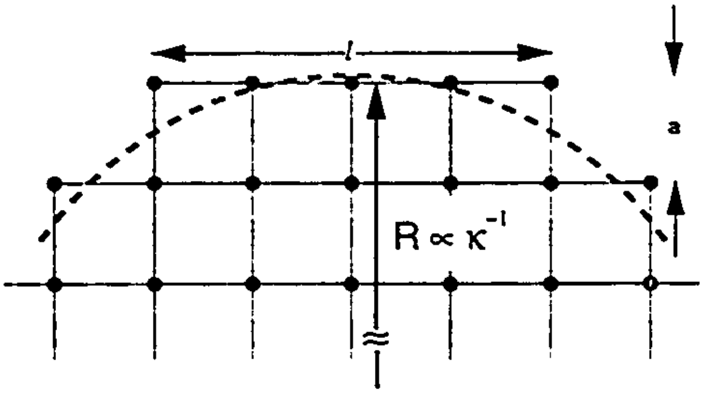

Figure 67: The discrete Ising lattice represents a curved interface with a stepped planar surface of comparable variation in height. Consequently, even a fully roughened surface can be described in terms of its *micro-facet* distribution. It can be shown that an interface of constant curvature κ will have a facet of size $l = \sqrt{8a/\kappa}$ where a is the unit lattice spacing.

$$\Delta h = h(\mathbf{x}) - h(\mathbf{x}_0) = \frac{1}{2}\kappa x^2 \equiv a$$

The distance from edge to edge is therefore

$$\ell = 2\|\mathbf{x} - \mathbf{x}_0\| = 2\sqrt{2a/\kappa}$$

where $\triangle h$ is assumed to be one lattice constant a. The micro-facet area is then

$$A(\kappa) = \ell(\kappa)^2 = 8a/\kappa. \tag{125}$$

so that, using (124), the mean micro-facet area behaves like

$$A(T) \propto T^{-1/2} \qquad T > T_R$$

A.4 Corrected Micro-Facet Quantities

The micro-facet population on a reference plane below the roughening temperature T_R is described by the Boltzmann-like probability function

$$P_f(\ell, T) = \Omega e^{-E(\ell)/k_B T}$$

where $E(\ell)$ is the energy required to create a micro-facet of size ℓ. Units are defined such that the Boltzmann constant k_B is unity and it is subsequently dropped from use. The prefactor Ω is defined so that

$$\sum_{\ell} P_f(\ell, T) = 1 \tag{126}$$

where the sum is over all sizes of ℓ in units of the lattice spacing a. Consistent with a cubic lattice at low temperatures, the typical micro-facet is assumed to be a square of thickness a and sides $\ell \times \ell$. The micro-facet energy is then

$$E_f(\ell) = 4\ell E_s(T) - a\ell^2 \triangle E_b(T);$$

where the first term is the contribution from the step free energy E_s and the second is from the bulk free energy difference $\triangle E_b$.

Going to the continuum limit, $P_f(\ell, T)$ then becomes a probability density function. Since the quantities measured on the interface are averages over the fluctuation population, we will use a lower limit $\ell_{min} = 1$; this reflects the fact that the lattice cannot support a micro-facet of size smaller than unity. At bulk phase coexistence $\triangle E_b = 0$ and in the continuum limit, (126) is then

$$\int_1^\infty d\ell\ \Omega e^{-E(\ell)/T} = 1$$

$$\Longrightarrow \qquad \Omega = \tfrac{4E_s}{T} e^{4E_s/T}.$$

Now, several useful expectation values will be derived using $P_f(\ell, T)$. Note that we make repeated use of the integral identity

$$\int dx\ x^n\ e^{ax} = \frac{x^n e^{ax}}{a} - \frac{n}{a} \int\ dx\ x^{n-1}\ e^{ax}.$$

The mean micro-facet width:

$$\begin{aligned} \langle \ell \rangle &\equiv \int_1^\infty d\ell\ \ell\ P_f(\ell, T) \\ &= \Omega \int_1^\infty d\ell\ \ell\ e^{-4\ell E_s/T} \\ &= 1 + \frac{T}{4E_s} \end{aligned}$$

The mean micro-facet area:

$$\begin{aligned} \langle A \rangle &\equiv \int_1^\infty d\ell\ \ell^2\ P_f(\ell, T) \\ &= 1 + \frac{T}{2E_s} \left(1 + \frac{T}{4E_s}\right) \end{aligned}$$

The micro-facet area variance:

$$\begin{aligned}\sigma^2 &\equiv \int_1^\infty d\ell\,(\ell^4 - \langle A\rangle^2)\,P_f(\ell,T)\\ &= 6\left(\frac{T}{4E_s}\right)^2 + 16\left(\frac{T}{4E_s}\right)^3 + 20\left(\frac{T}{4E_s}\right)^4\end{aligned}$$

Finally, the fraction of the reference plane which is covered by micro-facets can be approximated using the following argument: It is assumed that the thermal energy density $\varepsilon(T) \sim T$ is distributed equally amongst all sizes of micro-facet; in other words,

$$\varepsilon(T) = \int d\ell\ \varsigma(\ell,T)\ P_f(\ell,T) \simeq T.$$

Thus, the energy density distribution function $\varsigma(\ell,T)$ is equal to T. This leads to a definition of the number density of micro-facets of size ℓ;

$$n(\ell) \simeq \frac{\varsigma(\ell,T)}{E_f(\ell)} = \frac{T}{4\ell E_s}.$$

The expectation of the *area* density of micro-facets is then

$$\begin{aligned}\langle \mathcal{A}_{tot}\rangle &= \langle n(\ell)A(\ell)\rangle\\ &= \int_1^\infty d\ell\ \frac{T}{4\ell E_s}\ell^2\ P_f(\ell,T)\\ &= \frac{T}{4E_s}\langle\ell\rangle = \frac{T}{4E_s}\left(1 + \frac{T}{4E_s}\right).\end{aligned}$$

Note that $\langle \mathcal{A}_{tot}\rangle$ is not directly applicable to the interface area; there is a prefactor $\mathcal{A}$ which depends on the details of the lattice, the model Hamiltonian and the geometry of the micro-facets. Thus, the expression for the fraction of the interface plane which is *not* covered by micro-facets is

$$\begin{aligned}\langle A_o\rangle &\equiv 1 - C_{onst}\mathcal{A}_{tot}\\ &= 1 - C_{onst}\left[\frac{T}{2E_s}\left(1 + \frac{T}{4E_s}\right)\right] \qquad (127)\end{aligned}$$

For this model, the prefactor has been measured to be $C_{onst} \sim 1/16$.

A.5 Growth and Evaporation Crystal Shapes

Some experimental measurements have been made of nucleation- and diffusion-limited growth (Gallet, Balibar and Rolley 1987) and evaporation on planar and droplet crystal interfaces (Dougherty and Gollub 1988; Heyraud and Métois 1980; Métois and Heyraud 1982; Heyraud and Métois 1987). Although not quantitatively comparable to the results presented here, the qualitative similarity between their photographic images and our surface representations is worth noting. Figure 68 shows a pair of images from a crystal evaporation experiment and the related simulation. The real crystal on the top is a gold (Au) droplet several μm in diameter from a study done by Heyraud and Métois (1980); note that the Au crystal is face-centered cubic (FCC) instead of simple cubic like our model and thus shows {111} facets as well as {100}. The simulation droplet on the bottom is from a $128 \times 128 \times 128$ system with both the solid and melt at the coexistence temperature $T_m = 0.4\ T_c$; the droplet is rapidly evaporating from its initial state as a perfect cube. Both systems are at a temperature below their respective equilibrium roughening temperatures. The Au crystal exhibits a series of concentric terraces which have been identified as diffusing step fronts. Although the resolution is somewhat low on the simulation model, the presence of similar steps around the main facets is detectable. A mechanism for *surface self-diffusion* has been proposed by Heyraud and Métois (1982).

Figure 69 shows a similar set of images from crystal growth studies. The physical crystals are again gold (Au) and lead (Pb) which is also FCC in structure; the Pb crystals are from another study by Heyraud and Métois (1987). The simulation image is from work which is not presented in this thesis. The main feature is the

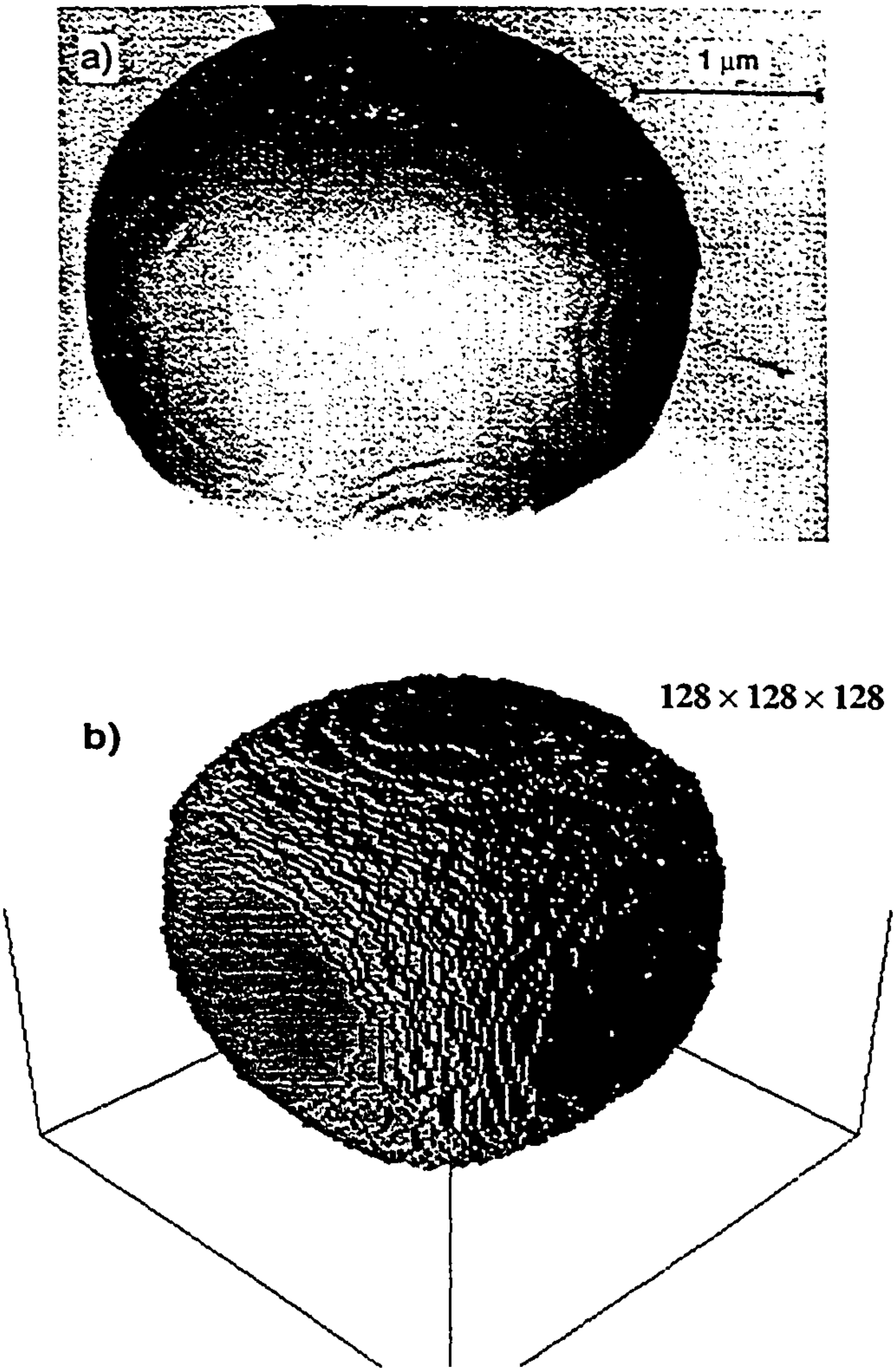

Figure 68: A pair of images comparing the appearance of evaporating crystals as observed in experiment (Heyraud and Métois 1980) and simulation (see Section 5.3). The physical crystal is gold (Au) on a graphite substrate; it has an FCC lattice structure and thus shows {100} and {111} facets. Note the similar concentric step patterns related to surface diffusion.

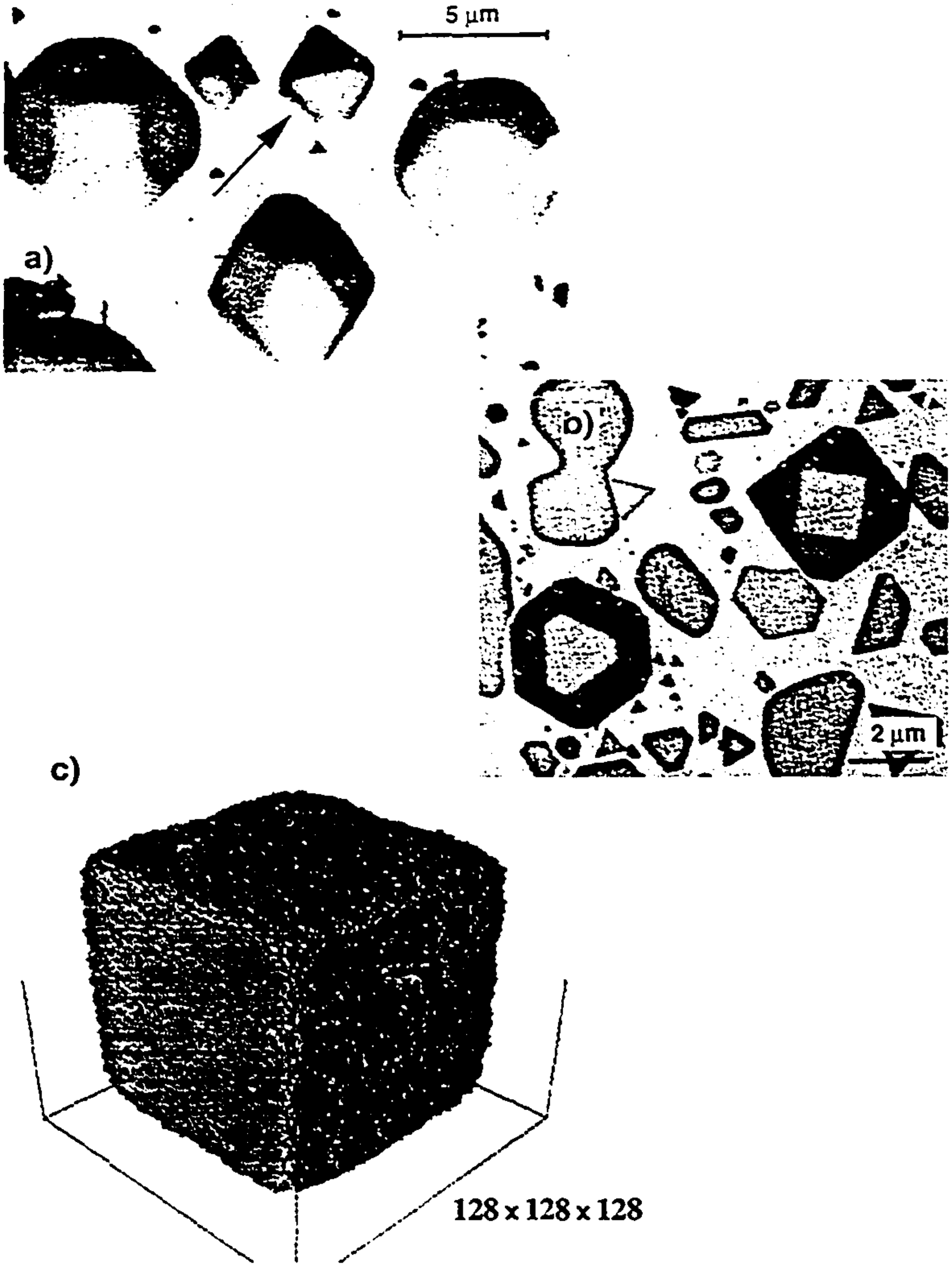

Figure 69: Three images comparing the appearance of growing crystals as observed in experiment (Heyraud and Métois 1980; Heyraud and Métois 1987) and simulation (not presented in this work). The physical crystals are a) gold (Au) and b) lead (Pb); they both have an FCC lattice structure and thus show {111} facets. Note the absence of curved and roughened regions.

absence of roughened regions between the facets. In the case of the Au crystals, several different stages of growth are observed. One crystal shape is presumed to be the state at late times (indicated by the arrow) where only the $\{111\}$ facets appear; similar to the case of the evaporating droplet described in Section 5.3, it is believed that the fastest growing regions (ie. the roughened interface) dominate the growth. The simulation image is the same system described above except that the coexistence temperature is $T_m = 0.5\ T_c$ (ie. the melt is undercooled).

A.6 Surface Area of Unstable Interfaces

The surface length (area) of unstable 1D (2D) interfaces is expected to increase like

$$s(t) \propto \begin{cases} t^2 & \textit{early } t \\ t & \textit{late } t \end{cases} \tag{128}$$

To demonstrate this, we make the following argument: We suppose an infinite 1D planar interface with a perturbation which has the form

$$h(x,t) = h_o + \sum_k a_k(t)(1 + \sin(kx)).$$

For simplicity, we shall isolate a single growth mode k' so that $a_k \equiv 0$ for $k \neq k'$. This form for the interface implies the case where there is no coarsening or side-branching of the needle crystals. The requirement that the tips move with constant velocity (typical of dendritic growth) sets the amplitude to $a_{k'} = C_{onst}t$. The total surface area (or, in 2D, the interface length) is described by

$$s(t) = \int_0^\lambda dx \sqrt{1 + \frac{dh}{dx}^2}$$

where the integral is over the wavelength of the sine wave $\lambda = 2\pi/kx$. This integral doesn't have a simple solution; instead we can look at it's early and late time behaviours. For small $a(t)$ (ie. early times), we approximate the square root with a Taylor expansion to first order;

$$\begin{aligned} s(t) &\simeq \int_0^{\lambda} dx \left(1 + \frac{1}{2}(a_k(t)k\cos(kx))^2\right) \\ \Longrightarrow &\propto t^2. \end{aligned}$$

For $a(t) \gg 1$ at late times, the 1 can be ignored and the square root approximated by

$$\begin{aligned} s(t) &\simeq \int_0^{\lambda} dx a_k(t)k\cos(kx) \\ \Longrightarrow &\propto t. \end{aligned}$$

This is consistent with the view that the needles are columns of constant cross-section (no coarsening) whose surface length increases solely along their sides. In 3D, the interface can be similarly defined as

$$h(x,y,t) = h_o(x,y) + \sum_{k_x,k_y} a_{k_x,k_y}(t)(1+\sin(k_x x))(1+\sin(k_y y))$$

and the total surface area becomes

$$S(t) = \int_0^{\lambda} dy \int_0^{\lambda} dx \sqrt{1 + \frac{\partial h}{\partial x}^2 + \frac{\partial h}{\partial y}^2}.$$

In applying the same limits of $a(t)$, we find the same time dependencies.

On a circular interface (ie. a disk in 2D), we can make a similar argument with regard to the total area of the droplet: Let's suppose a perfect disk of radius R_o. We can then perturb the interface

$$R(\theta) = R_o + \sum_m \rho_m(1+\cos m\theta)$$

where ρ is a function of t. Simplifying so that $\rho_m = 0$ except for one value of m, the area of the disk is

$$
\begin{aligned}
A(t) &\equiv \int_0^{2\pi} \int_0^{R(\theta)} r \, dr \, d\theta \\
&= \int_0^{2\pi} \frac{R(\theta)^2}{2} \, d\theta \\
&= \pi (R_o^2 + 2R_o\rho + \frac{3}{2}\rho^2).
\end{aligned}
$$

In the thermodynamic limit of $R_o \to \infty$, the disk interface becomes the planar interface. We can assume for large R_o that $\rho \propto t$ and thus to first order $A(t) \simeq t$ for small t. At late times, $A(t) \simeq t^2$.

References

Adler, J. 1987. *Phys. Rev. B*, **36**, 2473.

Balibar, S., Gallet, F., and Rolley, E. 1990. *J. Crys. Growth*, **99**, 46.

Becker, R. and Döring, W. 1935. *Ann. Phys.*, **24**, 719.

Ben Amar, M. and Pomeau, Y. 1988. *Euro. Lett.*, **6**, 609.

Ben-Jacob, E., Goldenfeld, N., Langer, J., and Schön, G. 1984. *Phys. Rev. A*, **29**, 330.

Binder, K. 1983. *J. Chem. Phys.*, **79**, 6387.

Binder, K. 1984a. *Phys. Rev. B*, **29**, 341.

Binder, k. 1984b. *Phys. Rev. A*, **29**, 341.

Browser, R., Kessler, D., Koplik, J., and Levine, H. 1984. *Phys. Rev. A*, **29**, 1335.

Bürkner, E. and Stauffer, D. 1983. *Z. Phys. B*, **53**, 241.

Burton, W., Ca76, N., and Frank, F. 1951. *Phil. Trans. Roy. Soc. London A*, **243**, 299.

Chou, H. and Cummins, H. 1988. *Phys. Rev. Lett.*, **61**, 73.

Chui, S. and Weeks, J. 1976. *Phys. Rev. B*, **14**, 4978.

Chui, S. and Weeks, J. 1978. *Phys. Rev. Lett.*, **40**, 733.

Creutz, M. 1984. *Phys. Rev. Lett.*, **50**, 1411.

Creutz, M. 1986. *Ann. Phys.*, **167**, 62.

de Gennes, P. 1971. In *Faraday Symposium #5 on Liquid Crystals*, page 16.

Dougherty, A. and Gollub, J. 1988. *Phys. Rev. A*, **38**, 3043.

Fisher, M. 1969. *J. Phys. Soc. Jap.*, **26**, 87.

Gallet, F., Balibar, S., and Rolley, E. 1987. *J. Physique Paris*, **48**, 369.

Glicksman, M. 1984. *Matls.Sci. and Eng.*, **65**, 5.

Glicksman, M., Shaefer, R., and Ayers, J. 1976. *Metall. Trans. A*, **7**, 1747.

Grant, M. 1988. *Phys. Rev. B*, **37**, 5705.

Grant, M., San Miguel, M., Viñals, J., and Gunton, J. 1985. *Phys. Rev. A*, **31**, 3027.

Grossman, B., Guo, H., and Grant, M. 1991. *Phys. Rev. A*, **43**, 1727.

Guo, H. and Jasnow, D. 1986. *Phys. Rev. A*, **34**, 5027.

Harris, R. 1985. *Phys Lett.*, **111A**, 299.

Harris, R. and Grant, M. 1988. *Phys. Rev. B*, **38**, 9323.

Harris, R. and Grant, M. 1990. *J.Phys. A*, **23**, L567.

Harris, R., Jörgenson, L., and Grant, M. 1992. *Phys. Rev. A*, **45**, 1024.

Heermann, D. 1984. *Phys. Rev. Lett.*, **52**, 1126.

Heyraud, J. and Métois, J. 1980. *J. Crys. Growth*, **50**, 571.

Heyraud, J. and Métois, J. 1987. *J. Crys. Growth*, **82**, 269.

Heyraud, J., Métois, J., and Bermond, J. 1989. *J. Crys. Growth*, **98**, 355.

Holzer, M. 1990a. *Phys. Rev. Lett.*, **64**, 653.

Holzer, M. 1990b. *Exact Equilibrium Crystal Shapes in Two Dimensions and Perturbation*

Expansions for the Facet Shape and Step Free Energy of a Three-Dimensional Equilibrium Crystal. PhD thesis, Simon Fraser University. see page 7 and 15 for comment on ECS as intensive state variable.

Holzer, M. and Wortis, M. 1989. *Phys. Rev. B*, **40**, 11044.

Horvay, G. and Cahn, J. 1961. *Acta Metall.*, **9**, 695.

Hwa, T., Kardar, M., and Paczuski, M. 1991. *Phys. Rev. Lett.*, **66**, 441.

Ivantsov, G. 1947. *Dokl. Akad. Nauk. SSSR*, **58**, 567.

Jackson, K. and Miller, C. 1977. *J. Crys. Growth*, **40**, 169.

Jayaprakash, C., Saam, W., and Teitel, S. 1983. *Phys. Rev. Lett.*, **50**, 2017.

Jörgenson, L., Harris, R., and Grant, M. 1989. *Phys. Rev. Lett.*, **63**, 1693.

Jörgenson, L., Harris, R., Grant, M., and Guo, H. 1993. In publication.

José, J., Kadanoff, L., Kirkpatrick, S., and D.R. Nelson, D. 1977. *Phys. Rev. B*, **16**, 1217.

Kardar, M., Parisi, G., and Zhang, Y. 1986. *Phys. Rev. Lett.*, **56**, 889.

Kessler, D., Koplik, J., and Levine, H. 1986. *Phys. Rev. A*, **33**, 3352.

Kessler, D., Koplik, J., and Levine, H. 1988. In *Advances in Physics*, volume 37, page 255.

Kim, J. and Kosterlitz, J. 1989. *Phys. Rev. Lett.*, **62**, 2289.

Kosterlitz, J. 1974. *J. Phys. C*, **7**, 1046.

Kosterlitz, J. and Thouless, D. 1973. *J. Phys. C*, **6**, 1181.

Landau, L. and Lifshitz, E. 1980. In *Statistical Physics*, volume 1, page 155. Pergamon, Oxford.

Langer, J. 1980. *Rev. Mod. Phys.*, **52**, 1.

Langer, J. 1987. In J. Souletie, J. V. and Stora, R., editors, *Lectures in the Theory of Pattern Formation, Chance and Matter*, Amsterdam. Les Houches Summer School Session 4b July 1986, North-Holland.

Langer, J. 1992. *Physics Today*, **45**(10), 24.

Langer, J. and Müller-Krumbhaar, H. 1978. *Acta Metall.*, **26**, 1681.

Langer, J., Sekerka, R., and Fujioka, T. 1978. *J. Crys. Growth*, **44**, 414.

Laxmanan, V. 1985. *Acta Metall.*, **33**, 1023.

Liu, F. and Goldenfeld, N. 1990. *Phys. Rev. A*, **42**, 895.

Maurer, J., Bouissou, P., and Perrin, B.and Tabeling, P. 1989. *Euro. Lett.*, **8**, 67.

Medina, E., Hwa, T., Kardar, M., and Zhang, Y. 1989. *Phys. Rev. A*, **39**, 3053.

Métois, J. and Heyraud, J. 1982. *J. Crys. Growth*, **57**, 487.

Métois, J. and Heyraud, J. 1987. *Surf. Sci.*, **180**, 647.

Metropolis, N., Rosenbluth, A., Rosenbluth, M., Teller, A., and Teller, E. 1953. *J. Chem. Phys.*, **21**, 1087.

Mon, K., Landau, D., and Stauffer, D. 1990. *Phys. Rev. B*, **42**, 545.

Mon, K., Wansleben, S., Landau, D., and Binder, K. 1988. *Phys. Rev. Lett.*, **60**, 708.

Mullins, W. and Sekerka, R. 1963. *J. Appl. Phys.*, **34**, 323.

Mullins, W. and Sekerka, R. 1964. *J. Appl. Phys.*, **35**, 444.

Murphy, L. and Rottman, C. 1990. *Phys. Rev. B*, **42**, 680.

Nelson, D. and Kosterlitz, J. 1977. *Phys. Rev .Lett.*, **39**, 1201.

Nicholas, J. 1965. *An Atlas of Models of Crystal Surfaces.* Gordon and Breach.

Nozières, P. 1989. *J. Physique Paris*, **50**, 2541.

Nozières, P. and Gallet, F. 1987. *J. Physique Paris*, **48**, 353.

Ohta, T. and Kawasaki, K. 1978. *Prog. Theor. Phys.*, **60**, 365.

Pavlovska, A. and Nenow, D. 1977. *J. Crys. Growth*, **39**, 340.

Pawley, G., Swendsen, R., Wallace, D., and Wilson, K. 1984. *Phys. Rev. B*, **29**, 4030.

Qian, X. and Cummins, H. 1990. *Phys. Rev. Lett.*, **64**, 3038.

Reichl, L. 1984. *A Modern Course in Statistical Physics.* University of Texas, Austin.

Rolley, E., Balibar, S., and Gallet, F. 1986. *Euro. Lett.*, **2**, 247.

Rolley, E., Balibar, S., Gallet, F., Graner, F., and Guthmann, C. 1983. *Phys. Rev. Lett*, **51**, 1366.

Rottman, C. and Wortis, M. 1981. *Phys. Rev. B*, **24**, 6274.

Rottman, C. and Wortis, M. 1984a. *Phys. Rev. B*, **29**, 328.

Rottman, C. and Wortis, M. 1984b. *Phys. Rep.*, **103**, 59.

Saito, Y., Goldbeck-Wood, G., and Müller-Krumbhaar, H. 1988. *Phys. Rev. A*, **38**, 2148.

Saito, Y. and Ueta, T. 1989. *Phys. Rev. A*, **40**, 3408.

Sekerka, R. 1967a. *J. Phys. Chem. Solids*, **28**, 983.

Sekerka, R. 1967b. Pergamon Press, Oxford.

Sekerka, R. 1971. In *Physical Chemistry in Metallurgy*, page 133. Proceedings of the Darken Conference, U.S. Steel Research Laboratories.

Shugard, W., Weeks, J., and Gilmer, G. 1978. *Phys. Rev. Lett.*, **41**, 1399.

Swendsen, R. 1978. *Phys. Rev. B*, **17**, 3710.

Touzani, M. and Wortis, M. 1987. *Phys. Rev. B*, **36**, 3598.

van Beijeren, H. 1975. *Commun. Math. Phys.*, **40**, 1.

van Beijeren, H. 1977. *Phys. Rev. Lett.*, **38**, 993.

van Beijeren, H. and Nolden, I. 1987. In Schommers, W. and von Blanckenhagen, P., editors, *Topics in Current Physics*, volume 43, page 259. Springer-Verlag, Berlin.

van Saarloos, W. and Gilmer, G. 1986. *Phys. Rev. B*, **33**, 4927.

Weeks, J. 1980. In Riste, T., editor, *Ordering in Strongly Fluctuating Condensed Matter Systems*. Plenum, New York.

Weeks, J. and Gilmer, G. 1979. In Prigogine, I. and Rice, S., editors, *Advances in Chemical Physics*, volume 40, page 157. Wiley, New York.

Wolf, P., Balibar, S., and Gallet, F. 1983. *Phys. Rev. Lett*, **51**, 1366.

Wolf, P., Gallet, F., Balibar, S., Rolley, E., and Nozières, P. 1985. *J. Physique Paris*, **46**, 1987.

Wulff, G. 1901. *Z. Krist. Mineral*, **34**, 449.

Yokoyama, E. and Kuroda, T. 1990. *Phys. Rev. A*, **41**, 2038.